2016

Hexagonal boron nitride nanosheets synthesis and applications

Feng Xiao
University of Wollongong

Institute for Superconducting and Electronic Materials

Hexagonal boron nitride nanosheets synthesis and applications

By Feng Xiao, B. Sc., M. Sc.

"This thesis is presented as part of the requirements for the award of the Degree of the Doctor of Philosophy at the University of Wollongong"

April 2016

Certification

I, Feng Xiao, declare that this thesis, submitted in fulfilment of the requirements for the award of Doctor of Philosophy, in the Institute for Superconducting and Electronic Materials, University of Wollongong, is wholly my own work unless otherwise referenced or acknowledged. This document has not been submitted for qualifications at any other academic institution.

Feng Xiao

April 2016

DEDICATION

To my parents, aunt and wife. You are always with me.

ACKNOWLEDGEMENTS

To my parents and my aunt, for your ongoing support, encouragement and concern whenever I need them. I could have never made it without you.

To my principal supervisor Dr. Zhenguo Huang, for his patience, encouragement, financial support, and understanding. To my co-supervisor Prof. Huijun Li for his support and encouragement.

To Dr. Sina Naficy, for his efforts in fabricating hydrogel and related tests, and other cooperative research work. To Dr. Christopher Richardson, for his assistance in CO_2 adsorption testing and suggestions for my paper. To Dr. Gilberto (STEM), Dr. Patricia Hayes (Raman and FTIR), Dr. Yi Du (AFM), Dr. Zhenxin Chen (TEM), and Dr. Germanas Peleckis (XRD), for their technical support. To Dr. Tania Silver, for polishing my papers and thesis.

To my friends Majharul Khan, Jian Hong, Weidong Chen, Prof. Baofeng Wang, Dr. Juner Chen, Ying Wang, Dr. Jiantie Xu, Dr. Qinjun Chen, Dr. Zhijia Zhang, Dr. Chengbo Zhu, Dr. Zengji Yue, Qing Meng, Weijie Li, Chao Han, Jun Wang, Lanlin Zhao, Zhixin Tai, Xinqi Chen, Prof. Jianmin Ma, Lili Liu, Chandrasekar Mayandi Subramaniyam, Mohammad Ihsan, Yunxiao Wang, Shaohua Zhang, and Jinyan Xiong, for their help and priceless friendship.

To the Chinese government for their financial support and for giving me this chance to study in Australia.

Finally, to my dear wife Jingwen Huang, for her love and constant support that helped me to achieve my PhD degree.

Abstract

h-BN nanosheet (denoted as *h*-BNNS) is a layer-structured material that has many outstanding properties, such as high thermal and mechanical performance, superb chemical and thermal stability, excellent lubricity, and strong insulating properties. These remarkable properties enable *h*-BNNS to be utilized in various applications, such as multi-function composites, military and electronic coatings, and biological materials. In this thesis, I have completed two projects on the synthesis of *h*-BNNS and its use in different applications.

In the first part of the work, upon flowing hot water steam over hexagonal boron nitride (*h*-BN) bulk powder, efficient exfoliation and hydroxylation of *h*-BN occur simultaneously. This method features high yield, high purity, low cost, and excellent scalability. For the first time, it has been confirmed that the hydroxyl groups are predominantly along the edges of the BN nanosheets via electron energy loss spectroscopy (EELS) mapping, in contrast to graphene oxide, where functionalization occurs both along the edges and on the basal planes. Although *h*-BN is known to be very inert and hard to functionalize, which severely limits its application, the hydroxyl (OH) groups can interact with various types of inorganic and organic matter via hydrogen bonding, and thus can help to explore the intrinsic properties of *h*-BNNS when dispersed in a foreign medium. The excellent dispersibility of OH-BNNS in water and alcohol enables a homogeneous distribution of the nanosheets in poly(*N*-isopropylacrylamide) (PNIPAM) hydrogel, which shows a 44% thermal enhancement compared with the pure hydrogel. Additionally, as one of the most commonly used temperature sensitive hydrogels, with applications ranging from drug delivery to various types of smart systems, PNIPAM hydrogel, upon mixing with OH-BNNS, shows dramatic improvement in two key aspects: dimensional change and dye desorption upon heating. *h*-

BNNS is nontoxic and chemically inert, and therefore, this finding could be highly valuable for bionic and soft robotic applications of PNIPAM hydrogel.

In the second part of the work, a bottom-up synthesis of *h*-BNNS with controllable thickness has been developed by using MgB_2 as a dynamic template, which naturally has layers of boron atoms sandwiched by magnesium atoms. This method enables the growth of predominantly bi-layered *h*-BNNS, which gives it an advantage over the commonly used exfoliation, which results in a wide distribution of layer numbers, and is being extended to the synthesis of other few-layered compounds based on existing layered atomic sheets in the starting materials. The layered structure of MgB_2 is also conducive to the controllable formation of micropores and mesopores, which are directly affected by the evaporation and decomposition of the Mg-based intermediates that are sandwiched by the *h*-BN sheets during the synthesis. For the first time, it has been experimentally demonstrated that boron rich *h*-BNNS can deliver great CO_2/N_2 adsorption selectivity, high CO_2 adsorption capacity, and a surprisingly large heat of adsorption for high CO_2 coverage. The strong interaction between CO_2 and *h*-BNNS is related to the boron active sites, which can be effectively controlled. This method offers a practical way to improve the CO_2 adsorption capacity of *h*-BNNS. These studies demonstrate the importance of developing novel methods for synthesis and functionalization, based on which the intrinsic properties of *h*-BNNS can be effectively explored.

TABLE OF CONTENTS

LIST OF PULICAITONS

1. **Feng Xiao**, Sina Naficy, Gilberto Casillas, Majharul H. Khan, Tomas Katkus, Lei Jiang, Huakun Liu, Huijun Li, and Zhenguo Huang. Edge-Hydroxylated Boron Nitride Nanosheets as an Effective Additive to Improve the Thermal Response of Hydrogels. ***Advanced Materials***, 2015, 27, 7247-7247.

2. **Feng Xiao**, Zhixin Chen, Gilberto Casillas, Christopher Richardson, Huijun Li and Zhenguo Huang. Controllable synthesis of few-layered and hierarchically porous boron nitride nanosheets. ***Chemical Communications***, 2016, DOI: 10.1039/c5cc09348a.

3. Majharul Haque Khan, Zhenguo Huang, **Feng Xiao**, Gilberto Casillas, Zhixin Chen, Paul J. Molino & Hua Kun Liu. Synthesis of Large and Few Atomic Layers of Hexagonal Boron Nitride on Melted Copper. ***Scientific Reports***, 2015, 5, 9547.

4. Ying Wang, Baofeng Wang, **Feng Xiao**, Zhenguo Huang, Yijing Wang , Christopher Richardson, Zhixin Chen, Lifang Jiao, Huatang Yuan. Facile synthesis of nanocage Co3O4 for advanced lithium-ion batteries. ***Journal of Power Sources***, 2015, 298, 203-208.

LIST OF FIGURES

LIST OF TABLES

Chapter 1 Introduction

Two-dimensional (2D) materials are crystalline materials with layer structures. Graphene was the first 2D material to be discovered, which happened in 2004. There are still 500 2D materials remaining to be found.[1] Graphene has many extraordinary properties, including excellent mechanical performance, remarkable thermal and electrical conductivity, and high thermal and chemical stability, which enable it to be widely applied in various fields, such as biological engineering, electronics, filtration, super lightweight/strong composite materials, photovoltaics and energy storage.[2] Recent research predicts that the graphene market will reach nearly $200 million by 2026.[3]

Inspired by graphene, one other 2D material, hexagonal boron nitride nanosheets (*h*-BNNS), has been widely explored. *h*-BNNS is in an unique position since it is an isoelectric analogue to graphene and shares similar structural features and many physical properties, except that it has a wide band gap. Moreover, *h*-BNNS has better thermal stability than graphene. Therefore, these unique advantageous properties promote its usage in various applications,[4-7] such as in the automotive industry, equipment and machinery, electronics, metallurgy, medicine, etc. It has been predicted that the worldwide market for *h*-BNNS is projected to reach 7.6 thousand tons by 2020, driven by expanding applications in sectors such as ceramics, industrial tools, refractory coatings, and electronic devices.[8] This massive demand has also benefited from the development of large-scale production routes and the emergence of new technologies.

In this thesis, two different facile routes are reported for the synthesis of edge-hydroxylated *h*-BN nanosheets (OH-BNNS) and porous *h*-BN nanosheets. These two types of *h*-BN enable them to be used as additives in composite fabrication and CO_2 adsorption, respectively.

OH-BNNS was obtained through the exfoliation and functionalization of bulk *h*-BN by water steam. The –OH groups are distributed along the edge of the OH-BNNS, which has been confirmed by electron energy loss spectroscopy (EELS) and Raman mapping. It has been found that the edge-functionalized OH-BNNS is especially beneficial for improving the thermal performance of hydrogel composite, due to the superb thermal properties of *h*-BNNS along the (002) orientation, where non-functional groups are on the surface of the OH-BNNS. The thermal conductivity of the OH-BNNS/ poly(*N*-isopropylacrylamide) (PNIPAM) hydrogel has been improved by almost 44% compared to the neat PNIPAM hydrogel. It was also observed that OH-BNNS/PNIPAM hydrogel shows faster dimensional change and dye release. In addition, *h*-BN is non-toxic. Consequently, the OH-BNNS/PNIPAM hydrogel composite is highly promising for application in drug delivery in the future.

Hierarchical porous *h*-BNNS has been synthesized by using MgB_2 as a dynamic template, NH_4Cl as an etchant, and NH_3 as a nitrogen source. The resultant *h*-BNNS, synthesized at lower temperature, is highly porous, with majority of nanosheets being bilayer thick. The porous structure is ascribed to gas release during the reaction; the massive bilayers are associated with the magnesium-based by-product that exists as a separate layer, protecting the *h*-BNNS from coalescence. Additionally, *h*-BNNS is chemically and thermally stable. The featured *h*-BNNS is thus promising for CO_2 adsorption in various harsh environments.

According to the analysis, the resultant *h*-BNNS has a significantly improved surface area compared to that of the bulk *h*-BN and exhibits a high adsorption of CO_2.

This thesis starts with a comprehensive literature review (Chapter 2), followed by an introduction to the experiments (Chapter 3), then a description of the two projects (Chapters 4-5). It finishes with the conclusions and outlook (Chapter 6).

References

[1] The super materials that could trump graphene. Nature. 2015. 522, 274-276.

[2] Graphene Uses & Applications. Graphenea.

[3] “Graphene-Info Market Report". Graphene-info. 2015.

[4] Pakdel, A., C. Zhi, Y. Bando, and D. Golberg, Low-dimensional boron nitride nanomaterials. Materials Today, 2012. 15, 256-265.

[5] Lin, Y. and J.W. Connell, Advances in 2D boron nitride nanostructures: nanosheets, nanoribbons, nanomeshes, and hybrids with graphene. Nanoscale, 2012. 4, 6908-6939.

[6] Pakdel, A., Y. Bando, and D. Golberg, Nano boron nitride flatland. Chemical Society Reviews, 2014. 43, 934-959.

[7] Xiang-Fen Jiang, Q.W., Xue-Bin Wang, Xia Li, Jun Zhang, Dmitri Golberg, Yoshio Bando, Recent Progress on Fabrications and Applications of Boron Nitride Nanomaterials: A Review. J. Mater. Sci. Technol., 2015, 31, 589-598.

[8] Raw & Manufactured Materials. Ceramic industry. 2015.

Chapter 2 Literature review

2.1 Brief of *h*-BN

BN exists in various allotropes. The most common and stable polymorph is *h*-BN, analogous to graphite featuring a lamellar structure and inherently slippery and soft property, and is therefore widely used as a lubricant and filler to cosmetic products. The sp^2-bonded layered configuration can be found in rhombohedral boron nitride (*r*-BN), which is in ABC stacking rather than in AB stacking in *h*-BN. Similar to the graphite and diamond, consisting of sp^2 conjugated carbon layers and a sp^3 conjugated carbon atom lattice, respectively, *h*-BN and cubic BN (*c*-BN) are corresponding isoelectric BN allotropes.

BN does not exist in nature and is thereby a synthetic compound from elemental B, boric acid (H_3BO_3) or boron oxide (B_2O_3) reacting with various nitrogen sources, such as N_2 gas, ammonia gas (NH_3), urea ($CO(NH_2)_2$) and melamine ($C_3H_6N_6$) at high temperatures over 1200 °C. BN was firstly synthesized from the reaction between molten H_3BO_3 and potassium cyanide (KCN) under atmospheric pressure by Balmain in 1842,[1, 2] However, it took over 100 years to enable BN powders and hot-pressed shapes to be stabilized. Subsequently, with a great effort on modern processing technology, BN has become a practical material with various forms applied in a wide range of fields.

Inspired by identification of carbon nanotubes (CNTs) in 1991,[3] pure BN nanotubes (BNNTs) were successfully synthesized in 1995.[4] Other 1D BN nanomaterials such as nanowires, nanorods and nanofibers were subsequently reported 10 years later.[5-7] Following the discovery of the C_{60} soccer ball,[8] in addition, 0D octahedral BN fullerene

were synthesized by Stephan and Golberg respectively in 1998, which were cage-like and rectangle-like rather than the quasispherical carbon fullerene morphology.[9, 10] In 2004, a discovery of graphene's amazing physical properties aroused the researchers' curiosity on 2D materials.[11] One of the most widely studied 2D counterparts is *h*-BN nanosheets (BNNSs), the synthesis of which was initially reported just a few months later. Afterwards, Novoselov extended the mechanical cleavage approach employed on graphene and obtained free-standing 2D *h*-BN flakes by peeling the BN crystals.[12]. Although BNNS has been considered as an insulator, BN nanoribbons (BNNRs), which are the BNNSs with varied length but small widths, were initially prepared in hollow morphology [13] and were proposed to be half metal in zigzag BNNRs (ZBNNRs) when the B edge of ZBNNS is passivated.[14] Models of 0D, 1D and 2D BN nanostructures are shown below in Figure 2.1.

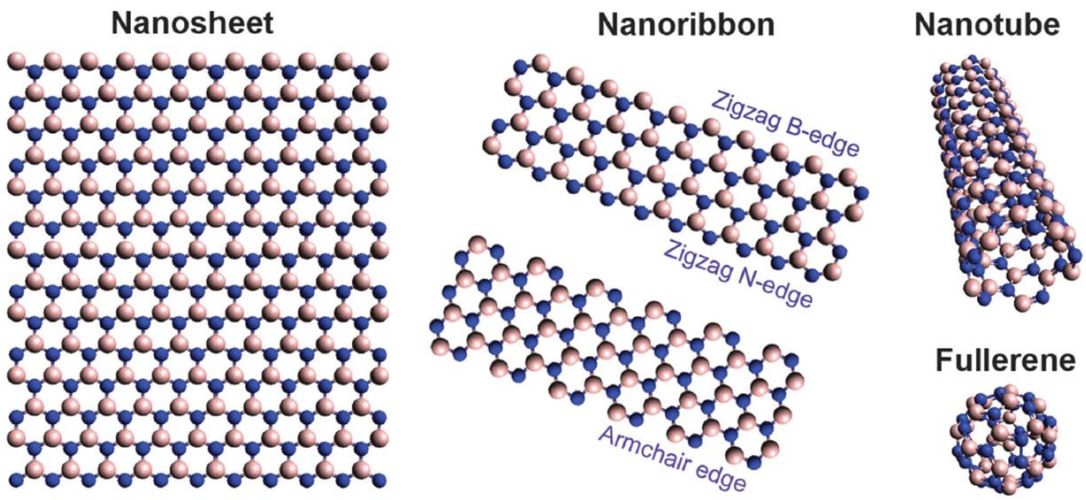

Figure 2.1. Models of 2D, 1D and 0D BN nanostructures.[15]

2.2 Structure

Analogous to graphite, *h*-BN has a honeycomb structure but with alternating B and N atoms linked by sp^2 hybridized orbits. The interlayers of *h*-BN are held by van der Waals forces. The B-N bonds with ionic features are 0.144 nm (0.142 nm in Graphene) in length and the distance between the centres of neighbouring hexagonal rings is 0.25 nm (0.246 nm in

graphene). To satisfy the electrostatic or polar-polar interactions (referred to as “lip-lip” interactions in individual BNNS layers), BN shows AA’ stacking, in which the adjacent hexagon rings are superposed with B and N atoms alternatively located along the c axis, whereas graphite shows AB stacking, in which each layer is shifted by half a hexagon with C atoms always sitting in the centre of the hexagons. This AA’ structure of *h*-BN contributes to a stronger interlayer interaction than in graphene, resulting in poorer exfoliation or functionalization when compared to graphene. Although the AA’ stacking is intrinsic to the bulk *h*-BN, the top and bottom layer of the layered structure may also slide forming AB stacking structure.[16-19] According to the van der Waals corrected density functional theory (DFT) computations, a nearly free-sliding pathway from AA’ stacking to AB stacking has been identified but a band gap modulation of ~0.6 eV is predicted to occur.[18]

B-N bond is more energetically favourable than B-B or N-N bonds based on the *ab initio* molecular dynamics calculations. The computed energy cost of the anti-site defect, where two adjacent B and N atoms are replaced by two B-B bonds and N-N bonds, increases from 5.5 eV to 7.1 eV after atomic relaxation.[20] Compared to graphitic C-C bonds, B-N bonds show a combined interaction both ionic and covalent bonding associated with the disparity in electronegativity between B and N atoms.[21] This can also result in “lip-lip” interactions among layers, which facilitates stabilizing the growth of open-ended BNNTs through the forming of bridges between consecutive shells to evolve into a metastable energy minimum, similar to the growth of carbon nanotubes (CNTs). [20, 22, 23]

There are many methods to identify the layer number of a BNNS, in which transmission electron microscopy (TEM) is the most straightforward technique. Since those nanosheets are

extremely thin and tend to be crumpled on the sheets plane or folded on the edges, the layer number thus can be directly observed at the crumpled and folded areas under the high resolution TEM (HR-TEM) imaging. Figure 2.2a shows a thin BNNS prepared by chemical exfoliation. Obviously, there are many curled sheets, which are associated with the thin BNNS. Figure 2.2b shows BNNSs at high magnification, where it is easy to determine the layer number of BNNSs (bilayered and four-layered BNNSs, respectively). The thickness of the *h*-BNNS can be calculated based on the *d*-spacing of BNNS (0.33 nm for the *h*-BN). However, *d*-spacing can be altered depending on its crystalline extent and functional groups grafted. [24-29] Alternatively, atomic force microscope (AFM) is a straight way to determine the thickness of BNNS. It is more suitable for measuring those samples with a relatively thicker thickness (>20 layers) than TEM, under which it's difficult to count the layer number. Non-contact mode is always employed where the cantilever is oscillating at or just above its natural resonance frequency over the sample surface with the amplitude of oscillation about a few picometers up to a few nanometers. The measured height of monolayer is prone to be higher than in theory on account of the trapped solvent deriving from the transferring or dispersing process which is inevitable so far.[28-35] Other impurities and functional groups on *h*-BNNS surfaces are possible to further increase the height value. Therefore, AFM is a complementary approach for the thickness measurement. Optical microscope has also been used in determining the layer number of BNNS, intrigued by the utilization in large-area thin graphene.[36] Even with the interference enhancement from the coated silicon film, BNNS exhibits very low optical contrast since the absorbing wavelength is beyond visible region (band gap larger than 5 eV). In spite of this, BNNS was optically identified on a silicon wafer coated ~ 90 nm silica layer and its optical contrast was improved from less than 1.5%, which is indiscernible, to 2.5% (~3% with a green filter), which is comparable to that for graphene on transparent substrate in light-transmission mode (Figure 2.2d).[37] This method is

however very sensitive to any contaminant or a thin layer of water, which can notably interfere the optical contrast due to the weak contrast. The layer number of graphene can be determined by the G band Raman peak (~2650 cm^{-1}).[38] Similarly, Raman spectroscopy has been employed for the determination of the layer number of BNNS as well. It's been suggested that the E_{2g} band (around 1366 cm^{-1} for the bulk *h*-BN) would shift along with the reduced thickness. It's reasoned that the elongation of B-N bond in bulk *h*-BN associated with the interlayer interaction results in a softening of the phonon while in the case of the few-layered BNNS, the weaker interlayer interactions contribute to a shortening of the B-N bond. [37, 39] Specifically, E_{2g} band is usually blue shifted in monolayers and red shifted in few-layers relative to its position in bulk *h*-BN (Figure 2.2e). With respect to the full width of half maximum (FWHM), a substantial decrease would occur for few-layered BNNS ascribed to the decrease in the superposition of multiple E_{2g} peaks in these more homogenously distributed BNNS with smaller sheet size and thinner sheet thickness.

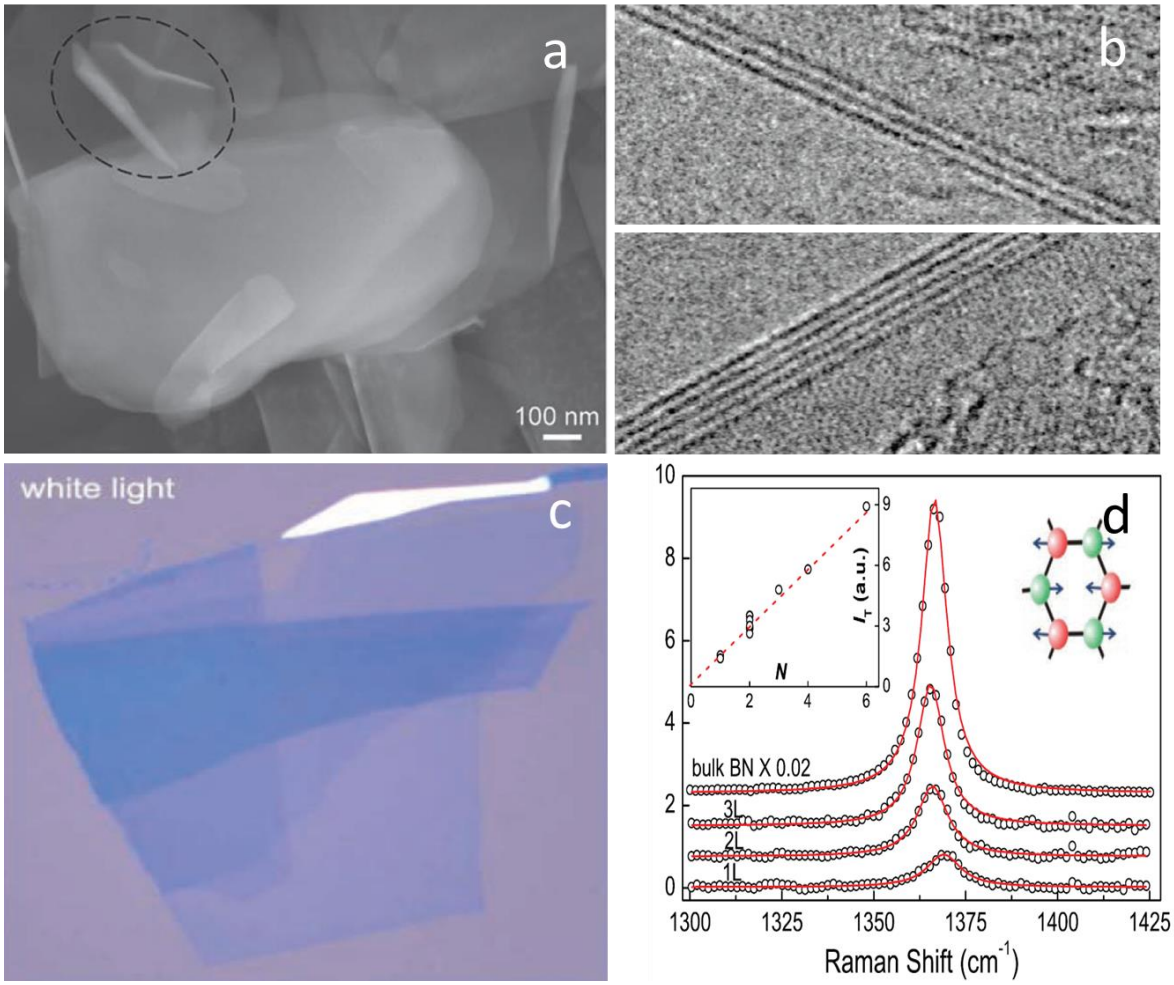

Figure 2.2. (a) a low-magnification TEM image of a chemically synthesized *h*-BNNS with crumpled and folded features.[28] (b) a high-magnification TEM image of few-layered *h*-BNNS showing lattice fringes.[29] (c) an optical image of a mechanically exfoliated BNNS on a 90 nm SiO_2/Si wafer under white light.[37] (d) Raman spectra of monolayer, bilayer, trilayer and bulk *h*-BN (inset left showing the changes in integrated intensity of I_T dependent on the number of layers N and inset right illustrating the phonon mode responsible for the Raman peak).[37]

Layered materials have interesting applications due to their highly anisotropic properties.[32] The increasing focus has been witnessed since the mechanically exfoliated and chemically synthesized single- and few-layered graphene was found,[11, 41] which exhibits a wide

variety of unusual physical properties.[42-45] *h*-BNNS is an insulator with a graphite-like structure and therefore is called "white graphene". In spite of the great similarity in structure between *h*-BNNS and graphene, their electronic properties are disparate; as *h*-BN is an insulator with a wide band gap of approximately 5.9eV, while graphite is a semimetal.[46] *h*-BN films have a variety of attractive properties, such as excellent mechanical strength, a large thermal conductivity, high hardness, high-effective corrosion resistance and distinguished chemical stability at high temperature to 1000 ℃ in air, much higher than that of graphene with the corresponding temperature only 400 ℃, leading to numbers of promising applications.[46-50]

2.3 Defects

BN is one of the most attractive materials technologically. Theoretically, BN with perfect atomic lattice exhibits remarkable mechanical and thermal properties. In reality, the imperfection of the materials production processes results in inevitable structural defects. Such lattice defects have a dramatic influence on the performance of BN-based composites.

Stone-Wales (SW) defect is considered as a point defect, which alters the connectivity of two π-bonded C atoms and contributes to their rotation by 90° based on the midpoint of their bond (Figure 2.3).[51] The reaction finally leads to two separate rings that have vertices bonded to each other rather than two rings sharing an edge. This structural imperfection is common in sp^2 bonded carbon allotropes, such as graphene where hexagonal rings are converted into pentagons and heptagons when the C-C bonds rotate by 90°. The formation of the SW defects retains the same number of atoms as original graphene without dangling bonds generated. Its high formation barrier (10 eV) results in the negligible equilibrium

concentration at experimental temperatures below 1000 °C, but the defect can be generated under non-equilibrium conditions (e.g., under irradiation or quenching) associated with the reverse transformation barrier (5 eV).[52] Similarly, SW exists in BN nanomaterials. First-principles computations on zigzag and armchair BN nanoribbons (zBNNR and aBNNR) suggests that the formation of SW defects are mainly influenced by their geometric structure in BNNR and SW defects dramatically decrease the band gaps regardless of BNNR orientations. Since there are two kinds of B-N bonds in zBNNR and aBNNR, which are parallel and perpendicular to the axis, two types of SW defects are possible in zBNNR and aBNNR (denoted as SW-1 and SW-2). The new B-B and N-N bands are shorter for SW-1 in zBNNR but longer for SW-1 in aBNNR compared to that for SW-2 in both of cases.

Consequently, it leads to the structural deformation where the B and N atoms are slightly outward from the plane. This structural deformation is reflected by the pyramidalization angle ($\Theta_p = \theta_{\sigma\pi} - 90°$) which is adopted to determine the extent of sp^3 hybridization of an atom ($\theta_{\sigma\pi}$ is the angle formed by σ and π bonds). It's been computed that the formation energies of SW defects rise with increasing widths of BNNRs. Moreover, the formation of the SW defects drastically decreases the energy bandgap of defective BNNRs, albeit they still maintain large-band-gap semiconductor behaviour. Additionally, the SW defects sites are more reactive than sites in the centre of defect-free BNNR. In particular, the newly created B-B and N-N bonds become the most reactive in SW defects ascribed to their energetically unfavourable feature.[53]

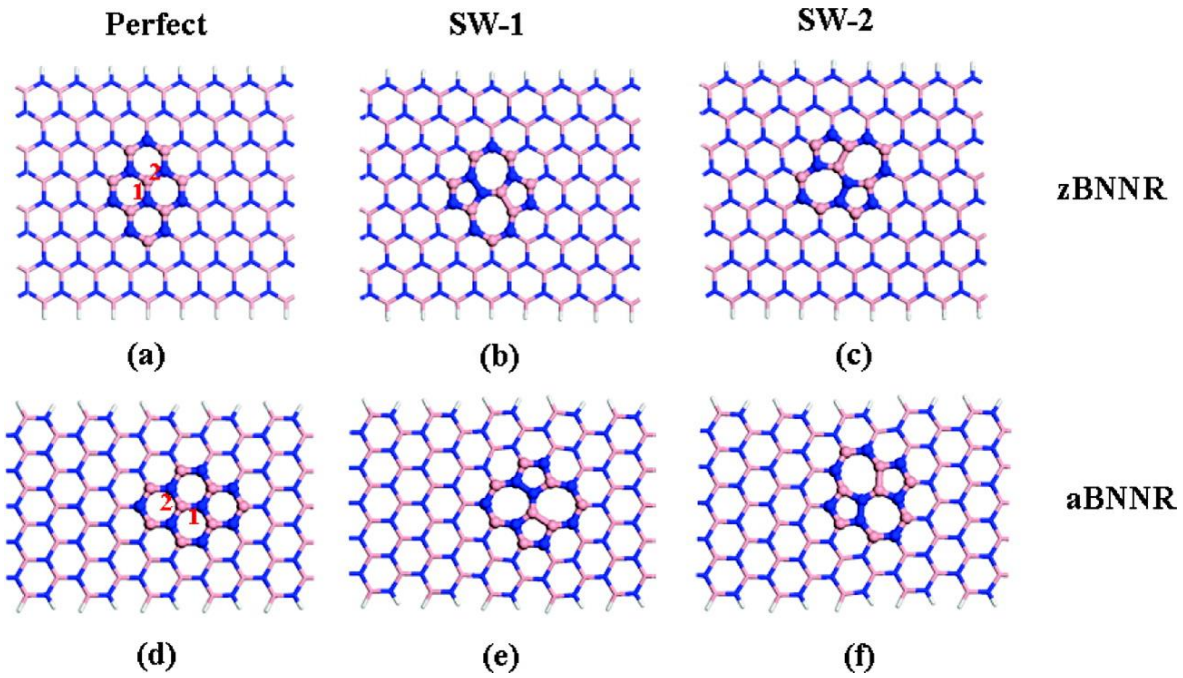

Figure 2.3. Two types of the B-N bonds in zBNNR and aBNNR, and their SW-1 and SW-2 defects respectively.[53]

The size of the grains and the atomic structure of their grain boundaries (GBs) tend to drastically influence the properties of polycrystalline materials. These impacts are especially prominent in two-dimensional materials, where even a line defect can divide and disrupt a crystal. Compared to the homoelemental graphene, heteroelemental *h*-BN exhibits more complexity. In graphene, elastic strain primarily determines the energy of dislocation, therefore the core of dislocations is constituted of pentagon-heptagon pairs (5/7s) on account of the lower strain energy than other polygon pairs, such as square-octagon pairs (4/8s) (Figure 2.4). In the contrast, the energy of dislocation in BN is comprised of both topological strain and possible homoelemental bonding, which is weaker than heteroelemental bonding in a perfect lattice. The first-principles calculation suggested that 5/7s necessitate lower strain energy, but they unavoidably introduce homoelemental bonding (B-B or N-N). Nevertheless, 4/8s are free of the homoelemental bonding while it's subjected to the higher strain energy. Interestingly, based on the structures of dislocations, it's been found that grain boundaries

can accommodate either polar (B-rich or N-rich), composed by 5/7s, or unipolar, constituted of 4/8s on varied tilt angle of grains. The polar grain boundaries tend to carry net charges brought by extra atoms, positive at B-rich and negative at N-rich ones, resulting in a change in band gap by as much as 38% while grain boundaries in graphene are prone to restraining the electronic transport.[54] Experimentally, both 5/7 defect and 4/8 were observed under high resolution TEM (HRTEM) with a ~22° angle deviation of their grain boundaries.[55] Recent theoretical calculations have predicted that introduction of curvature in the sheet favours the defects formation attributed to the decrease in formation energy.[54] This has been seen in Figure 2.5 that the warped structure is dynamic and eventually flattens, converting into in-plane strain in the unit cells to lower the energy. Within a period of 16 s under e-beam irradiation at 80 kV, the boundary relaxed from the highly strained wrinkle to the planar structure. However, the grain boundaries itself are robust, though with vacancies, defects and wrinkles with high local strain exist along them. [55]

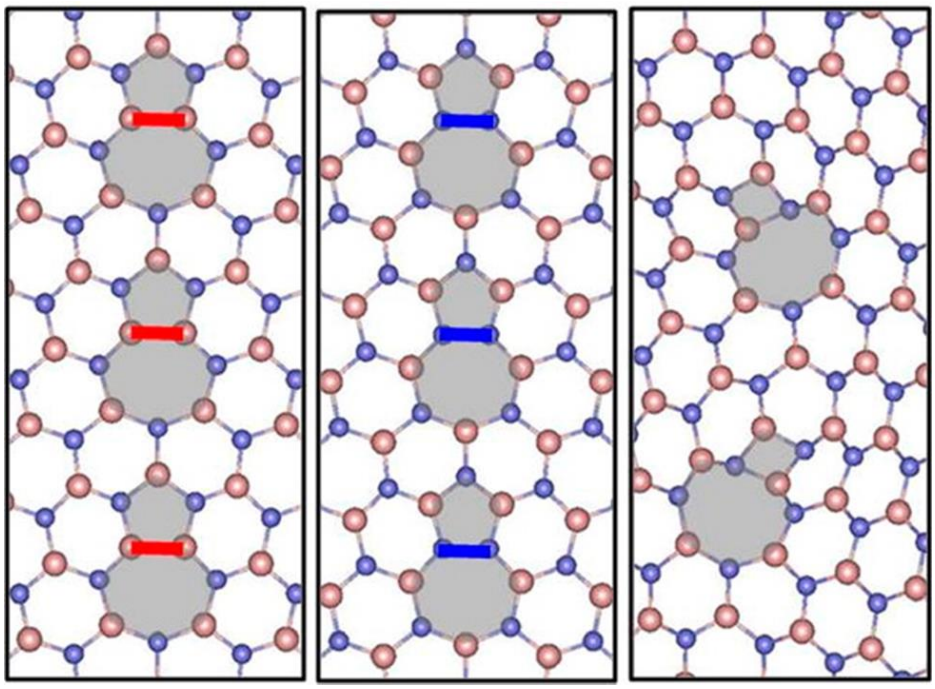

Figure 2.4. Grain boundaries (a) polar, constituted of 5/7s (N-rich); (b) polar, constituted of 5/7s (B-rich); (c) nonpolar, constituted of 4/8s.[54]

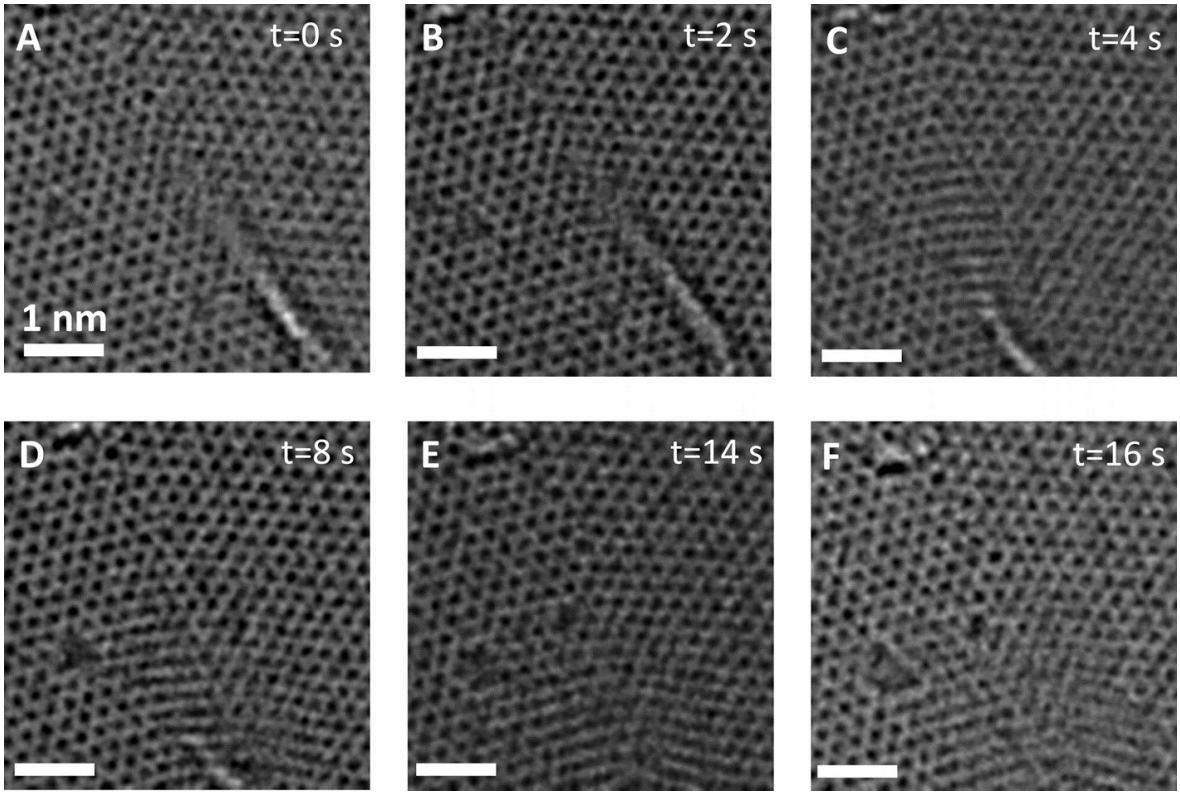

Figure 2.5. HRTEM time series images of a grain boundary in a *h*-BN film. (A) Out-of-plane strain and warping are visible in the lower right corner. (B) After 2 s the wrinkle remains but the local structure of the 5/7s has changed. (C) After 4 s the wrinkle has changed curvature. (D) After 8 s wrinkle is almost flattened. (E) After 14 s a strained nanograin formed. (F) The dynamic transition is in equilibrium.[55]

Lattice defects has also been identified by directly imaging and even distinguishing individual boron and nitrogen atoms under HRTEM and many triangle-shaped vacancies with discrete sizes have been observed ascribed to the knockon effect of the incident electron beam (Figure 2.6).[56] Note that all the triangles are in the same orientation, which indicate that monovacancy of boron (V_B) and monovacancy of nitrogen (V_N) will not coexist as two types of vacancies exhibit opposite orientations. Theoretically, boron has a lower knockon energy (about 74 kV) than that of nitrogen (about 84 kV),[57] therefore, it's prone to forming

boron vacancies rather than forming nitrogen vacancies under high energy charged electrons. Consequently, V_N are not observed under HRTEM, but instead V_B, V_{3B+N} and V_{6B+3N}, etc. are found.[58] However, one group found that only one element forms a monovacnacy under 120 kV, which is voltage of atoms to be knocked out. Therefore, there might be other mechanism except the pure knockon damage, such as an immediate replacement of the ejected atom by mobile atoms nearby.[59] Additionally, the layer distance with a missing boron atom is found to be substantially enlarged, indicating that dangling bonds for each N atom might be repulsive to each other. Such a relaxation also results in restraining to form a pentagon and stabilization of the V_B. It's emphasized that no stable divacancy (V_{BN}) has been observed in order to compensate the charge because V_{BN} would immediately transform to the V_{3B+N} due to the further removal of doubly coordinated boron atoms.[56]

Although defects tend to degrade the intrinsic thermal and mechanical properties, deviation from the perfection can be useful in some applications. The band gap can be altered with the defects.[60] It's been calculated that B antisites (N site occupied by B instead) have strong adsorption of CO_2 gas.[61] Different functional groups have been grafted on BNNS, which can offer a better dispersibility and even give rise to magnetic property.[35, 62]

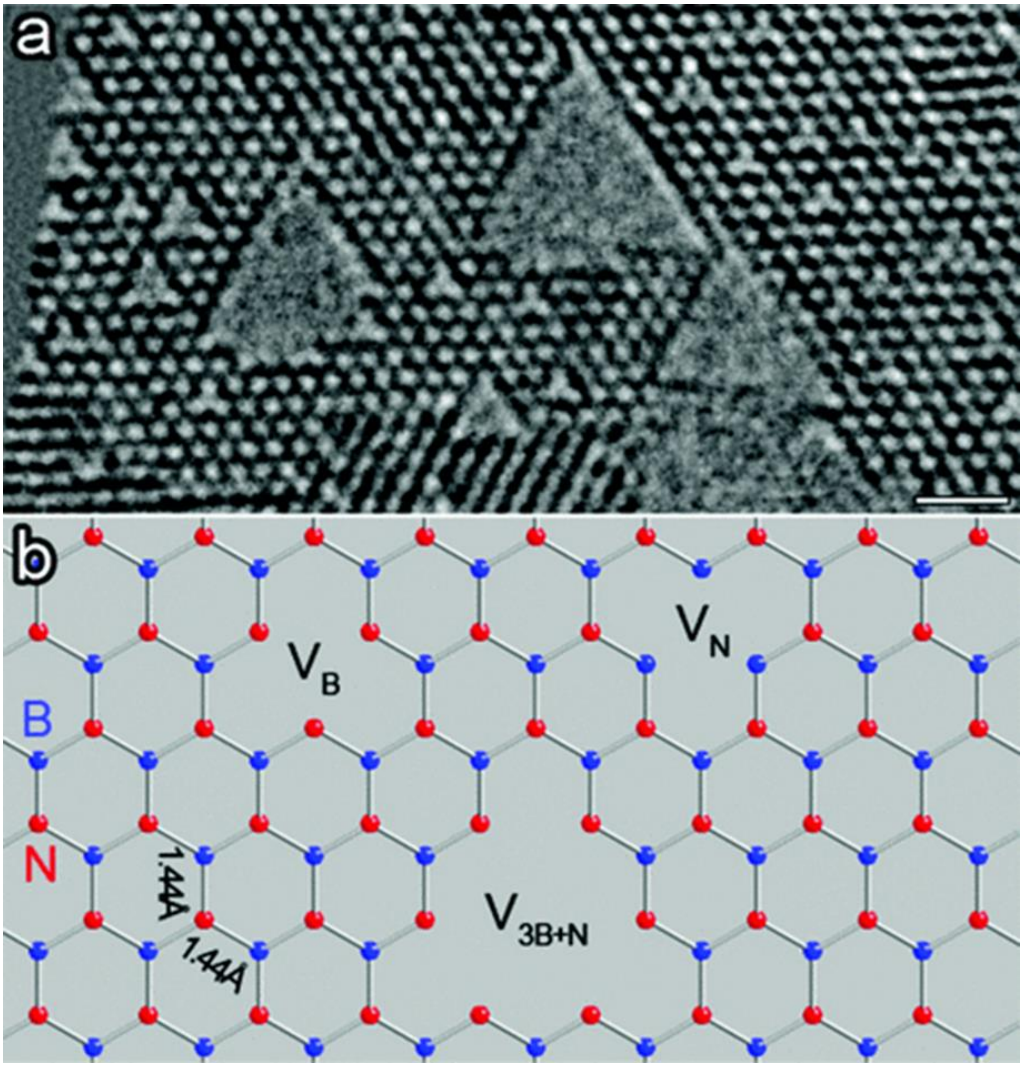

Figure 2.6. Point defects in *h*-BN monolayer. (a) A typical HRTEM image showing the lattice defects in *h*-BN with same orientation but various sizes. (b) Models for atomic defects in *h*-BN. V_B and V_N stand for boron and nitrogen monovacancy respectively.[56]

2.4 Preparation of *h*-BNNS

A great effort has been devoted to preparing the BNNS and those methods show respective advantages in relation to different applications.

2.4.1 Mechanical exfoliation

2.4.1.1 Scotch tape cleavage

Mechanical exfoliation has been considered as the best and most simple way to prepare high-quality 2D materials.[11, 12] Novoselov et al, who tried to obtain single sheets of other layered materials like $NbSe_2$ and MoS_2, $Bi_2Sr_2CaCuO_x$ by micromechanical cleavage, commented on the possibility of obtaining similar results on layered boron nitride sheets.[12] Pacile et al isolated BN nanosheets (BNNS) using adhesive tape to peel off BN layers from powdered *h*-BN and press onto a targeted substrate. Through repeating the peeling-pressing process, BNNS would be exfoliated down to a monolayer level. Although large-scaled *h*-BN sheets with an average crystal size of about 10 μm had been obtained, those sheets were uneven with the thinnest region of about 3.5 nm but the thickest region of roughly 80 nm (Figure 2.7).[63] Few-layered BNNS prepared this way has shown interesting properties.[37, 56, 58, 59, 64-67] However, this method is less effective and the lateral size of BNNS is limited by the lateral size of commercial *h*-BN powder.

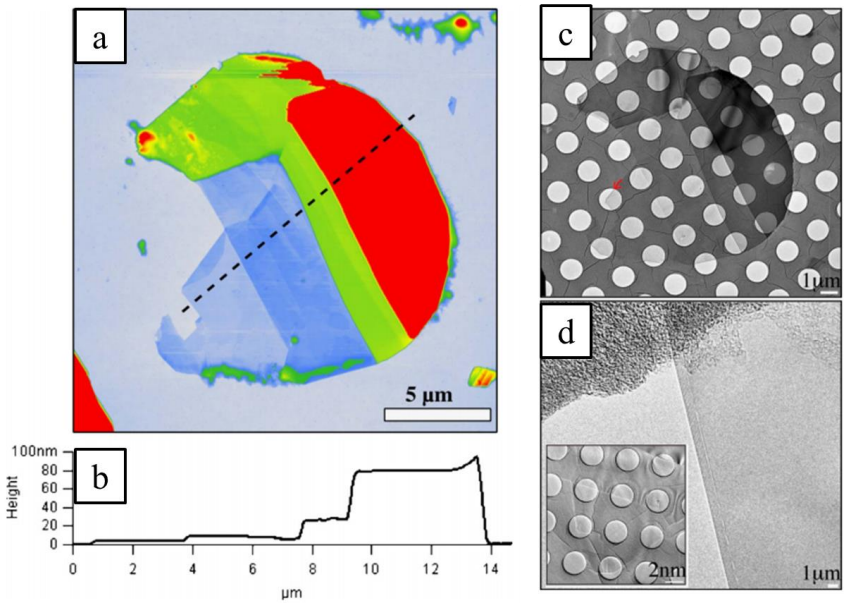

Figure 2.7. a) AFM topography image of exfoliated BNNS under tapping mode. b) The dashed line indicates the position of the line profile. The thinnest area is 3.5 nm. c) TEM

image of exfoliated *h*-BNNS in low magnification. (d) Zoom-in image highlighted by the red arrow in c.[63]

2.4.1.2 Ball milling

Scotch tape method is perhaps the least productive and can only satisfy the requirement in laboratories. In order to increase scalability, other methods used similar shear forces have been employed.[68-70] Ball-milling approach is one of the most common mechanical cleavage. A considerable size refinement was achieved at the initial hours (t<3 h) of milling with the lateral size of particles decrease from 394-607 nm to 90-214.[71, 72] Additionally, the high-energy ball milling may lead to the chemical activation of *h*-BN which is intrinsically chemical inert. The amorphous part of activated BN can be easily hydroxylated even at room temperature.[73, 74]

A low-energy ball milling with gentle shear forces introduced by rolling actions of the planetary mill was also applied for the mechanical cleavage of *h*-BN. The milling energy is controllable by adjusting ball sizes and rotating speed. During the milling process, *h*-BN powder was under the protection from the benzyl benzoate which could diminish the ball impacts and milling contamination associated with its high viscosity. Furthermore, compared to other solvent, *i.e.* water, ethanol and acetone, benzyl benzoate has a similar surface energy to *h*-BN, which largely prevents the newly isolated BNNS from agglomerating and facilitates dispersion. A 67% production yield of few-layered BNNS was achieved and the in-plane structure of the BNNS still remained.[68] A scalable ball milling has been proposed by mixing *h*-BN powder with sodium hydroxide in aqueous solution via a synergetic effect of chemical peeling and mechanical shear forces (Figure 2.8). With the assistant of aqueous

NaOH solution, which is capable of reducing the shear forces and cutting the *h*-BN sheets attributed to the reaction between *h*-BN and the hydroxyl ions, leading to minor damage to the in-plane structure of the hydroxyl-functionalized BN nanaplatelets (OH-BNNPs). Moreover, the concentrated NaOH solution enables a mild cutting reaction than molten hydroxide, resulting in relative large flakes with an average size of 1.5 μm. The resultant OH-BNNPs products are able to be redispersed in various solvents and form stable dispersions.[75]

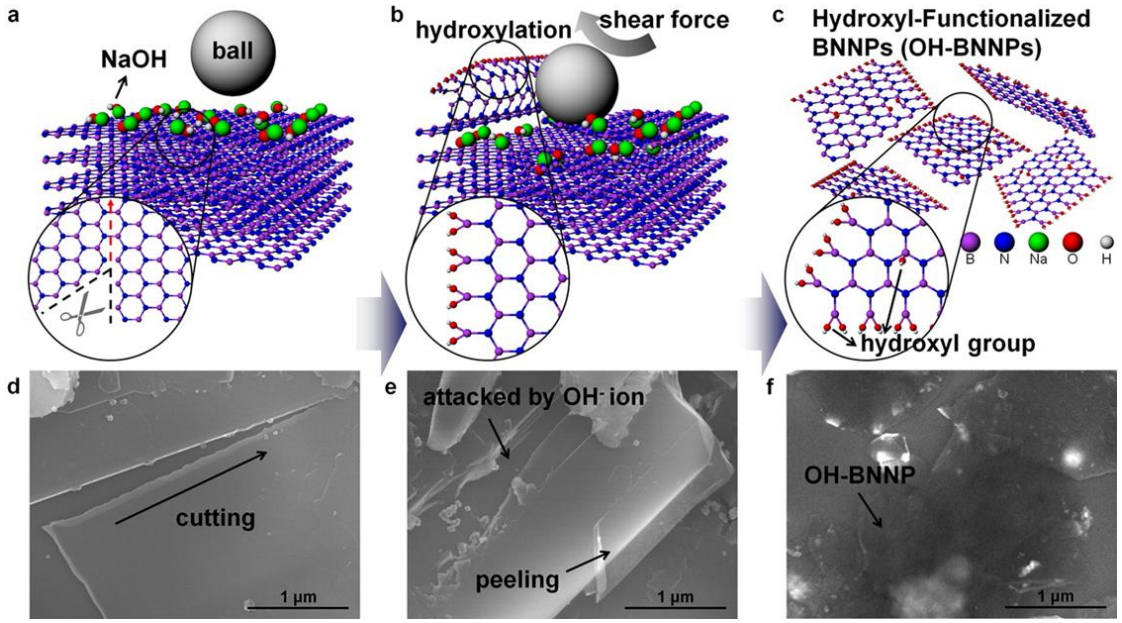

Figure 2.8. Schematic illustration and corresponding SEM images of *h*-BN. (a,d) Cutting of large *h*-BN sheets via the reaction between *h*-BN and the hydroxyl ions. (b,e) Thin curled sheets peeled off from the surface of an *h*-BN particle by the shear forces. (c,f) Exfoliated OH-BNNPs.[75]

2.4.1.3 Fluid shearing

Vortex fluid exfoliation is a novel and effective way to prepare the BNNS. *h*-BN powder was dispersed in NMP, which serves as a stabilising surfactant to enhance the dispersion and to

avoid agglomerating. The exfoliation processes occurred in a vortex fluidic device in which a rapidly rotating 10 mm glass tube inclined at 45° (Figure 2.9a). The shearing in the film derives from the interplay between centrifugal and gravitational forces. The fluid formed a thin steam which is in parabolic shape and approximates to a thin film along the tube at high speeds. The thin steam gives rise to a shear force to partially lift the layers, and then the layer slippage and exfoliation ensue. A noticeable increase in the yield of exfoliation was observed when the tube inclined at 45° and the highest yield achieved with the rotation speed of 8000 rpm at this inclination angle. It's proposed that this method may be applicable for the cleavage of other two dimensional materials in a controlled condition.[69]

With the similar mechanism, high pressure microfluidization process is an alternative but sophisticated method, enabling large-scale production of few-layered BNNS by shear fluid. The working principle shown in Figure 2.9b is that the dispersion (DMF and chloroform as the solvents) enters the system through the inlet reservoir and an intensifier pump generates extremely high pressures to accelerate the product into the interaction chamber at velocities up to 400 m/s. The dispersion stream separates into micro channels of various geometries as narrow as the cross section of a human hair within the wide chamber. The dispersion stream is then forced to collide upon itself, which generates huge forces of impact and shear with several orders of magnitude higher than other technologies, *e.g.* homogenizator, sonicator and high-shear mechanical stirrer. Finally, the resultant product is cooled and collected in the output reservoir. This approach is highly efficient, completing one circulation in 0.6 min for 100 ml solution with a yield of 45%.[70]

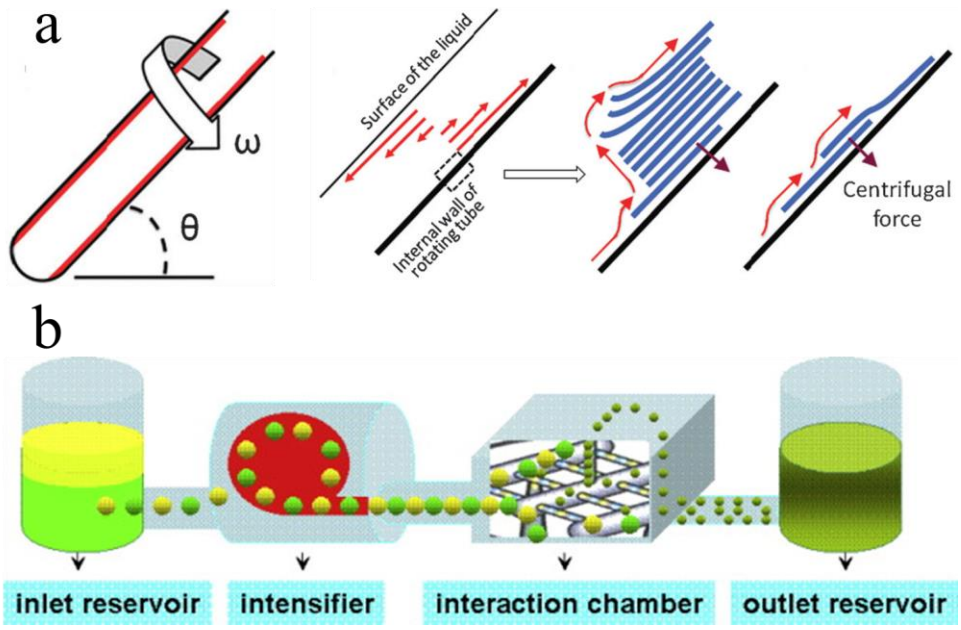

Figure 2.9. a) Schematic diagram of vortex fluid exfoliation of *h*-BN. b) Working principle of a microfluidizer processor.[69,70]

2.4.1.4 Blender shearing

To progress from the laboratory to the commercial applications, developing large-scale production methods for BNNS is necessary. Blender shearing technique is a practical scaling up exfoliation which can offer large quantities of defect-free BNNS (Figure 2.10). The mechanism of this process is that layered materials are exfoliated by high-shear laminar flow rather than the localized, turbulent, highly dissipative flow. Four main processing parameters, mixing time (t), mixing speed, (N), mixing volume (V) and rotor diameter (D), have been optimized. The maximum lab-scale production rate can reach 0.4 mg/s.[76, 77]

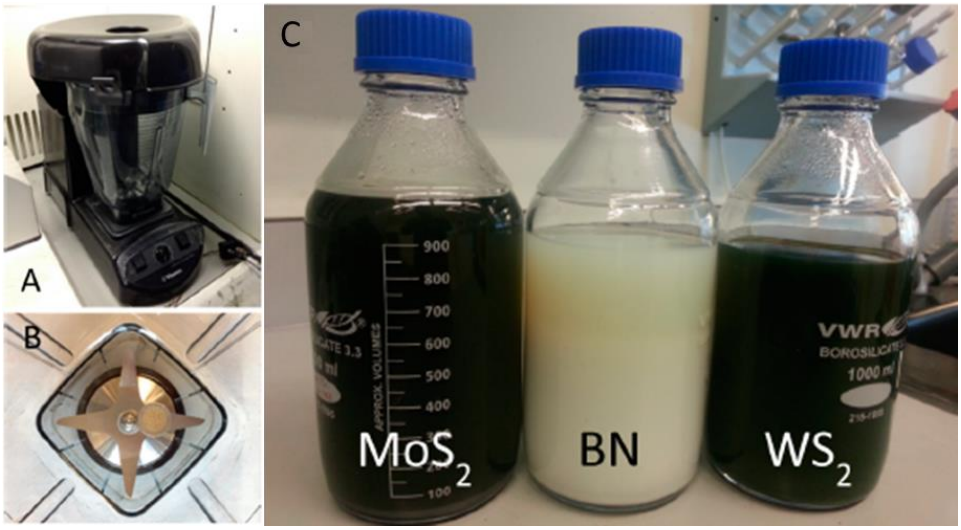

Figure 2.10. A and B) Photographs of the kitchen blender and its blade. C) Exfoliated dispersions of MoS_2, BN and WS_2.[77]

2.4.2 Sonication-based exfoliation

Essentially, sonication-assisted exfoliation is a way to cleave BNNS through ultrasonication energy in varied polar solvents, which are supposed to have the similar surface energy to that of *h*-BN. Few-layered and even mono-layered BNNSs have been isolated from the *h*-BN powder. This approach is facile without any sophisticated facilities and is scalable.

2.4.2.1 Exfoliation in organic solvents

According to the previous work of Hernandez et al [31] and Zhi et al[47], DMF (surface energy 37.1 mJ/m^2) exhibits polar-polar interaction with the *h*-BN surface to effectively peel BN particles away since its surface energy could overcome the van der waals forces between BN layers. The majority of BNNSs isolated are less than 7 nm with 52 BNNSs in a total of 73 nanosheets observed. Besides, those resultant BNNSs could be dispersed well in many solvents, such as chloroform with 0.3 mg/mL, DMF with 0.7 mg/mL. Resultant dispersions

were attractive since it is free of foreign materials rather than the solvent molecules compared to another route using Lewis bases like amine molecules, which complexes with boron atoms on *h*-BN surface.[78] Though they suggested that the surfaces are in an altered chemical status deriving from the somewhat interaction between *h*-BN and solvents, compared to the pristine *h*-BN, it was difficult to accurately determine the surface functional groups by means of Fourier transform infrared spectroscopy (FTIR), associated to the weak signal intensities and overlapped peaks reflecting the –OH, -NH, and –BN bonds.[47]

To build up a feasible methodology to efficiently screen the appropriate solvents, many other solvents have been tried and surface energy was the first parameter to be considered.[31, 79] However, exfoliation ability of solvents with similar surface tension diverges drastically.[31] Therefore, Hildebrand solubility parameter was further employed.[80] Nevertheless, the same issue occurs that many solvents with similar Hildebrand solubility parameter show the quite disparity of exfoliation abilities since the Hildebrand solubility parameters were only suitable for nonpolar systems.[32, 81] To more precisely explore the nature of the exfoliation process, Coleman et al applied Hansen solubility parameter, which denotes successful solvents to be those with dispersive, polar, and H-bonding components of the cohesive energy density within certain well-defined ranges. It's been demonstrated that layered compounds such as MoS_2, WS_2, $MoSe_2$, $MoTe_2$, $TaSe_2$, $NbSe_2$, $NiTe_2$, BN, and Bi_2Te_3 can be efficiently dispersed in varied solvents. Those layered materials are most effectively dispersed in solvents with specific surface tensions (close to 40 mJ/m^2 in all cases). This conclusion sheds light on how to search for new solvents and develop solvent blends.[32, 79]

From a different aspect, Shen et al claimed that Hansen parameters are still not accurate for predicting good solvents in that Hansen parameter is mainly applicable for solutes such as polymers. In order to efficiently predict the exfoliation abilities of solvent, surface tension components were directly probed and matched to predict solvents with effective liquid phase exfoliation capability for a range of 2D materials, *e.g. h*-BN, graphene, WS_2, MoS_2, $MoSe_2$, Bi_2Se_3, TaS_2, and SnS_2.[82, 83] It's been proposed that exfoliation efficiency is improved when the ratios of the surface tension components of the targeted solvent is close to that of the 2D materials in question, for example, 1:1 IPA/water for graphene, WS_2, *h*-BN and $MoSe_2$; 1:4 IPA/water for Bi_2Se_3, and SnS_2; 7:3 IPA/water for MoS_2, acetonitrile for TaS_2 (Figure 2.11).

Compared to other organic solvents, ionic liquids (ILs) feature unique properties such as nonvolatility, versatile solubility, and high thermal stability. Owing to those unique properties and closely matched surface energy, it's been used to effectively exfoliate graphite.[84] Alternatively, ILs are also expected to be an efficient exfoliation media for *h*-BN associated to their surface energies similar to those of *h*-BN. Additionally, interaction may occur between ILs and *h*-BN surface, which facilitates the exfoliation. This approach can reach a high yield of 50% and a high concentration around 1.9 mg/mL with a layer number less than 10. Interestingly, anions are found more strongly to affect the functionalization ratios (FRs) and concentrations. A clear anion effect on the FRs and concentrations was observed with the order: $[PF_6] > [Tf_2N] > [BF_4] > [TfO]$. This trend seems to be related to the order of anion basicity and hydrogen-bond ability. Among them, $[PF_6]$ anions screen [bmim] cations to a lower extent than other anions, leading to stronger cation-π interactions of BNNS surfaces with $[bmim][PF_6]$ compared to other ILs.[85]

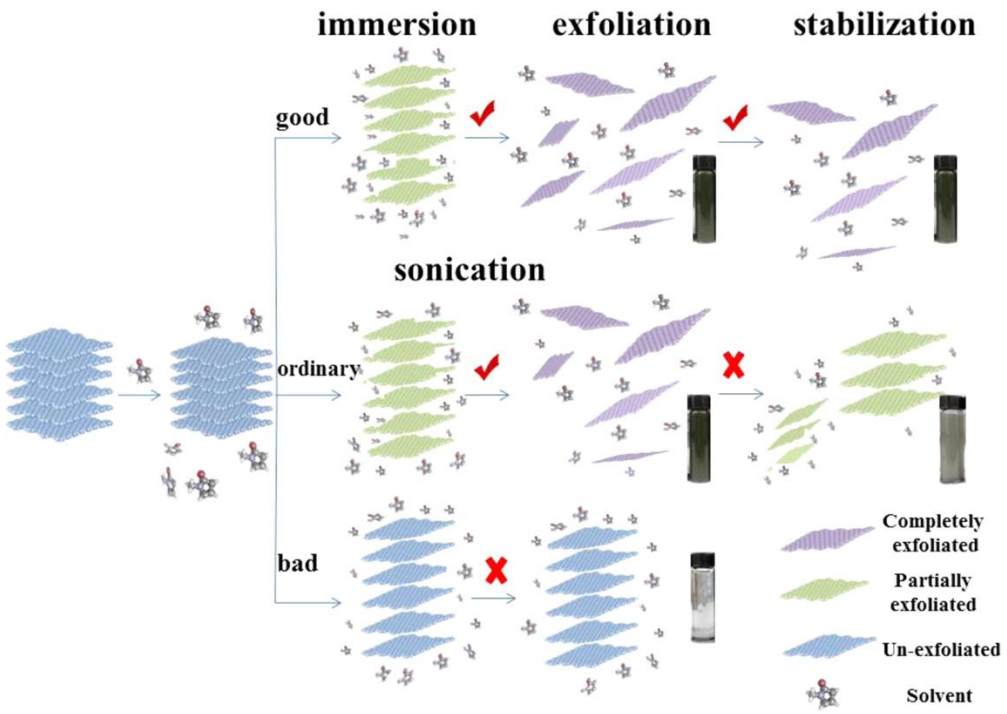

Figure 2.11. Proposed mechanism of liquid phase exfoliation (LPE) process. The efficient solvent for LPE should have surface tension similar to that of the aimed 2D materials.[82]

2.4.2.2 Exfoliation in water

Though *h*-BN is traditionally considered to be hydrophobic and the surface energy of water is much higher than that of *h*-BN, aqueous dispersion of few-layered and monolayered *h*-BNNS have been prepared through the sonication-assisted hydrolysis. The aqueous dispersion of BNNS is free of surfactants or organic functional groups (Figure 2.12). The aqueous dispersion of BNNS even exhibited strong affinity toward proteins such as ferritin, indicating that the nanosheet surfaces were capable of further bioconjugations. The mechanism of the exfoliation is largely based on the susceptibility of *h*-BN to hydrolysis. The whole process is divided into two parts. Initially, boron-nitrogen bonds near defect sites might be prone to attack by oxygen atoms from water molecules and defect further propagates until reaching the edges, resulting in the smaller sheets. Then the smaller sheets were exfoliated from the parent *h*-BN particle due to the combined contribution of mechanical agitation from

sonication and solvent polarity effect. The *h*-BNNS nanosheets have been obtained with different lateral sizes (up to ~1μm), which mainly depended on the initial *h*-BN samples as sonication-assisted hydrolysis promoted the cutting of large and thick *h*-BN sheet to smaller and thinner nanosheets.

Very recently, a modified aqueous exfoliation and dispersion of a series of 2D materials have been reported via temperature control sonication. Unlike the previous methods, an extra thermal energy is introduced via the dissipation of the sonic waves. This method allows the stable storage longer than one month if the high temperatures are maintained. The simulations suggest its good solubility is associated with the existence of platelet surface charges as a result of edge functionalization or intrinsic polarity. Although those 2D materials have dissimilar surface and physical properties, which result in quite varied dispersion mechanisms, in general, high temperatures favour both exfoliation and dispersion stability for all of them. [86]

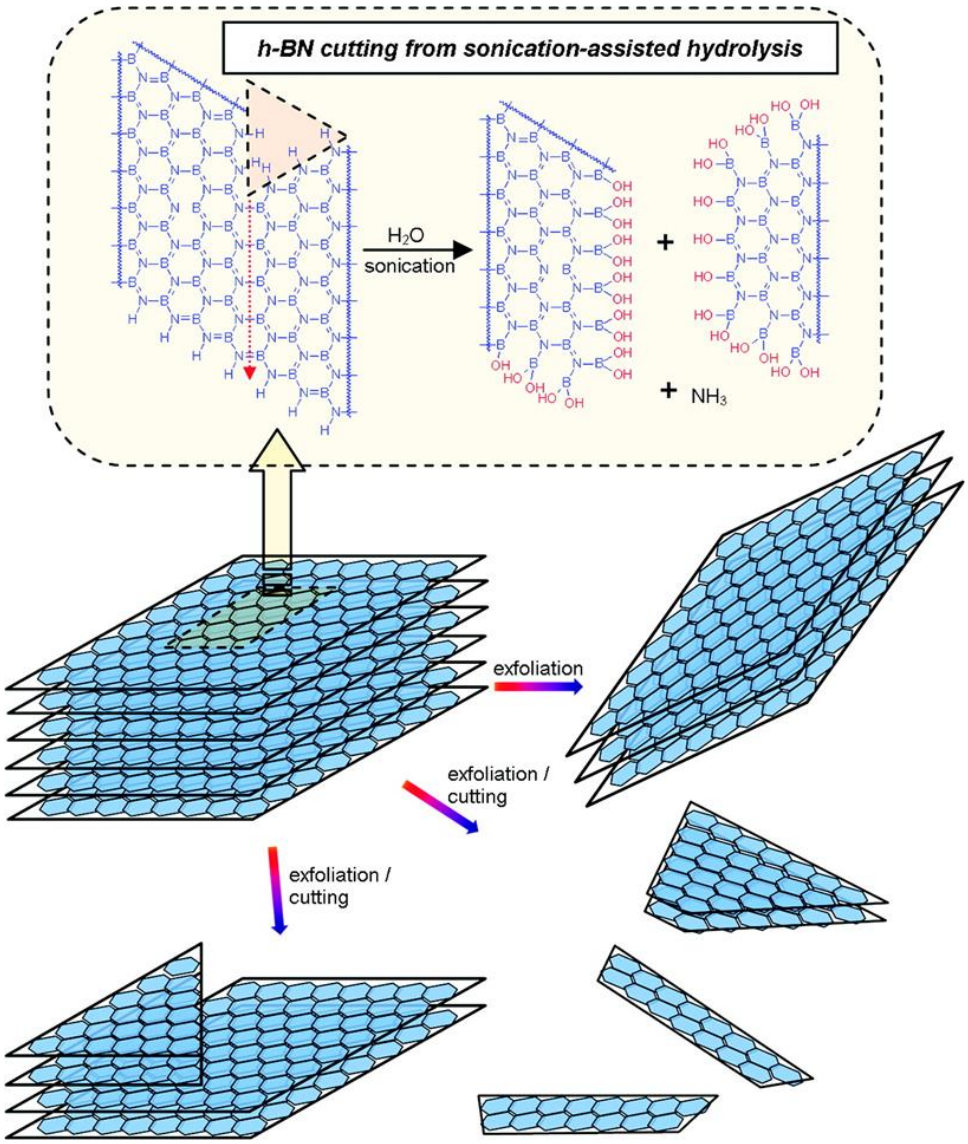

Figure 2.12. Schematics of exfoliation of *h*-BN via sonication-assisted hydrolysis.[28]

A simple co-solvents sonication-assisted exfoliation has been employed to produce BNNS from *h*-BN powder. It easily alters the surface energy by adjusting the ratios of the mixture solvents and enables avoiding working with those harmful or even dangerous solvents. In this study, solvents parameters, such as molecular weight (M.W.), boiling point, conformation, and safety considerations, have been selected. Methanol, ethanol, 1-propanol, 2-propanol, acetone, and *tert*-butanol were considered under these criteria (Figure 2.13). It was found that the co-solvent mixtures trump the results of the two liquids individually. The UV-vis results imply that 60 w/w% *tert*-butanol is superior at dispersing and retaining BNNS, with 2-

propanol and 1-propanol being second best, followed by ethanol, methanol and acetone. Those co-solvent mixtures were stable more than 2 months.[87] Interestingly, it's been found that the increase in absorbance of UV-vis is directly proportional to increasing M.W., but inversely proportional to surface tension. Obviously, surface tension is not the only key factor of effective exfoliation, and M.W. plays a great role. This may support the importance of the considering the Lennard-Jones potential between the surface of *h*-BN and the co-solvent system, indicating that larger solvent molecules more effectively stabilize the dispersed nanosheets than smaller solvent molecules.[88]

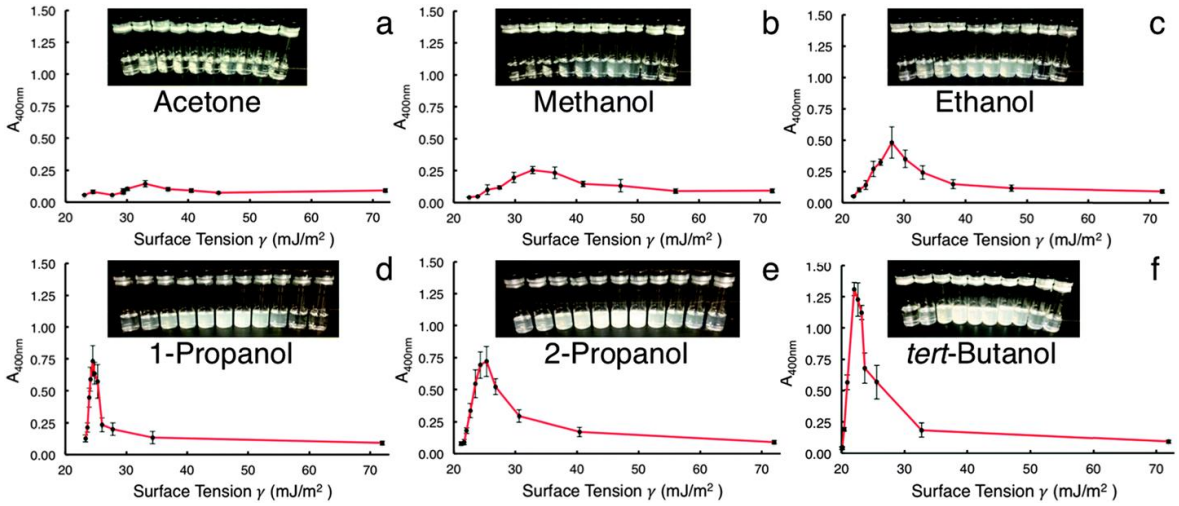

Figure 2.13. UV-vis results for BNNS in different co-solvent systems.[87]

2.4.2.3 Exfoliation in acid

Wet exfoliation methods have suffered from the low yield, which are mainly ascribed to the weak interaction between *h*-BN and the solvent molecules. Wang et al. used methanesulfonic acid (MSA), a strong protic acid, to exfoliate *h*-BN via sonication. The final concentration of BNNS in MSA can reach as high as 0.3 mg/mL, comparable to the results in other effective solvents.[89] Previously, protic sulfonic acids have been demonstrated that they are powerful solvents for those materials that hardly dissolve in common solvents, such as rod-like

polymers, nanotube and graphene.[90-93] Similar to the mechanism in their previous work, the solubilisation is attributed to the reversible protonation of the stiff polymer chains or graphitic carbon. MSA can also protonate *h*-BN, leading to isolated positively charged BNNS moieties associated with the local perturbation of electronic charges between *h*-BN interlayers. Additionally, the charges induce repulsive forces between BNNS and facilitate the dispersion process that aids the stability of the BNNS in MSA. Their hypothesis was supported by the occurrence of the orange colour due to the charge-transfer between BNNS and MSA molecules when the white mixture of *h*-BN and MSA was sonicated and subsequently the disappearance of the orange colour when the sonicated dispersion was exposed to air resulting from the adsorbed water acting as a competing base for deprotonation and precipitation of the BNNS in MSA and leaving a colourless supernatant. Besides, the results from FTIR and XPS indicate that the exfoliation process does not rise to oxidation of the BNNS.[89]

2.4.3 Chemical functionalization assisted exfoliation

Chemical functionalization has been demonstrated to be an effective way for the exfoliation of laminated materials, such as CNT,[94-97] BNNT bundles,[98-102] and graphite[103, 104] by surmounting the van der Waals forces that integrate the unit entities together. Similar strategy has also been tried to obtain *h*-BNNS.

Chemical functionalization can be divided into noncovalent, Lewis acid-base (ionic) and covalent categories. Essentially, bulky organic moieties are attached to the periphery of the *h*-BN and perhaps intercalate between the layers as well. When the functionalized *h*-BN is surrounded by a solvent, the solvation force induced by the attached functional groups

surmounts the van der Waals forces among the layers and exfoliate the bulk *h*-BN powder into BNNS. Those exfoliated BNNSs are prone to be dispersed in other organic solvents or water, ascribed to the functional groups attached.

2.4.3.1 Noncovalent functionalization

Followed by the success of preparing graphene nanoribbons[105], similar approach was applied to preparation of BNNS. The process was facile, placing 0.2 mg crystals in a 5 ml 1,2-dictoxy-*p*-phenylenevinylene) and followed by 1 h sonication. The duration was suggested be to an important factor that must be optimized for the yield and for minimization for the damage on the crystal structure of the BNNS.[106]

Many approaches have been proposed to modulate *h*-BN nanosheets upon non-covalent interactions.[107, 108] Basically, the polarity of the functional molecules is the key factor for its optimal orientation on the BNNS. Organic molecules have several advantages as surface dopants. A large number of organic molecules are available, and new ones can be customized and synthesized by incorporating the required functional groups, which can offer control over the molecular dipole moments, light sensing properties, hydrophilic or hydrophobic features. The most common electron acceptor (tetracyanoquinodimethane, TCNQ) and donor (tetrathiafulvalene, TTF) molecules have been introduced to noncovalently modulate the BNNS. The DFT computations (as shown in Figure 2.14) suggest that no chemical bonds form between BNNS and TCNQ/TTF as there are negligible changes in both complexes. The interactions between these interactive species are dominated by the weak dipole-dipole and electrostatic forces. In the lowest-energy configuration, TCNQ/TTF float atop the BN layer with heights of 3.49 Å and 3.68 Å respectively. The BNNS slightly crumpled from the flat

plane associated with the interaction from the TCNQ. In contrast, the BNNS is suffered from a serious distortion resulting from the adsorption of TTF. There is only small energy disparity between the most favourable and the less favourable doping sites for TCNQ and TTF, resulting in the easily overcome energy barrier for molecular migration, thus both TCNQ and TTF are easily mobile on the BN plane.[107]

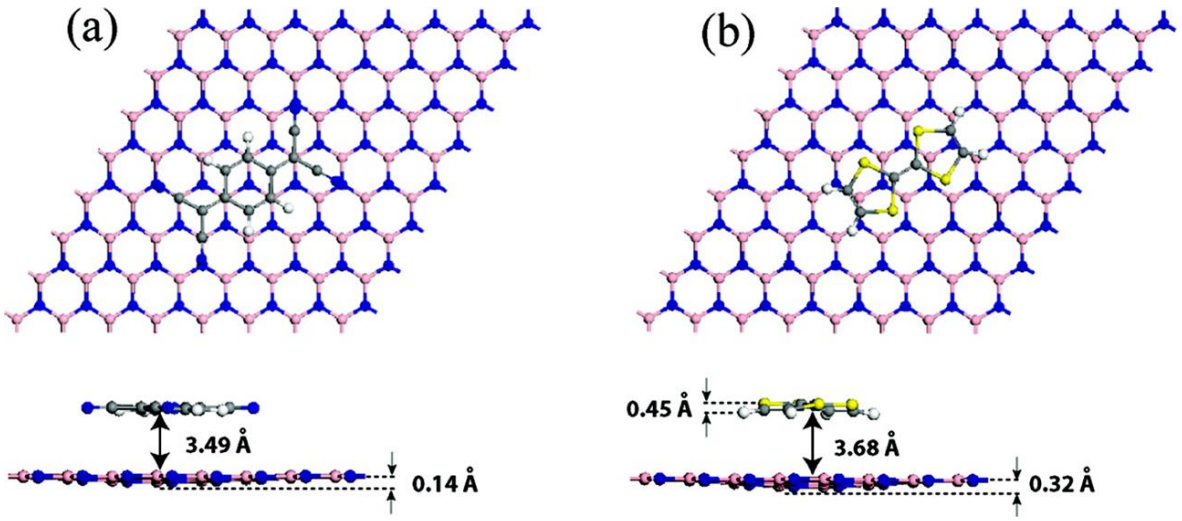

Figure 2.14. Top and side views of the lowest-energy configurations of the complexes between BNNS and TCNQ (a) and TTF (b). The distance between dopants and BNNS as well as distortion magnitude of the planar molecular or BNNS plane is also illustrated.[107]

Anchoring transition metals on *h*-BN has been widely studied theoretically, focusing on the potential applications in spin polarized transport and catalytic performance.[109-113] Nevertheless, an isolated metal atom tends to be very reactive due to the unsaturated valance and induced spin. Therefore, it's unlikely to dope a single metal atom on *h*-BNNS on a large scale. In this regard, metal-arene (denoted as MC_6H_6) group has been found to be a potential compound to functionalize *h*-BN. There are several advantages for MC_6H_6: (1) it's thermal stable and the synthetic routes are well established; (2) the metal atoms can maintain their formal zero oxidation state in the form of arene π-ligands and the π-systems of the ligands are

negligibly unperturbed. The chemical functionalization of *h*-BN with six metal-arenes (MC_6H_6, M=Ti, V, Cr, Mn, Fe, and Co) has been calculated and its found that MC_6H_6 can be stably adsorbed on the *h*-BN surface, with binding energies from 0.97 eV for (FeC_6H_6) to 1.4 eV (MnC_6H_6), depending on the content of the adsorbates. Additionally, the induced transition metal atoms from the adsorption of MC_6H_6 group enable the reduction of band gap of *h*-BN, resulting in the generation of the nonzero magnetic moments. Moreover, the adsorption of an O_2 molecule on *h*-BN is pronouncedly improved contributed to the MC_6H_6 functionalization.[108]

The *ab initio* calculations suggest that five nucleobase, including guanine (G), adenine (A), thymine (T), cytosine (C) and uracil (U), of DNA and RNA exhibit the same stacking arrangement on the BNNS, regardless of the their biological properties. The stable configurations are found to be different from those on metal surface[114, 115] or graphene[116, 117] (homogeneous templates). The N and O atoms of the nucleobases are prone to staying atop of B atoms of BNNS with a vertical distance of ~3.1 Å. The adsorption energies are in a sequence G > A > T > C > U, ranging from 0.69 to 0.5 eV. The noncovalent functionalization of the BNNS with the nucleobases, attributed to the electrostatic interaction generated by mutual polarizations (intra-molecule and intra -sheet charge re-distribution) of adsorbates and adsorbent, induces a moderate adhesive force to immobilize nucleobases on the sheet, which is slightly stronger than the π-π interaction the graphene and nucleobases but does not damage intrinsic properties of BNNS and nucleobases.[118] Such a DNA/BN hybrid is highly potential for the biological application in different environments.

2.4.3.2 Covalent functionalization

Covalent functionalization has a stronger bonding force and it's been demonstrated that polymer composite with covalently functionalized BNNS exhibited superior physical performance enhancement compared to using noncovalently functionalized BNNS.[119] Therefore, it's more promising to induce covalently functionalized BNNS as a nanofiller to impart their remarkable properties into composites. With this in mind, hydroxylated BNNS (OH-BNNS) was prepared by organic molecule functionalization and subsequent oxidation of the organic peroxide.[62] In this work, exfoliated BNNS was selected as the initial reactant by sonication-assisted exfoliation. The exfoliated BNNS was then mixed with organic peroxide, liquid di-*tert*-butylperoxide reagent, in a sealed high pressure autoclave vessel and *tert*-butoxy radical species were grafted on BNNS by the subsequent thermolysis of organic peroxide. Finally, whereby the piranha solution (H_2SO_4:H_2O_2, 3:1) can hydrolyze organic *tert*-butoxy groups to obtain OH-BNNS. The resultant OH-BNNS became much more active than the pristine *h*-BN. The hydroxyl groups are not only on the edges but also on the basal plane of BNNS according to the calculation from the TGA result. The functional group that is conducive to the better integration to the polymer chains allows the fabricated composites consequently exhibiting substantial mechanical improvement.

Aggressive oxidants were also used to functionalize and exfoliate *h*-BN, resulting in the yield of BNNS as high as 25% with 1-4 layers thick[120]. This deep functionalization even led to a dramatic decrease in band gap (3.9 eV). There are other methods to exfoliate and functionalize *h*-BN by using aggressive reagent, such as ammonium fluoride (NH_4F)[35] and fluoboric acid (HBF_4).[121] As a result, few-layered fluorinated BNNS have been fabricated with significantly reduced band gap, leading to generating new properties, *i.e.* magnetic property and electrical conductivity, which is not exist in the pristine *h*-BN. Mechanistically,

F ions tend to chemically bind to the B atoms on the surface of *h*-BN, forming the sp^3-hybridized B atoms that extrude out of the basal plane of *h*-BN. Driven by the sp^3-hybridized B atoms underlying F ions, the planar *h*-BN begins to curl, resulting in buckling of the outmost *h*-BN layer. Finally, the diffusion of the intercalated ammonium ions exfoliates the *h*-BN into BNNS.

h-BN is thermally stable at about 1000 ℃ in open air, but starts to degrade at the higher temperature to form boron oxide. Intrigued by this tendency, a novel route for large scale thermal exfoliation and functionalization *h*-BN has been reported.[122] It's a simple procedure that *h*-BN is heated at 1000 °C in air and the resultant product is purified by hot water and then dried. The hydroxyl group attached on the BNNS has been verified by FTIR spectra and XPS, which enhances the dispersibility of BNNS in solvent, up to 0.3 g L^{-1}. A large amount of small monolayer BNNS has been produced based on the AFM result.

Whereby sodium hydroxide/potassium hydroxide (NaOH/KOH) is eutectic at ~200 °C, its melts used to prepare cuprates[123] and nanostructures of complex functional oxide.[124-126] Recently, it's been proposed that NaOH/KOH melts was used to exfoliate bulk *h*-BN powder.[28] Thin and folded nanosheets, randomly overlapped flat nanosheets, and randomly scattered nanoscrolls were observed. The exfoliation is achieved by the following mechanism (Figure 2.15). Cations (Na^+ or K^+) adsorb on the outmost *h*-BN surface, leading to somewhat curling of *h*-BN near edges and steps. The self-curling of the outmost *h*-BN layers enlarges the interlayer spacing near the sides and promotes the subsequent insertion of cations and anions. Then anions (OH^-) adsorb on the positively curved surface and facilitate continuous

curling of the *h*-BN layer, followed by the peeling off BNNS from parent *h*-BN by the reaction of *h*-BN surface with hydroxide melts.

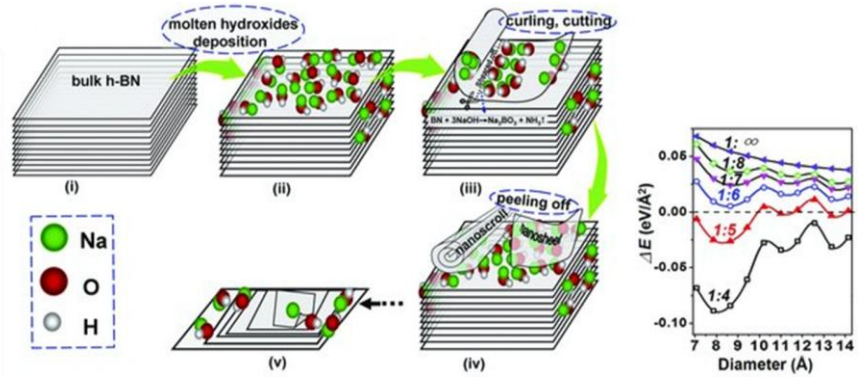

Figure 2.15. Illustration of the *h*-BN exfoliation by hydroxide melts.[28]

2.4.4 Substitution reactions

Ggraphite was tried as source materials to synthesize single-crystalline mutil-layered boron nitride with a thickness ranging from 5 nm to 40 nm.[127] Subsequently, another facile, low-cost biomass-directed method was developed by using diverse biomass sources via the carbothermal reduction of gaseous boron oxide species at 1500 °C under a N_2 atmosphere. Dandelion parachute, fleabane flower, pine needles and even large-mesh wiper papers have been used as the sources. Single crystalline, laterally large and atomically thin BNNS has been obtained with remaining the same macroscopic shapes of the original biomasses (Figure 2.16).

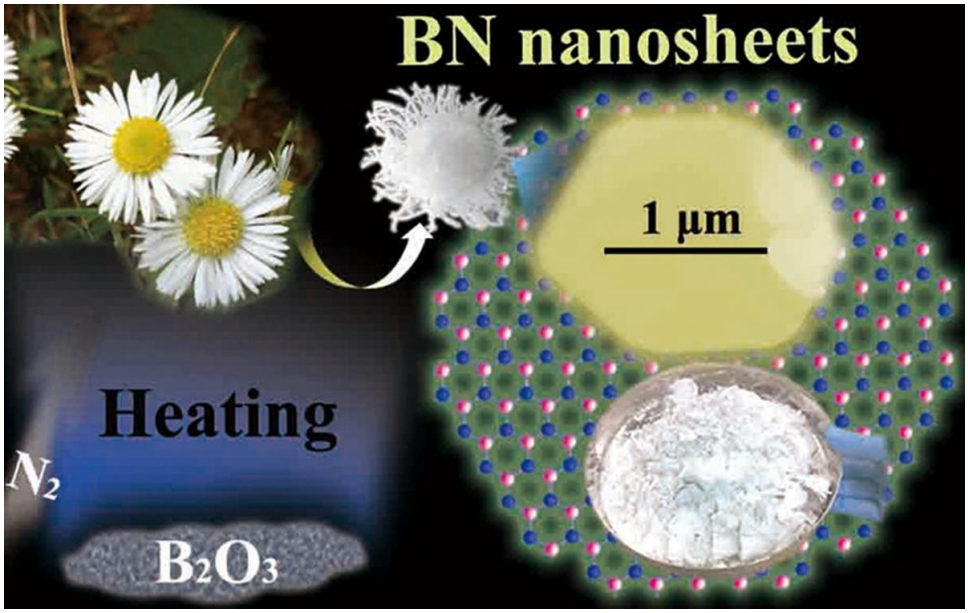

Figure 2.16. Illustration of biomass-directed synthesis of high-quality *h*-BNNS.[127]

2.4.5 Unzipping BN nanotubes

Unzipping CNTs through catalytic cutting or plasma etching has been developed to prepare high-quality graphene nanoribbons (GNR),[128-130] and the achievement of unzipping BN nanoribbons (BNNR) was ensued by unwrapping multiwalled BNNT (MWBNNT) through delicate plasma etching.[131] The MWBNNT were deposited on a Si substrate and spin-coated on a thin PMMA film. Subsequently, the PMMA/BNNT film was subjected to Ar plasma etching, followed by the removing PMMA by acetone vapour and further calcination at 600 °C for 6 h. Since the side and bottom parts of BNNT was initially embedded in the PMMA film, the plasma only etched the top part of BNNT, giving rise to the BNNT unzipping through cutting top walls.

Another unzipping method for the production of high-quality BNNR is through the corrosion and unzipping of BNNT by ammonia solution.[132] BNNT was severely corroded with end-

cap removed, tip sharpened, sidewall thinned, length shortened and also partial or even full longitudinal unzipped.

An *in-situ* unzipping concept was put forward for the scalable preparation of high-quality BNNR recently.[133] BNNR is fabricated by longitudinally unzipping BNNT during the BNNT synthesis process and the resultant BNNR has a good crystallinity, high chemical purity and few defects. Specifically, amorphous boron powder was first ball-milled in anhydrous ammonia gas and the resultant B powder was blended with lithium oxide (Li_2O) powder at a certain ratio. The blended powder was placed in an alumina crucible and heated at 1200 °C in NH_3 atmosphere for 3 h. A fluffy white powder was formed with an unzipping (BNNR/BNNT) ratio of more than 40%. The yield of the BNNR is able to be improved to approximately 60% after sonication and centrifugation. The author proposed that the unzipping is ascribed to the Li-NH_3 species rather than the individual Li, which may penetrate into BNNT on defect sites and intercalate into the interlayer of BNNT, expanding the interlayer spacing so that the BN sp^2 bonds break. With the assistance of the strain in nanotube,[130] the bond breaking can extend along the BNNT to form BNNR.

2.4.6 Solid-state reactions

The most common and scalable synthetic route of *h*-BN is solid state reaction, which has been extensively adopted by industries. A boron precursor, such as B_2O_3 or H_3BO_3, and a nitrogen source, such as melamine, urea, N_2 and NH_3, are the common reagent for the preparation.[134] Using the reactions of boron oxides with either urea or melamine, and boric acid with urea, high-yield *h*-BNNS with varying thickness in a range of 25-50 nm, diameters of 800-1000 nm and a surface area of 172 m^2g^{-1}, have been produced through a simple

template- and catalyst-free chemical vapour deposition process at 1100-1300 °C under nitrogen gas flow[135]. Nag et al[136], using almost the same way but with boric acid and urea at a lower temperature at 900 °C for 5h, suggested that the thickness of *h*-BNNSs could be controlled by having varied the relative proportions of the two reagents. They achieved *h*-BNNS with a majority of 1-4 layers and the high value of surface area of 927m^2 g^{-1} when the boric acid/urea ratio was 1:48, which exhibited high CO_2 adsorption but a negligible H_2 adsorption. Another approach to prepare *h*-BNNS of ~35 nm in thickness was that a mixture of B_2O_3 and melamine was heated at 1200 °C under N_2.[137] Alternatively, a slurry of boric acid, sodium azide, ammonium chloride, and urea was calcinated and the resultant disordered BN was annealed subsequently, resulting in the *h*-BNNS with a thickness of ~30 nm and lateral size of hundreds of nm.[138] *h*-BNNS nanoflowers were synthesized in a solid state reaction of $NaBF_4$, NH_4Cl and NaN_3 in the autoclave at 300 °C for 20 h.[139] In order to decrease the thickness of the *h*-BNNS, sublimed sulfur (S) was introduced into the reaction.[140]

A novel synthetic route, “chemical blowing”, which is quite different from the methods mentioned above, has been proposed by simply heating ammonia borane (AB) under Ar flow through multistage process.[141] BN or C_x-BN sheets with a thickness ranging from mainly 1 to 5 nm has been synthesized, relying on making large bubbles with atomically thin B-N-H (or B-N-C-H) polymer walls by releasing hydrogen gas from AB, somewhat resembling blowing a balloon. A high yield about 25% of mono- and few-layered BN or C_x-BN sheets were produced after annealing at high temperatures and collapse of the polymer bubbles.

Micrometre-scale *h*-BN sheets have been precipitated on a Ni substrate using cubic BN (c-BN) granules as seeds under nitrogen and hydrogen gas flow.[142] Since there is a discrepant solubility for boron and nitrogen in the nickel at the high temperature, specifically 0.3 at% for boron and almost no solubility for nitrogen in solid nickel at 1085 °C respectively, boron dissolves in nickel at high temperatures prior to its re-solidification on nickel surface, followed by the reaction with nitrogen flow gas to form *h*-BNNS on the nickel grains. Another similar way has been done by Suzuki et al[143] who has grown atomically thin *h*-BNNS on both surfaces of a polycrystalline Co (Ni)/amorphous BN/SiO_2 sandwich structure under vacuum with the thickness of 1-2 nm (3 to 7 layers) on the Co substrate and 1 nm (3-4 layers) on the Ni substrate respectively.

2.4.7 Chemical vapour deposition (CVD)

CVD method has often been employed to grow large-area *h*-BN films by the decomposition of precursors on metal or graphene substrate under Ar/H_2 gas flow as a carrier gas. The earliest study on the subject was published in 1968, in which diborane and ammonia as precursors for the deposition of *h*-BNNS on various substrates (Si, Ta, Mo, Ge, and fused silica) in temperature ranging from 600 to 1080 °C.[144] Many review papers have summarized various CVD synthesis of *h*-BNNS.[15, 145-147] Essentially, the precursors for *h*-BNNS could be either separate B and N compounds (i.e. BF_3-NH_3, BCl_3-NH_3, B_2H_6-NH_3), or a single precursor (ammonia borane, borazane, and borazine). Although those single precursors are water- and air-sensitive, they are desirable due to low toxicity and the inherently defined 1: 1 of B : N stoichiometry.

Auwarter et al[148] used b-trichloroborazine, which has a higher stability than ammonia borane to offer a slower and more steady decomposition reaction that allows a long and continuous interaction between decomposed gases and nickel surface. Monolayer *h*-BNNS has been obtained with below 3% of Cl coverage in one monolayer. Ye et al[149] coated *h*-BNNS on SiBNC fibers by the deposition of borazine which is free of C and O. In their study, they found that using ammonia is the prerequisite to crystalline *h*-BNNS deposition at ambient pressure. Otherwise, extensive amorphous coatings were obtained .The optimal temperature for the *h*-BNNS deposition was 1090 °C, as borazine is unstable at higher temperatures. Shi et al[150] flowed borazine vapour by N_2 gas under an ambient pressure at a low temperature of 400 °C with an post annealing process at 1000 °C which facilitates the further dehydrogenation of borazine and leads to a better crystalline *h*-BN. Varying thickness of *h*-BN films have been grown by increasing the flow rate of borazine and reaction time. Ismach et al[151] issued a facile and rational way to synthesize high-quality *h*-BN films with controlled number of layers from diborane and ammonia under a low-pressure chemical vapour deposition (LPCVD) growth system. He found that the sequence of dosing precursor played an essential role in the number of *h*-BN layers and impurity with 1-5 layers for diborane-first where the presence of B-Ni and B-O bonds were detected by XPS, but 2-4 layers for ammonia-first where no trace of N, Ni-N, B-O, and B-Ni was found. Diborane has also been used for the production of *h*-BNNS by plasma-enhanced CVD method[152] accompanied by ammonia gas, but the film presented a mixture of *h*-BN and amorphous phases or in certain circumstance, *c*-BN. An alternative borane, decaborane, [153] has been tried to form *h*-BNNS via decaborane/ammonia reactions on Ni and Cu substrate since decaborane is known to react with many metals at high temperature to form metal boride which could be involved in providing the initial seeds for *h*-BNNS growth. Films on Ni were ~2 nm thick but 2~15 nm thick instead on Cu under the same deposition condition. Ammonia

borane, which is a crystalline solid and melts at around 106 °C, is the most ideal precursor that shows many advantages including the stability in the air environment, 1:1 B/N stoichiometry, free of foreign elements like C, Cl, F and O, and not toxic compared with other boron containing precursors such as BF_3 or BCl_3. Song et al[46] sublimed AB to grow large scale atomic *h*-BNNS with 2-5 layers which showed an excellent mechanical properties with elastic modulus ranging from 200 to 500 N/m. Kim et al[154] also used ammonia borane as a precursor and synthesized monolayer *h*-BNNS using CVD with two heating zones under low pressure (LPCVD). Compared to previous atmospheric pressure CVD synthesis, in LPCVD condition, the growth is preferentially limited and less affected by the geometry of the substrate and gas flow effect. Lee et al[155] who has grown *h*-BNNS on polycrystalline Ni foil using ammonia borane as B and N source, found that Ni (100) facets promoted the growth of *h*-BN but the growth on Ni (111) surfaces was negligible.

Tuneable growth of *h*-BNNS can be obtained on polycrystalline Pt foils usingwith ammonia borane as the precursor.[156] By simply altering the concentration of ammonia borane, monolayer, bilayer and few-layered *h*-BNNS was synthesized. The mechanism for preparation of the predetermined layers of *h*-BNNS is proposed as follows. At 70 °C, the decomposition of borazane is weak, and the product quantity is close to the balance point that needs for *h*-BNNS growth. At this stage, the *h*-BNNS growth follows a Frank van der Merwe model associated with the adatom-surface (Pt) interaction, resulting in the formation of monolayer *h*-BN domains and films. When the temperature is increased to 75 °C, the bilayer nucleus forms ascribed to the increased quantity of borazane decomposition. The growth of few-layer *h*-BNNS at 80 °C resembles to bilayers.

In a recent study, monolayer *h*-BNNS was prepared on a whole Pt foil (2×5 cm^2) under 100 mTorr with the size being limited only by the initial Pt foil size. The orientation of Pt foil lattice plane and total pressure were the crucial parameters for thickness control.[157] At high pressure, a thick *h*-BNNS tends to be grown on Pt (111), while thin *h*-BNNS was preferentially grown on Pt (001) (Figure 2.17). It's been explained that Pt (111) surface has the higher density of the Pt atoms than that of the Pt (001) surface, resulting in a more efficient decomposition of the borazine precursor.

Recently, our group have developed a novel synthetic route for large and homogenous *h*-BNNS.[158] A comparative study has been conducted, which suggests that melted copper is a better catalyst substrate than solid copper. Single crystalline monolayer and bilayer *h*-BNNS with a lateral size of several microns were obtained on melted copper whereas polycrystalline and mixed multiple layers (1-10) were found on solid copper. This difference may be due to the small amounts of uniformly distributed nucleation sites on the smooth melted surface, in contrast to the large amounts of unevenly distributed nucleation sites on the grain boundaries and other defects on the solid copper surface.

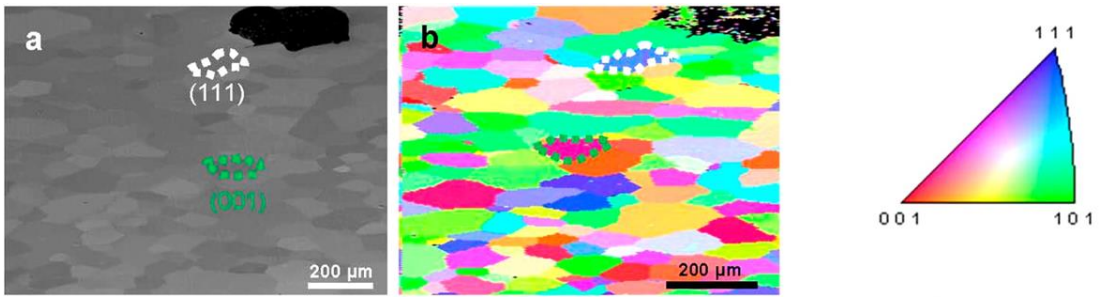

Figure 2.17. The effect of Pt crystal orientation on *h*-BNNS growth. a) SEM image of *h*-BNNS on Pt foil. The white- and green-dotted lines indicate the Pt (111) and (001) region, respectively. b) EBSD image of the same region as (a) and the EBSD legend.[157]

2.5 Properties and Applications

h-BN has a variety of advantageous physical properties, such as electrical insulation, high thermal and chemical stability, high thermal conductivity, and excellent mechanical properties, all of which entail a series of applications.[15, 146] The most promising application is as the dielectric substrates in graphene electronic devices. Moreover, *h*-BNNS is widely utilized as multifunctional composite fillers and sensor substrates.

2.5.1 Electronic properties and applications

Graphene devices on standard SiO_2 substrates are highly disordered, exhibiting characteristics that are far inferior to the intrinsic properties of graphene.[159] However, graphene devices on *h*-BN substrates have mobilities and carrier inhomogeneities that are almost an order of magnitude better than on SiO_2. This is ascribed to its atomically smooth surface that is relatively free of dangling bonds and charge traps, and its large optical phonon modes, wide band gap (5~6 eV) and similar lattice constant to that of graphene. Atomically few-layered BNNS-graphene heterostructures have exhibited extraordinary charge mobility as high as 60,000 $cm^2\ V^{-1}\ s^{-1}$, three times larger than that on SiO_2.[160] Another heterolayered configuration (C-BN-C) has utilized field-effect tunnelling transistor devices, where two graphene layers are separated by a thin *h*-BNNS.[161] Measurements of the electron tunnel current through *h*-BNNS suggest that they are good tunnel barriers down to a single atomic layer. [162]

Owing to the wide band gap of BNNS in both lateral and through-thickness directions, the theoretical studies on the electronic band gap and magnetic properties of 2D BN nanostructures have been mainly focused on BNNR, albeit there are only a few of low-yield synthetic methods available.[131-133, 163, 164] Resembling to GNNR, BNNR with either zigzag or armchair edges exhibits much enhanced quantum confinement due to the edge effect with anisotropic electronic or magnetic properties that are not present in BNNS. Band gap of zigzag BNNR is indirect and decrease monotonically with increasing ribbon width whereas the armchair BNNR experiences typical direct gap oscillation with distinct family behavoir.

Band gap tuning of BNNR and BNNS might be achieved by the application of planar strain[165, 166] or by hydrostatic pressure in the GPa range.[167] The band gap modulation of BNNR often gives rise to a change in magnetic properties. While bare zigzag BNNR was found to be magnetic semiconductors with spin-polarized states localized along the edges,[168] it may be turned into half-metals via a directional external electric field. Hydrogen modification of BNNR may also induce pronounced changes in electronics and magnetic properties but in different way for zigzag and armchair BNNR. Specifically, hydrogen-modified armchair BNNR remain nonmagnetic semiconductors whereas zigzag BNNR counterpart displays half-metallicity and becomes ferromagnetic metals with either hydrogen termination merely at the B edge[14, 169] or full surface hydrogenation.[170] A gradual transition of zigzag BNNR from a nonmagnetic semiconductor to a ferromagnetic metal could be achieved by tuning the degree of hydrogenation.[170]

It's been reported that it is experimentally feasible to use hydrogenation for band gap reduction of BNNS. [171] The measured band gap of BNNS was decreased from 5.6 eV to 4.25 eV after subjected to 250 s of hydrogen plasma treatment. Additionally, a theoretical study suggests that fluorine (F) is capable of functionalization of BNNS, making insulating BNNS semiconducting.[172] The fluorinated BNNS have been prepared by treating BNNS with HBF_4 and the insulating BNNS was successfully transferred to the semiconducting fluorinated BNNS.[124] More interestingly, *h*-BN powder was directly fluorinated and exfoliated by NH_4F in autoclave at 180 °C for 24 h, and the fluorinated BNNS exhibits magnetic property induced by the F-BN_3 bond.[35] This is becuase that fluorination can induce electron spin polarization in nonmagnetic BNNS. The magnetic moment of fluorinated BNNS mainly comes from the electron spin-polarization of the F and the three N atoms nearest to the sp^3-hybridized B atom underlying the F atom.

2.5.2 Thermal properties and applications

Many groups have calculated thermal conductivity (κ) values of *h*-BN, ranging from 300 to 2000 W m^{-1} K^{-1},[173-176] which are much larger than that of most of metallic and ceramic materials. Counterintuitively, *h*-BN κ values are somewhat lower than that of graphene (1500-2500 W m^{-1} K^{-1}), though they share similar crystal structures, lattice constants, unit cell masses, and phonon dispersions. This disparity may be ascribed to the softer phonon modes for BNNS and the mass difference between B and N.[173] The theoretical studies suggest that a predominant contribution of the κ value is from out-of-plane vibrations of BNNS. Monolayer BNNS therefore has a substantially higher κ value than few-layered BNNS associated with decreased interlayer phonon scattering. The κ value decreases with increases in layer number eventually converging to the value of *h*-BN.[175, 176] BNNR exhibit inferior κ value than BNNS, resulting from the edge-induced phonon scattering.[173]

As zigzag and armchair BNNR show different extent of scattering effect, the κ value of the former considerably higher than the latter.

As an insulator with high thermal conductivity and remarkable chemical inertness, *h*-BN possesses more merits than other conventional heat-transfer materials. It shows a great potential as thermal filler. However, according to the theoretical calculation, layered BN shows a significant anisotropy, which leads to its high thermal conductivity being pronounced along the (002) planes. To maximize the exposure of (002) planes, researchers tried to choose nanotubular and nanoshperical *h*-BN as fillers to utilize the thermal advantage of *h*-BN. Zhi et al.[177] improved the thermal conductivity of water up to ~2.6 times by using the combination of BNNT and BN nanospheres which also reduced the viscosity of fluid. Exfoliated *h*-BN with maximum exposure to these (002) lattice plane has been tried. [178] It's been reported that thermal conductivity of mineral oil with 0.1 wt% exfoliated *h*-BN was improved from 80% to 100% at 373K.

2.5.3 Mechanical properties and applications

Graphene has been suggested as one of the toughest material according to the theoretical calculations and experimental results, with calculated and measured Young's moduli of 1.05-1.24[179-181] and 1 Tpa,[182] respectively. As structurally analogous to graphene, *h*-BN is predicted to be equally strong and resilient. As calculated, the in-plane stiffness values of a monolayer BNNS and graphene are similar, being 267 and 335 N m^{-1}, respectively.[183] The mechanical properties of BNNS have been investigated by nanoindentation measurements using atomic force microscopy (AFM).[46] To be specific, circular wells with diameter around 1μm were patterned onto a silicon substrate and BNNS were then transferred on to the

prepatterned substrates. The mechanical properties of BNNS were investigated by indenting the centre of each freestanding membrane with a diamond tip. The tested results for BNNS with thickness of 1-2 nm are in the range of 220-510 N m^{-1}, which are smaller than the theoretical value (270 N m^{-1} for monolayer BNNS), largely attributed to the layer distribution of stacking faults in the CVD synthesized films or the error in estimating the exact size of the holes and the position of membrane contact with the substrate.

Owing to its exceptional mechanical properties, *h*-BN is a potential reinforcement material in composites with ceramics or polymer matrices. Zhi et al.[47] fabricated BN composites with PMMA and the resultant composites exhibited a 22% improvement in the elastic modulus of PMMA, an 11% increase in its strength and a remarkable enhancement on thermal conductivity by utilizing only 0.3wt% BNNSs fraction. Wang et al.[184] developed chemical blowing concept to produce high-yield boron nitride nanosheets and fabricated polycarbonate (PC)/BN and polymethylmethacrylate (PMMA)/BN composites with 22% and 17% increase in elastic modulus and 35% and 32% improvement in yield strength, respectively by adding 2 wt% BN fractions.

2.5.4 Wetting properties and applications

Wetting is the ability of a liquid to maintain contact with a solid surface. In general, if the water contact angle is smaller than 90°, the solid surface is considered hydrophilic and if the water contact angle is larger than 90°, the solid surface is considered hydrophobic. Some materials have a water contact angel even higher than 150°, which is considered superhydrophobic surface. Essentially, the wettability of a surface depends on its chemical composition and microstructural geometry.[185-192] Smooth *h*-BN film is relatively

hydrophilic with a water contact angle (CA) of ~50°, while morphology-modified *h*-BN surfaces can be hydrophobic or even superhydrophobic.[187] This significant transition in wettability is based on the combined effects of surface roughness and partial liquid-solid contact area at the interface.

Quantum molecular dynamics (QMD) simulations have shown the contact angles of monolayer BNNS and graphene are nearly same (86° and 87°, respectively). However, simulation of a water droplet on the wrinkled single layer BNNS shows a notably smaller contact angle. The varied wettability of the BNNS can be assigned to the polar nature of B-N bonds that promote the interaction with polar water molecules on the wrinkled BNNS surface. Additionally, the experimental results have also demonstrated that BNNS show higher hydrophilicity than the simulated results, with smaller contact angles of 51-67°.[186, 192]

2.5.5 Piezoelectricity

The symmetry dependant properties make atomically thin monolayer BN piezoelectric, whereas the bulk parent crystal is not. It has been discovered that a bilayer exhibits a strong mechanical coupling between curvature and electric fields.[193] Density functional theory suggests amplified in-plane piezoelectric displacements in bilayered BN by exceedingly large factors on the order of 10^3-10^4. This newly discovered electromechanical coupling to very small radii of curvature in *h*-BN is an emergent property of bilayers, which may also occur in other materials, including the semiconducting transition metal dichalcogenides.

2.5.6 Field emission

It has been experimentally demonstrated that BNNT is able to emit electrons from their tips under extremely strong electric fields.[194] With novel morphologies, layered *h*-BN could exhibit different properties when compared to bulk *h*-BN or BNNT. A novel form of porous BN nanoshperes, consisting of interconnected BN channels in the core, in addition to BN nanocones and protruding BN ribbons on their surface, exhibits surprisingly stable field emission properties at low turn-on voltages. These remarkable electron emission properties are due to the presence of finite zigzag BNNR located at the surface of the nanospheres that behave like metals. Similarly, BNNS protruding from BN fibres and Si_3N_4 nanowires have shown a low turn-on field of 1.9 and 4.2 V μm^{-1}, respectively.[195, 196]

2.5.7 Catalysis

Interaction between BN and the substrate may dramatically affect the chemical reactivity of the substrate. DFT simulations imply that adsorption and catalytic activation of O_2 on the *h*-BN supported Au and Au_2 can be influenced by the interaction with the support via electron pushing and donor/acceptor mechanisms.[138] This effect is ascribed to the mixing of the 5d orbitals of the supported Au and Au_2 with the N-p_z orbitals of *h*-BN. Although defect-free *h*-BN is inert and does not act as a good electron donor for the supported O_2-Au, it facilitates an electron transfer from Au to O_2. In the case of the defected *h*-BN surface, Au and Au_2 are trapped effectively by N or B vacancy and impurity point defects. Strong adsorption on the surface defects is accompanied by the large charge transfer to/from the adsorbate. The excess of the positive or negative charges on the supported Au and Au_2 can significantly enhance their catalytic activity. Experimental study has demonstrated that Au/BNNS and Pt/BNNS can be efficient catalysts in various reactions.[197] Especially, Pt/BNNS catalysts towards CO conversion have shown lower full conversion temperature and higher stability. In another

study, Ag/BNNS nanohybrid thin film coatings on quartz substrates were prepared and evaluated as reusable surface enhanced Raman spectroscopy sensors, which were robust when subjected to repeated solvent washing.[198] Additionally, with the unique thermal stability of BNNS, the sensor devices may be readily recycled by short-duration high temperature air oxidation to remove residual analytes in repeated runs.

2.5.8 Ecology

BNNS has been extensively studied for a variety of applications related to environment. For example, porous boron nitride has recently been studied for applications in gas and contaminants adsorption. B-N bond has ionic character that can induce an extra dipole moment, suggesting that hydriding/dehydriding properties of BN are stronger than those of graphite which has been considered as promising materials for hydrogen storage. Weng et al.[199] synthesized boron nitride porous microbelts with a high specific surface area of 1488 m^2g^{-1}. H_2 sorption evaluations demonstrate that those microbelts show high and reversible H_2 uptake from 1.6 to 2.3 wt% at 77 K and 1MPa. Nag et al.[143] produced BN nanosheets with a majority of 1-4 layers which exhibit high CO_2 adsorption, up to 32 wt%, but negligible H_2 adsorption. Lei et al.[26] utilized the excellent sorption properties of BN for water cleaning. The synthesized porous BN nanosheets exhibit remarkable sorption performances for a wide range of oils, solvents and dyes, with mass uptakes reaching 3,300%.

2.5.9 Other properties and applications

h-BN is excellent lubrication due to low friction attributed to the weak van der Waals bond in each layer. Besides, it was suggested that even single-layer *h*-BN could show low friction without sliding at contact interface between layers[200]. Cho et al.[201] reported that even

infinitesimal BNNS additive dispersed in water without any surfactants can diminish the amount of friction force and wear for a long time. Furthermore, combined with its high oil absorption, moisture binding effect and intensification of colour effects, *h*-BN is used in nearly all top-notch cosmetic products of foundation, make-up, eye shadow, blusher, kohl pencil, lipsticks and a host of other skincare products.

2.6 Reference

1. Balmain, W.H., XLVI. Observations on the formation of compounds of boron and silicon with nitrogen and certain metals. Philosophical Magazine Series 3, 1842. 21(138): p. 270-277.
2. Balmain, W.H., Bemerkungen über die Bildung von Verbindungen des Bors und Siliciums mit Stickstoff und gewissen Metallen. Journal für Praktische Chemie, 1842. 27(1): p. 422-430.
3. Iijima, S., Helical microtubules of graphitic carbon. Nature, 1991. 354(6348): p. 56-58.
4. Chopra, N.G., et al., Boron Nitride Nanotubes. Science, 1995. 269(5226): p. 966-967.
5. Yong Jun, C., Z. Hong Zhou, and C. Ying, Pure boron nitride nanowires produced from boron triiodide. Nanotechnology, 2006. 17(3): p. 786.
6. Yejun, Q., et al., Synthesis of continuous boron nitride nanofibers by solution coating electrospun template fibers. Nanotechnology, 2009. 20(34): p. 345603.
7. Zhang, H., et al., Conical Boron Nitride Nanorods Synthesized Via the Ball-Milling and Annealing Method. Journal of the American Ceramic Society, 2006. 89(2): p. 675-679.
8. Kroto, H.W., et al., C60: Buckminsterfullerene. Nature, 1985. 318(6042): p. 162-163.
9. Stéphan, O., et al., Formation of small single-layer and nested BN cages under electron irradiation of nanotubes and bulk material. Applied Physics A, 1998. 67(1): p. 107-111.
10. Golberg, D., et al., Octahedral boron nitride fullerenes formed by electron beam irradiation. Applied Physics Letters, 1998. 73(17): p. 2441-2443.
11. Novoselov, K.S., et al., Electric Field Effect in Atomically Thin Carbon Films. Science, 2004. 306(5696): p. 666-669.

12. Novoselov, K.S., et al., Two-dimensional atomic crystals. Proceedings of the National Academy of Sciences of the United States of America, 2005. 102(30): p. 10451-10453.
13. Chen, Z.-G., et al., Novel Boron Nitride Hollow Nanoribbons. ACS Nano, 2008. 2(10): p. 2183-2191.
14. Zheng, F., et al., Half metallicity along the edge of zigzag boron nitride nanoribbons. Physical Review B, 2008. 78(20): p. 205415.
15. Pakdel, A., Y. Bando, and D. Golberg, Nano boron nitride flatland. Chemical Society Reviews, 2014. 43(3): p. 934-959.
16. Warner, J.H., et al., Atomic Resolution Imaging and Topography of Boron Nitride Sheets Produced by Chemical Exfoliation. ACS Nano, 2010. 4(3): p. 1299-1304.
17. Ooi, N., et al., Electronic structure and bonding in hexagonal boron nitride. Journal of Physics: Condensed Matter, 2006. 18(1): p. 97.
18. Marom, N., et al., Stacking and Registry Effects in Layered Materials: The Case of Hexagonal Boron Nitride. Physical Review Letters, 2010. 105(4): p. 046801.
19. Ribeiro, R.M. and N.M.R. Peres, Stability of boron nitride bilayers: Ground-state energies, interlayer distances, and tight-binding description. Physical Review B, 2011. 83(23): p. 235312.
20. Blase, X., et al., Frustration Effects and Microscopic Growth Mechanisms for BN Nanotubes. Physical Review Letters, 1998. 80(8): p. 1666-1669.
21. Won, C.Y. and N.R. Aluru, Structure and Dynamics of Water Confined in a Boron Nitride Nanotube. The Journal of Physical Chemistry C, 2008. 112(6): p. 1812-1818.
22. Charlier, J.C., et al., Microscopic growth mechanisms for carbon and boron-nitride nanotubes. Applied Physics A, 1999. 68(3): p. 267-273.

23. Kwon, Y.-K., et al., Morphology and Stability of Growing Multiwall Carbon Nanotubes. Physical Review Letters, 1997. 79(11): p. 2065-2068.

24. Thomas, J., N.E. Weston, and T.E. O'Connor, Turbostratic1 Boron Nitride, Thermal Transformation to Ordered-layer-lattice Boron Nitride. Journal of the American Chemical Society, 1962. 84(24): p. 4619-4622.

25. Hamilton, E.J.M., et al., Preparation of Amorphous Boron Nitride and Its Conversion to a Turbostratic, Tubular Form. Science, 1993. 260(5108): p. 659-661.

26. Lei, W., et al., Porous boron nitride nanosheets for effective water cleaning. Nat Commun, 2013. 4: p. 1777.

27. Weng, Q., et al., Highly Water-Soluble, Porous, and Biocompatible Boron Nitrides for Anticancer Drug Delivery. ACS Nano, 2014. 8 (6), p. 6123–6130.

28. Li, X., et al., Exfoliation of Hexagonal Boron Nitride by Molten Hydroxides. Advanced Materials, 2013. 25(15): p. 2200-2204.

29. Lin, Y., et al., Aqueous Dispersions of Few-Layered and Monolayered Hexagonal Boron Nitride Nanosheets from Sonication-Assisted Hydrolysis: Critical Role of Water. The Journal of Physical Chemistry C, 2011. 115(6): p. 2679-2685.

30. Du, M., Y. Wu, and X. Hao, A facile chemical exfoliation method to obtain large size boron nitride nanosheets. CrystEngComm, 2013. 15(9): p. 1782-1786.

31. Hernandez, Y., et al., High-yield production of graphene by liquid-phase exfoliation of graphite. Nat Nano, 2008. 3(9): p. 563-568.

32. Coleman, J.N., et al., Two-Dimensional Nanosheets Produced by Liquid Exfoliation of Layered Materials. Science, 2011. 331(6017): p. 568-571.

33. Cui, Z., et al., Large Scale Thermal Exfoliation and Functionalization of Boron Nitride. Small, 2014. 10(12) p. 2352-2355.

34. Bhimanapati, G.R., D. Kozuch, and J. Robinson, Large-Scale Synthesis and Functionalization of Hexagonal Boron Nitride Nanosheets. Nanoscale, 2014. 6: p. 11671-11675.

35. Du, M., et al., One-Step Exfoliation and Fluorination of Boron Nitride Nanosheets and a Study of Their Magnetic Properties. Angewandte Chemie International Edition, 2014. 53(14): p. 3645-3649.

36. Blake, P., et al., Making graphene visible. Applied Physics Letters, 2007. 91(6): p. 063124.

37. Gorbachev, R.V., et al., Hunting for Monolayer Boron Nitride: Optical and Raman Signatures. Small, 2011. 7(4): p. 465-468.

38. Park, J.S., et al., band Raman spectra of single, double and triple layer graphene. Carbon, 2009. 47(5): p. 1303-1310.

39. Reich, S., et al., Resonant Raman scattering in cubic and hexagonal boron nitride. Physical Review B, 2005. 71(20): p. 205201.

40. Feng, X., et al., Controllable synthesis of few-layered and hierarchically porous boron nitride nanosheets. Chemical Communications, 2016. DOI: 10.1039/c5cc09348a.

41. Li, X., et al., Large-Area Synthesis of High-Quality and Uniform Graphene Films on Copper Foils. Science, 2009. 324(5932): p. 1312-1314.

42. Zaman, I., et al., A Facile Approach to Chemically Modified Graphene and its Polymer Nanocomposites. Advanced Functional Materials, 2012. 22(13): p. 2735-2743.

43. Wu, W., et al., Control of thickness uniformity and grain size in graphene films for transparent conductive electrodes. Nanotechnology, 2012. 23(3): p. 035603.

44. Bae, S., et al., Roll-to-roll production of 30-inch graphene films for transparent electrodes. Nat Nano, 2010. 5(8): p. 574-578.

45. Kim, K.S., et al., Large-scale pattern growth of graphene films for stretchable transparent electrodes. Nature, 2009. 457(7230): p. 706-710.

46. Song, L., et al., Large Scale Growth and Characterization of Atomic Hexagonal Boron Nitride Layers. Nano Letters, 2010. 10(8): p. 3209-3215.

47. Zhi, C., et al., Large-Scale Fabrication of Boron Nitride Nanosheets and Their Utilization in Polymeric Composites with Improved Thermal and Mechanical Properties. Advanced Materials, 2009. 21(28): p. 2889-2893.

48. Duan, Z.-Q., et al., A simple and green route to transparent boron nitride/PVA nanocomposites with significantly improved mechanical and thermal properties. Chinese Chemical Letters, 2013. 24(1): p. 17-19.

49. Madakbaş, S., E. Çakmakçı, and M.V. Kahraman, Preparation and thermal properties of polyacrylonitrile/hexagonal boron nitride composites. Thermochimica Acta, 2013. 552(0): p. 1-4.

50. Mirnezhad, M., R. Ansari, and H. Rouhi, Mechanical properties of multilayer boron nitride with different stacking orders. Superlattices and Microstructures, 2013. 53(0): p. 223-231.

51. Brayfindley, E., et al., Stone–Wales Rearrangements in Polycyclic Aromatic Hydrocarbons: A Computational Study. The Journal of Organic Chemistry, 2015. 80(8): p. 3825-3831.

52. Banhart, F., J. Kotakoski, and A.V. Krasheninnikov, Structural Defects in Graphene. ACS Nano, 2011. 5(1): p. 26-41.

53. Chen, W., et al., Electronic Structure and Reactivity of Boron Nitride Nanoribbons with Stone-Wales Defects. Journal of Chemical Theory and Computation, 2009. 5(11): p. 3088-3095.

54. Liu, Y., X. Zou, and B.I. Yakobson, Dislocations and Grain Boundaries in Two-Dimensional Boron Nitride. ACS Nano, 2012. 6(8): p. 7053-7058.

55. Gibb, A.L., et al., Atomic Resolution Imaging of Grain Boundary Defects in Monolayer Chemical Vapor Deposition-Grown Hexagonal Boron Nitride. Journal of the American Chemical Society, 2013. 135(18): p. 6758-6761.

56. Jin, C., et al., Fabrication of a Freestanding Boron Nitride Single Layer and Its Defect Assignments. Physical Review Letters, 2009. 102(19): p. 195505.

57. Zobelli, A., et al., Electron knock-on cross section of carbon and boron nitride nanotubes. Physical Review B, 2007. 75(24): p. 245402.

58. Alem, N., et al., Atomically thin hexagonal boron nitride probed by ultrahigh-resolution transmission electron microscopy. Physical Review B, 2009. 80(15): p. 155425.

59. Meyer, J.C., et al., Selective Sputtering and Atomic Resolution Imaging of Atomically Thin Boron Nitride Membranes. Nano Letters, 2009. 9(7): p. 2683-2689.

60. Wang, Z., Structure and electronic properties of boron nitride sheet with grain boundaries. Journal of Nanoparticle Research, 2012. 14(3): p. 1-7.

61. Choi, H., et al., Ambient Carbon Dioxide Capture by Boron-Rich Boron Nitride Nanotube. Journal of the American Chemical Society, 2011. 133(7): p. 2084-2087.

62. Sainsbury, T., et al., Oxygen Radical Functionalization of Boron Nitride Nanosheets. Journal of the American Chemical Society, 2012. 134(45): p. 18758-18771.

63. Pacile, D., et al., The two-dimensional phase of boron nitride: Few-atomic-layer sheets and suspended membranes. Applied Physics Letters, 2008. 92(13): p. 133107-133113.

64. Pacile, D., et al., The two-dimensional phase of boron nitride: Few-atomic-layer sheets and suspended membranes. Applied Physics Letters, 2008. 92(13): p. 133107.

65. Li, L.H., et al., Strong Oxidation Resistance of Atomically Thin Boron Nitride Nanosheets. ACS Nano, 2014. 8(2): p. 1457-1462.

66. Cunningham, G., et al., Solvent Exfoliation of Transition Metal Dichalcogenides: Dispersibility of Exfoliated Nanosheets Varies Only Weakly between Compounds. ACS Nano, 2012. 6(4): p. 3468-3480.

67. Exfoliation of Transition Metal Dichalcogenides: Dispersibility of Exfoliated Nanosheets Varies Only Weakly between Compounds. ACS Nano, 2012. 6(4): p. 3468-3480.

68. Li, L.H., et al., Large-scale mechanical peeling of boron nitride nanosheets by low-energy ball milling. Journal of Materials Chemistry, 2011. 21(32): p. 11862-11866.

69. Chen, X., J.F. Dobson, and C.L. Raston, Vortex fluidic exfoliation of graphite and boron nitride. Chemical Communications, 2012. 48(31): p. 3703-3705.

70. Yurdakul, H., et al., Nanoscopic characterization of two-dimensional (2D) boron nitride nanosheets (BNNSs) produced by microfluidization. Ceramics International, 2012. 38(3): p. 2187-2193.

71. Ghosh, J., et al., Microstructural characterization of amorphous and nanocrystalline boron nitride prepared by high-energy ball milling. Materials Research Bulletin, 2008. 43(4): p. 1023-1031.

72. Streletskii, A.N., et al., Mechanochemistry of hexagonal boron nitride: 1. Destruction and amorphization during mechanical treatment. Colloid Journal, 2010. 72(4): p. 544-552.

73. Streletskii, A.N., et al., Mechanochemistry of hexagonal boron nitride. 2. Reactivity upon interaction with water. Colloid Journal, 2010. 72(4): p. 553-558.

74. Streletskii, A.N., et al., Destruction, amorphization and reactivity of nano-BN under ball milling. Journal of Alloys and Compounds, 2009. 483(1–2): p. 313-316.

75. Lee, D., et al., Scalable Exfoliation Process for Highly Soluble Boron Nitride Nanoplatelets by Hydroxide-Assisted Ball Milling. Nano Letters, 2015. 15(2): p. 1238–1244.

76. Paton, K.R., et al., Scalable production of large quantities of defect-free few-layer graphene by shear exfoliation in liquids. Nat Mater, 2014. 13(6): p. 624-630.

77. Varrla, E., et al., Large-Scale Production of Size-Controlled MoS2 Nanosheets by Shear Exfoliation. Chemistry of Materials, 2015. 27(3): p. 1129–1139.

78. Lin, Y., T.V. Williams, and J.W. Connell, Soluble, Exfoliated Hexagonal Boron Nitride Nanosheets. The Journal of Physical Chemistry Letters, 2009. 1(1): p. 277-283.

79. Lotya, M., et al., Liquid Phase Production of Graphene by Exfoliation of Graphite in Surfactant/Water Solutions. Journal of the American Chemical Society, 2009. 131(10): p. 3611-3620.

80. Hernandez, Y., et al., Measurement of Multicomponent Solubility Parameters for Graphene Facilitates Solvent Discovery. Langmuir, 2010. 26(5): p. 3208-3213.

81. Du, W., X. Jiang, and L. Zhu, From graphite to graphene: direct liquid-phase exfoliation of graphite to produce single- and few-layered pristine graphene. Journal of Materials Chemistry A, 2013. 1(36): p. 10592-10606.

82. Jian, F.-S., et al., Liquid Phase Exfoliation of Two-Dimensional Materials by Directly. Nano Letters, 2015. 15(8): p. 5449-5454.

83. Zhou, K.-G., et al., A Mixed-Solvent Strategy for Efficient Exfoliation of Inorganic Graphene Analogues. Angewandte Chemie International Edition, 2011. 50(46): p. 10839-10842.

84. Wang, X., et al., Direct exfoliation of natural graphite into micrometre size few layers graphene sheets using ionic liquids. Chemical Communications, 2010. 46(25): p. 4487-4489.

85. Morishita, T., et al., A high-yield ionic liquid-promoted synthesis of boron nitride nanosheets by direct exfoliation. Chemical Communications, 2015. 51(60): p. 12068-12071.

86. Kim, J., et al., Direct exfoliation and dispersion of two-dimensional materials in pure water via temperature control. Nat Commun, DOI: 10.1038/ncomms9294.

87. Marsh, K.L., M. Souliman, and R.B. Kaner, Co-solvent exfoliation and suspension of hexagonal boron nitride. Chemical Communications, 2015. 51: p. 187-190.

88. Halim, U., et al., A rational design of cosolvent exfoliation of layered materials by directly probing liquid–solid interaction. Nat Commun, 2013. 4: p. 2213.

89. Wang, Y., Z. Shi, and J. Yin, Boron nitride nanosheets: large-scale exfoliation in methanesulfonic acid and their composites with polybenzimidazole. Journal of Materials Chemistry, 2011. 21(30): p. 11371-11377.

90. Berry, G.C., P.M. Cotts, and S.-G. Chu, Thermodynamic and rheological properties of rodlike polymers. British Polymer Journal, 1981. 13(2): p. 47-54.

91. Behabtu, N., et al., Spontaneous high-concentration dispersions and liquid crystals of graphene. Nat Nano, 2010. 5(6): p. 406-411.

92. Davis, V.A., et al., True solutions of single-walled carbon nanotubes for assembly into macroscopic materials. Nat Nano, 2009. 4(12): p. 830-834.

93. Ramesh, S., et al., Dissolution of Pristine Single Walled Carbon Nanotubes in Superacids by Direct Protonation. The Journal of Physical Chemistry B, 2004. 108(26): p. 8794-8798.

94. Niyogi, S., et al., Chemistry of Single-Walled Carbon Nanotubes. Accounts of Chemical Research, 2002. 35(12): p. 1105-1113.

95. Sun, Y.-P., et al., Functionalized Carbon Nanotubes: Properties and Applications. Accounts of Chemical Research, 2002. 35(12): p. 1096-1104.

96. Tasis, D., et al., Chemistry of Carbon Nanotubes. Chemical Reviews, 2006. 106(3): p. 1105-1136.

97. Banerjee, S., T. Hemraj-Benny, and S.S. Wong, Covalent Surface Chemistry of Single-Walled Carbon Nanotubes. Advanced Materials, 2005. 17(1): p. 17-29.

98. Xie, S.-Y., et al., Solubilization of boron nitride nanotubes. Chemical Communications, 2005(29): p. 3670-3672.

99. Pal, S., et al., Functionalization and solubilization of BN nanotubes by interaction with Lewis bases. Journal of Materials Chemistry, 2007. 17(5): p. 450-452.

100. Maguer, A., et al., A versatile strategy for the functionalization of boron nitride nanotubes. Journal of Materials Chemistry, 2009. 19(9): p. 1271-1275.

101. Wu, X., W. An, and X.C. Zeng, Chemical Functionalization of Boron−Nitride Nanotubes with NH3 and Amino Functional Groups. Journal of the American Chemical Society, 2006. 128(36): p. 12001-12006.

102. Ikuno, T., et al., Amine-functionalized boron nitride nanotubes. Solid State Communications, 2007. 142(11): p. 643-646.

103. Park, S. and R.S. Ruoff, Chemical methods for the production of graphenes. Nat Nano, 2009. 4(4): p. 217-224.

104. Zhu, Y., et al., Graphene and Graphene Oxide: Synthesis, Properties, and Applications. Advanced Materials, 2010. 22(35): p. 3906-3924.

105. Li, X., et al., Chemically Derived, Ultrasmooth Graphene Nanoribbon Semiconductors. Science, 2008. 319(5867): p. 1229-1232.

106. Han, W.-Q., et al., Structure of chemically derived mono- and few-atomic-layer boron nitride sheets. Applied Physics Letters, 2008. 93(22): p. 223103.

107. Tang, Q., Z. Zhou, and Z. Chen, Molecular Charge Transfer: A Simple and Effective Route To Engineer the Band Structures of BN Nanosheets and Nanoribbons. The Journal of Physical Chemistry C, 2011. 115(38): p. 18531-18537.

108. Zhao, J.-x., et al., Chemical functionalization of BN graphene with the metal-arene group: a theoretical study. Journal of Materials Chemistry, 2012. 22(18): p. 9343-9350.

109. Lai, L., et al., Magnetic Properties of Fully Bare and Half-Bare Boron Nitride Nanoribbons. The Journal of Physical Chemistry C, 2009. 113(6): p. 2273-2276.

110. Zhou, Y.G., et al., Electronic and magnetic properties of metal-doped BN sheet: A first-principles study. Physical Chemistry Chemical Physics, 2010. 12(27): p. 7588-7592.

111. Zhou, Y.G., et al., Electronic and magnetic properties of substituted BN sheets: A density functional theory study. Physical Chemistry Chemical Physics, 2011. 13(16): p. 7378-7383.

112. Zhou, Y.G., et al., First-principles study of the noble metal-doped BN layer. Journal of Applied Physics, 2011. 109(8): p. 084308.

113. Wang, Y., Y. Ding, and J. Ni, Electronic structures of Fe-terminated armchair boron nitride nanoribbons. Applied Physics Letters, 2011. 99(5): p. 053123.

114. Tao, N.J., J.A. DeRose, and S.M. Lindsay, Self-assembly of molecular superstructures studied by in situ scanning tunneling microscopy: DNA bases on gold (111). The Journal of Physical Chemistry, 1993. 97(4): p. 910-919.

115. Chen, Q., D.J. Frankel, and N.V. Richardson, Self-Assembly of Adenine on Cu(110) Surfaces. Langmuir, 2002. 18(8): p. 3219-3225.

116. Uchihashi, T., et al., Self-assembled monolayer of adenine base on graphite studied by noncontact atomic force microscopy. Physical Review B, 1999. 60(11): p. 8309-8313.

117. Adamcik, J., et al., Temperature-Controlled Assembly of High Ordered/Disordered Dodecylamine Layers on HOPG: Consequences for DNA Patterning. Langmuir, 2009. 25(5): p. 3159-3162.

118. Lin, Q., et al., Adsorption of DNA/RNA nucleobases on hexagonal boron nitride sheet: an ab initio study. Physical Chemistry Chemical Physics, 2011. 13(26): p. 12225-12230.

119. Yu, J., et al., Interfacial modification of boron nitride nanoplatelets for epoxy composites with improved thermal properties. Polymer, 2012. 53(2): p. 471-480.

120. Bhimanapati, G.R., D. Kozuch, and J.A. Robinson, Large-scale synthesis and functionalization of hexagonal boron nitride nanosheets. Nanoscale, 2014. 6(20): p. 11671-11675.

121. Chen, L., et al., Fabrication of two-dimensional nanosheets via water freezing expansion exfoliation. Nanotechnology, 2014. 25(49): p. 495302.

122. Luce, J.L. and A.M. Stacy, Crystallization of LnCu2O4 (Ln = La, Nd, Sm, Eu, Gd, Dy, Ho, Y, Er) from Hydroxide Melts: Synthesis and Structure. Chemistry of Materials, 1997. 9(7): p. 1508-1515.

123. Liu, H., C. Hu, and Z.L. Wang, Composite-Hydroxide-Mediated Approach for the Synthesis of Nanostructures of Complex Functional-Oxides. Nano Letters, 2006. 6(7): p. 1535-1540.

124. Xue, Y., et al., Excellent electrical conductivity of the exfoliated and fluorinated hexagonal boron nitride nanosheets. Nanoscale Research Letters, 2013. 8(1): p. 1-7.

125. Cui, Z., et al., Large Scale Thermal Exfoliation and Functionalization of Boron Nitride. Small, 2014. 10(12): p. 2352-2355.

126. Xiao, F., et al., Edge-Hydroxylated Boron Nitride Nanosheets as an Effective Additive to Improve the Thermal Response of Hydrogels. Advanced Materials, 2015. 27(44): p. 7196-7203.

127. Wang, X.-B., et al., Biomass-Directed Synthesis of 20 g High-Quality Boron Nitride Nanosheets for Thermoconductive Polymeric Composites. ACS Nano, 2014. 8: p. 9081-9088.

128. Jiao, L., et al., Narrow graphene nanoribbons from carbon nanotubes. Nature, 2009. 458(7240): p. 877-880.

129. Kosynkin, D.V., et al., Longitudinal unzipping of carbon nanotubes to form graphene nanoribbons. Nature, 2009. 458(7240): p. 872-876.

130. Jiao, L., et al., Facile synthesis of high-quality graphene nanoribbons. Nat Nano, 2010. 5(5): p. 321-325.

131. Zeng, H., et al., "White Graphenes": Boron Nitride Nanoribbons via Boron Nitride Nanotube Unwrapping. Nano Letters, 2010. 10(12): p. 5049-5055.

132. Liao, Y., et al., Chemical Sharpening, Shortening, and Unzipping of Boron Nitride Nanotubes. Advanced Functional Materials, 2014. 24(28): p. 4497-4506.

133. Li, L., et al., High-Quality Boron Nitride Nanoribbons: Unzipping during Nanotube Synthesis. Angewandte Chemie, 2013. 125(15): p. 4306-4310.

134. Kuzuba, T., et al., Raman-scattering study of high-pressure effects on the anisotropy of force constants of hexagonal boron nitride. Physical Review B, 1978. 18(8): p. 4440-4443.

135. Nag, A., et al., Graphene Analogues of BN: Novel Synthesis and Properties. ACS Nano, 2010. 4(3): p. 1539-1544.

136. Gao, R., et al., High-Yield Synthesis of Boron Nitride Nanosheets with Strong Ultraviolet Cathodoluminescence Emission. The Journal of Physical Chemistry C, 2009. 113(34): p. 15160-15165.

137. Lim, H.S., et al., Anisotropically Alignable Magnetic Boron Nitride Platelets Decorated with Iron Oxide Nanoparticles. Chemistry of Materials, 2013. 25(16): p. 3315-3319.

138. Gao, M., A. Lyalin, and T. Taketsugu, Catalytic Activity of Au and Au2 on the h-BN Surface: Adsorption and Activation of O2. The Journal of Physical Chemistry C, 2012. 116(16): p. 9054-9062.

139. Lian, G., et al., Facile synthesis of 3D boron nitride nanoflowers composed of vertically aligned nanoflakes and fabrication of graphene-like BN by exfoliation. Journal of Materials Chemistry, 2011. 21(25): p. 9201-9207.

140. Zhang, S., et al., Ultrathin BN nanosheets with zigzag edge: one-step chemical synthesis, applications in wastewater treatment and preparation of highly thermal-conductive BN-polymer composites. Journal of Materials Chemistry A, 2013. 1(16): p. 5105-5112.

141. Wang, X., et al., Large-surface-area BN nanosheets and their utilization in polymeric composites with improved thermal and dielectric properties. Nanoscale Research Letters, 2012. 7(1): p. 662.

142. Yang, P.C., et al., The formation of epitaxial hexagonal boron nitride on nickel substrates. Journal of Electronic Materials, 2005. 34(12): p. 1558-1564.

143. Suzuki, S., R.M. Pallares, and H. Hibino, Growth of atomically thin hexagonal boron nitride films by diffusion through a metal film and precipitation. Journal of Physics D: Applied Physics, 2012. 45(38): p. 385304.

144. Rand, M.J. and J.F. Roberts, Preparation and Properties of Thin Film Boron Nitride. Journal of The Electrochemical Society, 1968. 115(4): p. 423-429.

145. Pakdel, A., C. Zhi, Y. Bando, and D. Golberg, Low-dimensional boron nitride nanomaterials. Materials Today, 2012. 15(6): p. 256-265.

146. Lin, Y. and J.W. Connell, Advances in 2D boron nitride nanostructures: nanosheets, nanoribbons, nanomeshes, and hybrids with graphene. Nanoscale, 2012. 4(22): p. 6908-6939.

147. Xiang-Fen Jiang, Q.W., Xue-Bin Wang, Xia Li, Jun Zhang, Dmitri Golberg, Yoshio Bando, Recent Progress on Fabrications and Applications of Boron Nitride Nanomaterials: A Review. J. Mater. Sci. Technol., 2015. 31(6): p. 589-598.

148. Auwärter, W., et al., Synthesis of One Monolayer of Hexagonal Boron Nitride on Ni(111) from B-Trichloroborazine (ClBNH)3. Chemistry of Materials, 2003. 16(2): p. 343-345.

149. Ye, Y., U. Graupner, and R. Krüger, Hexagonal Boron Nitride from a Borazine Precursor for Coating of SiBNC Fibers using a Continuous Atmospheric Pressure CVD Process. Chemical Vapor Deposition, 2011. 17(7-9): p. 221-227.

150. Shi, Y., et al., Synthesis of Few-Layer Hexagonal Boron Nitride Thin Film by Chemical Vapor Deposition. Nano Letters, 2010. 10(10): p. 4134-4139.

151. Ismach, A., et al., Toward the Controlled Synthesis of Hexagonal Boron Nitride Films. ACS Nano, 2012. 6(7): p. 6378-6385.

152. Vilcarromero, J., M.N.P. Carreño, and I. Pereyra, Mechanical properties of boron nitride thin films obtained by RF-PECVD at low temperatures. Thin Solid Films, 2000. 373(1–2): p. 273-276.

153. Chatterjee, S., et al., Chemical Vapor Deposition of Boron Nitride Nanosheets on Metallic Substrates via Decaborane/Ammonia Reactions. Chemistry of Materials, 2011. 23(20): p. 4414-4416.

154. Kim, K.K., et al., Synthesis of Monolayer Hexagonal Boron Nitride on Cu Foil Using Chemical Vapor Deposition. Nano Letters, 2011. 12(1): p. 161-166.

155. Lee, Y.-H., et al., Growth selectivity of hexagonal-boron nitride layers on Ni with various crystal orientations. RSC Advances, 2012. 2(1): p. 111-115.

156. Gao, Y., et al., Repeated and Controlled Growth of Monolayer, Bilayer and Few-Layer Hexagonal Boron Nitride on Pt Foils. ACS Nano, 2013. 7(6): p. 5199-5206.

157. Park, J.-H., et al., Large-Area Monolayer Hexagonal Boron Nitride on Pt Foil. ACS Nano, 2014. 8(8): p. 8520-8528.

158. Khan, M.H., et al., ERRATUM: Synthesis of Large and Few Atomic Layers of Hexagonal Boron Nitride on Melted Copper. Scientific Reports, 2015. 5: p. 9547.

159. Geim, A.K. and K.S. Novoselov, The rise of graphene. Nat Mater, 2007. 6(3): p. 183-191.

160. Dean, C.R., et al., Boron nitride substrates for high-quality graphene electronics. Nat Nano, 2010. 5(10): p. 722-726.

161. Britnell, L., et al., Field-Effect Tunneling Transistor Based on Vertical Graphene Heterostructures. Science, 2012. 335(6071): p. 947-950.

162. Britnell, L., et al., Electron Tunneling through Ultrathin Boron Nitride Crystalline Barriers. Nano Letters, 2012. 12(3): p. 1707-1710.

163. Sinitskii, A., et al., High-Yield Synthesis of Boron Nitride Nanoribbons via Longitudinal Splitting of Boron Nitride Nanotubes by Potassium Vapor. ACS Nano, 2014. 8(10): p. 9867-9873.

164. Kim, D., et al., Sonication-assisted alcoholysis of boron nitride nanotubes for their sidewalls chemical peeling. Chemical Communications, 2015. 51(33): p. 7104-7107.

165. Qi, J., et al., Strain-Engineering of Band Gaps in Piezoelectric Boron Nitride Nanoribbons. Nano Letters, 2012. 12(3): p. 1224-1228.

166. Li, J., G. Gui, and J. Zhong, Tunable bandgap structures of two-dimensional boron nitride. Journal of Applied Physics, 2008. 104(9): p. 094311.

167. Hu, M.L., et al., Electronic structures and optical properties of hexagonal boron nitride under hydrostatic pressures. Journal of Applied Physics, 2011. 109(7): p. 073708.

168. Barone, V. and J.E. Peralta, Magnetic Boron Nitride Nanoribbons with Tunable Electronic Properties. Nano Letters, 2008. 8(8): p. 2210-2214.

169. Ding, Y., Y. Wang, and J. Ni, The stabilities of boron nitride nanoribbons with different hydrogen-terminated edges. Applied Physics Letters, 2009. 94(23): p. 233107.

170. Chen, W., et al., Hydrogenation: A Simple Approach To Realize Semiconductor−Half-Metal−Metal Transition in Boron Nitride Nanoribbons. Journal of the American Chemical Society, 2010. 132(5): p. 1699-1705.

171. Zhang, H.X. and P.X. Feng, Controlling Bandgap of Rippled Hexagonal Boron Nitride Membranes via Plasma Treatment. ACS Applied Materials & Interfaces, 2012. 4(1): p. 30-33.

172. Tang, C., et al., Fluorination and Electrical Conductivity of BN Nanotubes. Journal of the American Chemical Society, 2005. 127(18): p. 6552-6553.

173. Sevik, C., et al., Characterization of thermal transport in low-dimensional boron nitride nanostructures. Physical Review B, 2011. 84(8): p. 085409.

174. Lindsay, L. and D.A. Broido, Enhanced thermal conductivity and isotope effect in single-layer hexagonal boron nitride. Physical Review B, 2011. 84(15): p. 155421.

175. Lindsay, L. and D.A. Broido, Theory of thermal transport in multilayer hexagonal boron nitride and nanotubes. Physical Review B, 2012. 85(3): p. 035436.

176. Ouyang, T., et al., Thermal transport in hexagonal boron nitride nanoribbons. Nanotechnology, 2010. 21(24): p. 245701.

177. Zhi, C., et al., Highly Thermo-conductive Fluid with Boron Nitride Nanofillers. ACS Nano, 2011. 5(8): p. 6571-6577.

178. Taha-Tijerina, J., et al., Electrically Insulating Thermal Nano-Oils Using 2D Fillers. ACS Nano, 2012. 6(2): p. 1214-1220.

179. Liu, F., P. Ming, and J. Li, \textit{Ab initio} calculation of ideal strength and phonon instability of graphene under tension. Physical Review B, 2007. 76(6): p. 064120.

180. Konstantinova, E., S.O. Dantas, and P.M.V.B. Barone, Electronic and elastic properties of two-dimensional carbon planes. Physical Review B, 2006. 74(3): p. 035417.

181. Zakharchenko, K.V., M.I. Katsnelson, and A. Fasolino, Finite Temperature Lattice Properties of Graphene beyond the Quasiharmonic Approximation. Physical Review Letters, 2009. 102(4): p. 046808.

182. Lee, C., et al., Measurement of the Elastic Properties and Intrinsic Strength of Monolayer Graphene. Science, 2008. 321(5887): p. 385-388.

183. Şahin, H., et al., Monolayer honeycomb structures of group-IV elements and III-V binary compounds: First-principles calculations. Physical Review B, 2009. 80(15): p. 155453.

184. Wang, X., et al., High-yield boron nitride nanosheets from 'chemical blowing': towards practical applications in polymer composites. Journal of Physics: Condensed Matter, 2012. 24(31): p. 314205.

185. Yu, J., et al., Vertically Aligned Boron Nitride Nanosheets: Chemical Vapor Synthesis, Ultraviolet Light Emission, and Superhydrophobicity. ACS Nano, 2010. 4(1): p. 414-422.

186. Pakdel, A., et al., Boron Nitride Nanosheet Coatings with Controllable Water Repellency. ACS Nano, 2011. 5(8): p. 6507-6515.

187. Pakdel, A., Y. Bando, and D. Golberg, Plasma-Assisted Interface Engineering of Boron Nitride Nanostructure Films. ACS Nano, 2014. 8(10): p. 10631-10639.

188. Pakdel, A., Y. Bando, and D. Golberg, Morphology-Driven Nonwettability of Nanostructured BN Surfaces. Langmuir, 2013. 29(24): p. 7529-7533.

189. Pakdel, A., et al., Nonwetting "white graphene" films. Acta Materialia, 2013. 61(4): p. 1266-1273.

190. Li, L.H. and Y. Chen, Superhydrophobic Properties of Nonaligned Boron Nitride Nanotube Films. Langmuir, 2010. 26(7): p. 5135-5140.

191. Lee, C.H., J. Drelich, and Y.K. Yap, Superhydrophobicity of Boron Nitride Nanotubes Grown on Silicon Substrates. Langmuir, 2009. 25(9): p. 4853-4860.

192. Li, G.-X., et al., Preparation of transparent BN films with superhydrophobic surface. Applied Surface Science, 2008. 254(17): p. 5299-5303.

193. Duerloo, K.-A.N. and E.J. Reed, Flexural Electromechanical Coupling: A Nanoscale Emergent Property of Boron Nitride Bilayers. Nano Letters, 2013. 13(4): p. 1681-1686.

194. Cumings, J. and A. Zettl, Field emission and current-voltage properties of boron nitride nanotubes. Solid State Communications, 2004. 129(10): p. 661-664.

195. Chen, Z.-G. and J. Zou, Field emitters: ultrathin BN nanosheets protruded from BN fibers. Journal of Materials Chemistry, 2011. 21(4): p. 1191-1195.

196. Zhu, et al., Field Nanoemitters: Ultrathin BN Nanosheets Protruding from Si3N4 Nanowires. Nano Letters, 2006. 6(12): p. 2982-2986.

197. Wang, L., et al., Convenient synthesis and applications of gram scale boron nitride nanosheets. Catalysis Science & Technology, 2011. 1(7): p. 1119-1123.

198. Lin, Y., et al., Aqueously Dispersed Silver Nanoparticle-Decorated Boron Nitride Nanosheets for Reusable, Thermal Oxidation-Resistant Surface Enhanced Raman Spectroscopy (SERS) Devices. ACS Applied Materials & Interfaces, 2012. 4(2): p. 1110-1117.

199. Weng, Q., et al., Boron Nitride Porous Microbelts for Hydrogen Storage. ACS Nano, 2013. 7(2): p. 1558-1565.

200. Lee, C., et al., Frictional Characteristics of Atomically Thin Sheets. Science, 2010. 328(5974): p. 76-80.

201. Cho, D.-H., et al., Evaluation of hexagonal boron nitride nano-sheets as a lubricant additive in water. Wear, 2013. 302(1–2): p. 981-986.

Chapter 3 Experimental

3.1 Chemicals

Detailed information on the chemicals used in this thesis is summarized in Table 3.1.

Table 3.1. List of chemicals used.

Chemicals name	Formula	Purity (%)	Supplier
Hexagonal boron nitride	*h*-BN	99.95+	Alfa Aesar
Ethanol	C_2H_5OH	99.95+	Sigma Aldrich
Isopropanol	$(CH_3)_2CHOH$	99.95+	Sigma Aldrich
N-isopropylacrylamide	$(C_6H_{11}NO)_n$	97+	Sigma Aldrich
α-ketoglutaric acid	$C_5H_6O_5$	99+	Sigma Aldrich
N-*N*′-methylenebisacrylamide	$C_7H_{10}N_2O_2$	99+	Sigma Aldrich
Milli-Q water	H_2O	5 ppb (TOC)	Millipore
Argon gas	Ar	n/a	BOC gas
Magnesium diboride	MgB_2	99+	Alfa Aesar
Ammonium chloride	NH_4Cl	99.5+	Sigma Aldrich
Hydrochloric acid	HCl	32	Ajax FineChem
Ammonia gas	NH_3	n/a	BOC gas
Nitric acid	HNO_3	69	Sigma Aldrich
Melamine	$C_3H_6N_6$	99+	Sigma Aldrich
Ethylene glycol	$C_2H_6O_2$	99.8+	Sigma Aldrich
Boric acid	H_3BO_3		Sigma Aldrich
Polyethylene glycol	$C_{2n}H_{4n+2}O_{n+1}$	n/a	Sigma Aldrich
Fumed silica	SiO_2	n/a	
Nitrogen gas	N_2	n/a	BOC gas

3.2 Characterizations and Instruments

3.2.1 X-ray diffraction

X-ray diffraction (XRD) is an efficient analytic technique that can yield information on unit cell dimensions. X-ray diffraction is obtained from the constructive interference of monochromatic X-rays by a crystalline sample. Generally, a cathode ray tube is used to generate X-rays, which are filtered to produce monochromatic radiation, collimated to concentrate them, and directed toward the sample. Constructive interference and a diffracted ray are produced by the interaction of the incident rays and the sample when the conditions satisfy Bragg's Law (3.1).

$$n\lambda = 2dsin\theta \quad (3.1)$$

Where *d* is the distance between diffracting planes, λ is the wavelength of the incident X-ray beam, *n* is any integer, and θ is the angle of incidence experienced by the X-ray beam reflection from the faces of the crystal. The crystal size of materials can also be estimated acoording to the Sherrer formula (3.2).

$$D = \frac{K\lambda}{\beta cos\theta} \quad (3.2)$$

Where *K* is the shape factor of the average crystallite, λ is the X-ray wavelength, β is the half-peak width, and 2θ is the peak position (°).

The analysed material is finely ground. The XRD patterns were obtained on a GBC MMA ($Cu_{K\alpha}$, λ = 0.15406 nm) at UOW with step size 0.02° and scan rate 3°/min.

3.2.2 Scanning electron microscopy

Scanning electron microscopy (SEM) is a type of electron microscope routinely used to generate high-resolution images of objects by scanning them with a focused beam of high-energy electrons. The electron beam is generally scanned in a raster scan pattern, and the position of the beam is combined with the detected signal to generate an image. SEM can achieve resolution better than 1 nanometer. Specimens can be observed in high vacuum, in low vacuum, in wet conditions (in environmental SEM), and at a wide range of cryogenic or elevated temperatures.

In my case, *h*-BN is an insulator, so an electrically conductive coating (Au in this case) has been used to produce better images. Otherwise, the randomly scattered electrons would degrade the image quality. The SEM used for this PhD research was a JSM 7500F.

3.2.3 Transmission electron microscopy

Transmission electron microscopy (TEM) is a microscopy technique in which a beam of electrons is transmitted through an ultra-thin specimen, interacting with the specimen as it passes through. An image is formed from the interaction of the electrons transmitted through the specimen, and is magnified and focused onto an imaging device for a permanent record. The image-recording device usually consists of a fluorescent screen on a layer of photographic film and a digital camera. Additionally, a vacuum system, which consists of pumps and their associated gauges, valves, and power supplies, are required. The source of electrons is a heated V-shaped tungsten filament or, in high-performance instruments, a sharply pointed rod of a material such as lanthanum hexaboride. The TEM microscopes used in this thesis were a JEOL 2011 and a JSM 7500F at 80 kV.

3.2.4 Electron energy loss spectroscopy

Electron energy loss spectroscopy (EELS) is used for composition analysis and for the determination of chemical states of elements, based on the way that electrons interact with the sample. For instance, different elements in a sample result in changes in electron energies after their interaction with the sample, which normally results in chromatic aberration. This effect enables an image that provides information on elemental composition, based on the atomic transitions during electron-electron interaction. EELS data in this thesis were obtained on a JSM 7500F.

3.2.5 Energy dispersive X-ray spectroscopy

Energy dispersive x-ray spectroscopy (EDS, EDX, or XEDS) is an analytical technique used for elemental analysis. It is based on the interaction of some source of X-ray excitation and a sample. Its characterization capabilities are largely associated with the fundamental principle that each element has a unique atomic structure allowing a unique set of peaks on its X-ray emission spectrum. Qualitative and quantitative information on the chemical composition and elements can be obtained. Electron beam excitation is used in electron microscopes, so EDS is attached to SEM and TEM. EDS data in this thesis was obtained on a JSM 7500F.

3.2.6 Fourier transform infrared spectroscopy

Fourier transform infrared spectroscopy (FTIR) is a technique that is used to obtain an infrared spectrum of absorption, emission, and photoconductivity of a solid, liquid, or gas. An FTIR spectrometer simultaneously collects high spectral resolution data over a wide spectral

range. FTIR spectra in this thesis were collected using the KBr pellet method on a Shimadzu FTIR Prestige-21.

3.2.7 Raman spectroscopy

Raman spectroscopy is a technique that is used to observe vibrational, rotational, and other low-frequency modes in a system. It is commonly used in chemistry to provide a fingerprint by which molecules can be identified. Raman spectroscopy relies on inelastic scattering or Raman scattering of monochromatic light, usually from a laser in the visible, near infrared, or near ultraviolet range. The laser light interacts with molecular vibrations, phonons, or other excitations in the system, leading to the energy of the laser photons being shifted up or down. The shifting energy gives information on the vibrational modes in the systems. Raman scattering spectra (Horiba JobinYvon/LabRAM HR8000) were obtained at room temperature, and the wavelength of the laser source was 632.8 nm.

3.2.8 Atomic force microscope

An atomic force microscope (AFM) is able to measure the roughness of a sample surface at high resolution. Generally, the operation modes of AFM are classified into image formation and the others. The image formation is a plotting method in the form of a colour mapping through scanning in the x-y position of the tip and recording some particular z-coordinate corresponding to each x-y coordinate. The thickness of samples in this thesis was measured by an atomic force microscope (Asylum AFM).

3.2.9 X-ray photoelectron spectroscopy

X-ray photoelectron spectroscopy (XPS) is a surface-sensitive quantitative spectroscopic technique that measures the elemental composition of a sample surface. XPS spectra are obtained by irradiating a material with X-rays while simultaneously measuring the kinetic energy and number of electrons that escape from the top 0 to 10 nm of the material being analysed. It is a surface chemical analysis technique that is able to analyse the surface chemistry of a material in its as-received state, or after treatment. The elemental composition of samples was characterized using an X-ray photoelectron spectrometer (PHOIBOS 100 hemispherical analyser SPECSGmbH) at energy of 486.6 eV.

3.3.10 Brunauer-Emmett-Teller surface area analysis

Brunauer-Emmett-Teller surface area analysis (BET) is a technique used to measure the specific surface area. BET analysis relies on the BET theory, which explains physical adsorption of gas molecules on a solid surface and serves as the basis for an important analysis technique for the measurement of the specific surface area of a material. The BET theory refers to multilayer adsorption, and BET surface area analysis usually adopts non-corrosive gases (such as nitrogen, argon, carbon dioxide, etc.) as adsorbates to determine the surface area data.

Relying on Barrett-Joyner-Halenda (BJH) desorption model, the pore size distribution of a sample can be calculated from the isotherms obtained in the BET analysis. The measurements in this thesis were conducted on a Quantachrome Autosorb MP instrument, with high purity nitrogen (99.999 %) and carbon dioxide (99.995 %) gasses. Surface areas were determined using Brunauer-Emmett-Teller (BET) calculations.

Chapter 4 Hydroxylated Boron Nitride Nanosheets for thermal management

4.1 Introduction

Isostructural to graphene, single-layer hexagonal boron nitride (*h*-BN) has alternating boron and nitrogen atoms replacing carbon atoms in a sp^2-bonded two-dimensional layer.[1] Due to its atomically flat and electrically insulating surface, the *h*-BN nanosheet (*h*-BNNS) has been considered as an ideal substrate for graphene-based electronics.[2] In contrast to the covalent C-C bond of graphene, the covalent nature of the B-N bond makes *h*-BNNS highly resistant to oxidation (stable up to 840 ºC in air)[3] and to corrosion[4]. Additionally, *h*-BNNS shows excellent mechanical properties and thus has been extensively applied as a lubricant in harsh environments.[5] More interestingly, *h*-BNNS has excellent thermal conductivity, which makes it an efficient filler to improve the thermal performance of liquids[6, 7] and solid polymeric composites.[8] For all these applications, a facile method to synthesize high-quality *h*-BNNS is a prerequisite to take full advantage of its intrinsic properties.

The methods for the preparation of *h*-BNNS have been quite limited and inefficient, compared with the facile methods for the large scale production of graphene. So far, the most common way of producing *h*-BNNS is via sonication-assisted exfoliation of bulk *h*-BN powder. To overcome the van der Waals forces between the layers, the liquid media/solvents for effective exfoliation should have similar surface energy to that of *h*-BN.[9] Mono- and few-layered *h*-BNNS have been prepared by sonicating *h*-BN in media such as water, isopropanol, and *N*-methyl-2-pyrrolidone.[10-12] A complete removal of some of the solvents, however, can be hampered by their high boiling points. Compared with the numerous reports on functionalized graphene, only a few papers have been published on functionalizing *h*-BN, which is likely due to its exceptional chemical stability. Simulations have indicated that effective functionalization of *h*-BNNS can change its band gap and

consequently lead to applications in various fields.[13] Experimentally, hydroxyl functionalized *h*-BNNS (OH-BNNS) has been synthesized via various methods, including sonicating bulk *h*-BN powder in water,[10] heating bulk *h*-BN powder in air,[14] treating *h*-BN powder in hot $H_2SO_4/KMnO_4$ aqueous solution,[15] chemical reactions between *g*-C_3N_4 and $B(OH)_3$,[16] and oxygen radical functionalization followed by hydrolytic defunctionalization.[12] The presence of OH groups could alter the surface energy and thus ameliorate the solubility of *h*-BNNS in a variety of solvents. Being very common in Nature, hydroxyl (OH) groups can interact with various forms of inorganic and organic matter, and therefore, the intrinsic properties of *h*-BNNS can be better exploited by grafting OH groups. For example, OH-BNNS has been very effective for polymer reinforcement[12] and drug delivery.[16]

In this thesis, commercial *h*-BN was directly exfoliated by a steam treatment and simultaneously functionalized to yield OH-BNNS (Figure 4.1). This procedure is simple, low-cost, free of harsh chemicals, and can be readily scaled up. Furthermore, it's been demonstrated that the functionalization occurs predominantly along the platelet edge. The resultant excellent dispersion and stability of OH-BNNS in aqueous solution and organic solutions make it an effective additive to *N*-isopropylacrylamide based hydrogels, leading to much enhanced thermal conductivity without compromising the mechanical properties. The resulting hydrogels demonstrate faster dimensional change and dye desorption upon heating.

4.2 Experimental section

Preparation of OH-BNNS

The exfoliation and in-situ functionalization of boron nitride was carried out in a tube furnace with a fused quartz tube. Commercial boron nitride powder (99.95%, Alfa) in an alumina

crucible was placed at the center of the furnace, with another crucible full of water placed a few inches apart, upstream of the carrier gas inlet. After the quartz tube was purged with Ar a few times, the furnace was gradually heated up and kept for 2 h at the set temperature under Ar flow of 100 sccm. The resultant products were dispersed in either organic solvents, such as ethanol and isopropanol (IPA), or deionized water, where OH-BNNS forms a milky suspension. To quantify the OH-BNNS suspended in the liquids, the product obtained at 850 ºC was dispersed with an initial concentration of 1 mg/ml and sonicated for 5 min. After centrifuging at 1200 rpm for 30 min to remove the large particles, the ¾ top of the suspension was carefully transferred into another vial and then dried, with the resultant solid powder weighed. For the products obtained at higher temperatures (≥ 950 °C), before being treated by the same procedure, they were washed by DI water to remove H_3BO_3.

Characterization of OH-BNNS

X-ray powder diffraction (XRD) patterns were obtained on a GBC MMA (Cu Kα, λ = 0.15406 nm). Fourier transform infrared (FTIR) spectra were collected using a Shimadzu FTIR Prestige-21. Raman spectra were obtained at room temperature using a Horiba JobinYvon/LabRAM HR8000 with a laser source at 632.8 nm. The topographic heights of OH-BNNS were measured by an atomic force microscope (AFM, Asylum Research, MFP-3D). The morphology and lateral size of OH-BNNS were examined by a field emission scanning electron microscope (FESEM, JSM 7500F, JEOL). Bright field and high resolution transmission electron microscope (TEM, JEM 2010, JEOL) images were collected at 80 kV accelerating voltage. Electron energy loss spectroscopy (EELS) mapping was performed to determine the distribution of OH groups.

Preparation of PNIPAM/OH-BNNS

Temperature sensitive hydrogel composites were synthesized from *N*-isopropylacrylamide (NIPAM, Sigma-Aldrich). α-ketoglutaric acid and *N*-*N*′ -methylenebisacrylamide (BIS) were used as, respectively, the ultraviolet (UV)-initiator and the crosslinking agent (Sigma-Aldrich). To create NIPAM polymer (PNIPAM)/OH-BNNS hydrogels, an ethanol-based OH-BNNS dispersion (0.06 mg/ml) was used as the base medium to dissolve NIPAM (20 wt %), along with the UV-initiator (2.5 mol %) and BIS (2.5 mol %). The molar concentrations of UV-initiator and crosslinking agent were based on NIPAM monomer. To vary the concentration of OH-BNNS in the final composite, ethanol was used to dilute the main OH-BNNS stock solution. Where PNIPAM hydrogel was needed as a control, only ethanol was used to dissolve the above components. Polymerization was performed in a UV chamber (300 nm) for 6 h. As-prepared hydrogels were removed from the polymerization mold and placed in Milli-Q water to exchange ethanol with water, while water was replaced on a daily basis for 3 days.

For Raman mapping (collected at 1362 cm^{-1}), the hydrogel sample was freeze-dried and then crashed in an agate mortar with the pestle. Mechanical testing was performed on fully swollen hydrogels using a Shimadzu mechanical tester (EZ-L). Tensile tests were carried out on hydrogel ribbons (1 mm×5 mm ×20 mm), while compression tests were performed on cylindrical hydrogels (15 × ∅15 mm^3). In both cases the cross-head speed was fixed at 5 mm/min. Differential scanning calorimetry was carried out on the hydrogels to determine their heat capacity using a TA Q-100 DSC instrument. Through-thickness thermal diffusivity of the hydrogels was measured on a Linseis LFA1000 Laser Flash Analyser at room temperature. The hydrogels were taken out of the warm water (50 ºC) to observe the change in transparency using a digital camera (Optek, Australia) calibrated against a gray scale background; they were placed in the same petri dish with warm water (50 ºC) to observe the

change in dimension; a similar set up was used to monitor the dye release, but with warm water at 40 ºC.

4.3 Results and discussion

Stable dispersions of ~ 0.3 mg/mL OH-BNNS in water and ~ 0.06 mg/mL OH-BNNS in ethanol (Figure 4.2a and b) appear translucent, and the concentrations are much higher than those for *h*-BNNS with negligible amounts of hydroxyl groups[17] and are consistent with previous reports.[7, 10, 14] The SEM studies show that the as-received *h*-BN (Figure 4.3) powders consist of thick platelets with smooth surfaces and edges, and the lateral size is from 1 to 7 microns. The OH-BNNS (Figure 4.3a-c) obtained at 850 ºC appears to be transparent due to the much reduced thickness, but with a slightly reduced lateral size ranging from submicron to several microns. This is much larger than the exfoliated OH-BNNS in previous reports.[10, 14, 17] When the temperature was increased to 1000 ºC, smaller sheets with more noticeable voids in the plane were obtained (Figure 4.3d-e). This morphology is very similar to that in previous reports,[14, 17] where prolonged sonication was applied to exfoliate the *h*-BN. The formation of small sheets with many defects will have a negative impact on the heat transfer along the plane. Therefore, a low temperature, 850 ºC in this case, has been selected to produce large OH-BNNS with fewer defects.

Figure 4.4a shows TEM images of OH-BNNS with morphology similar to the parent *h*-BN powder. The Moiré pattern is associated with the restacked few-layered OH-BNNS with different orientations, which has been observed in the case of graphene.[18] Few-layered OH-BNNS can be clearly seen in high magnification transmission electron microscope (TEM) images (Figure 4.4b and Figure 4.3f). The electron diffraction pattern (inset of Figure 4.4b) reveals the typical six-fold symmetry of *h*-BN, indicative of the structural integrity after the

exfoliation. Atomic force microscope (AFM) topographic images of OH-BNNS were acquired via tapping mode. Isolated OH-BNNS with a thickness of ~1 nm and lateral size of approximately 2 μm was observed (Figure 4.5). A terraced morphology showing a mono-layered OH-BNNS joined to a tri-layered OH-BNNS can be seen, taking into account the solvents trapped between the OH-BNNS and the silicon substrate.[19] The result is in good agreement with that in Figure 4.4b, further supporting the effective exfoliation of *h*-BN during the treatment.

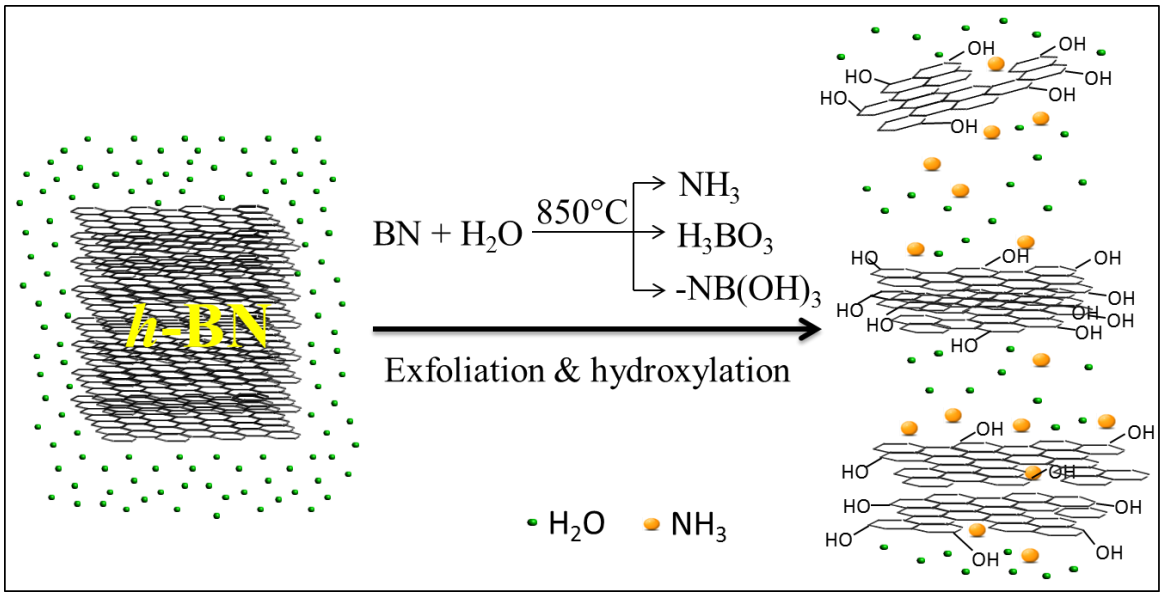

Figure 4.1. Schematic illustration of hydrolysis-assisted exfoliation and hydroxylation of *h*-BN powder in hot steam, where H_2O reacts with *h*-BN, forming NH_3 and -$NB(OH)_x$, and the highly energetic H_2O and NH_3 assist the exfoliation through diffusion between BN layers.

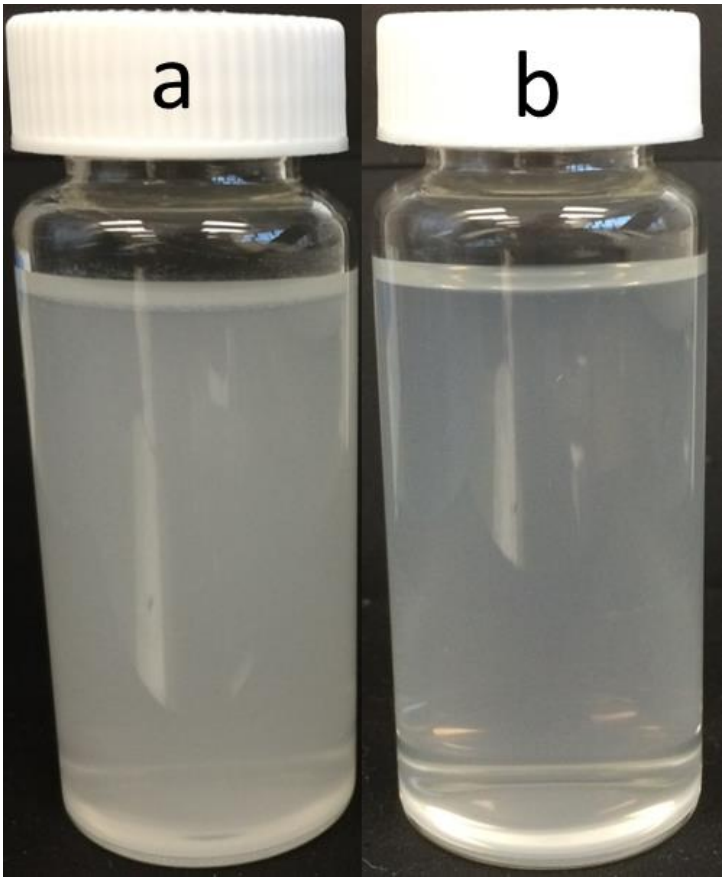

Figure 4.2. a) 0.3 mg/mL OH-BNNS in water; b) 0.06 mg/mL OH-BNNS in ethanol. OH-BNNS/water, which contains more OH-BNNS, appears less transparent than the OH-BNNS/ethanol.

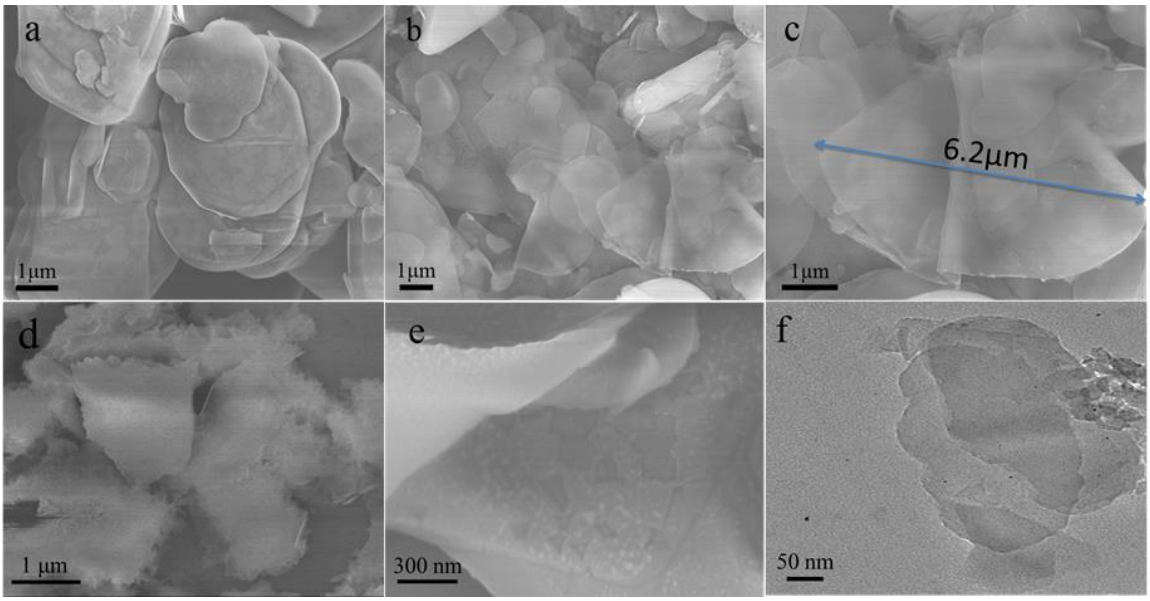

Figure 4.3. SEM images of a) commercial *h*-BN, b) OH-BNNS exfoliated at 850 ºC, c)

zoomed-in image of (b), d) exfoliated OH-BNNS at 1000 ºC; e) voids formed on OH-BNNS at 1000 ºC; f) high resolution TEM image of OH-BNNS exfoliated at 1000 °C. (When the synthesis temperature was increased to 1000 ºC, the morphology of the resultant powder shows more rough edges and small voids on the plane, in contrast to the morphology of pristine *h*-BN and *h*-BNNS obtained at 850 ºC.)

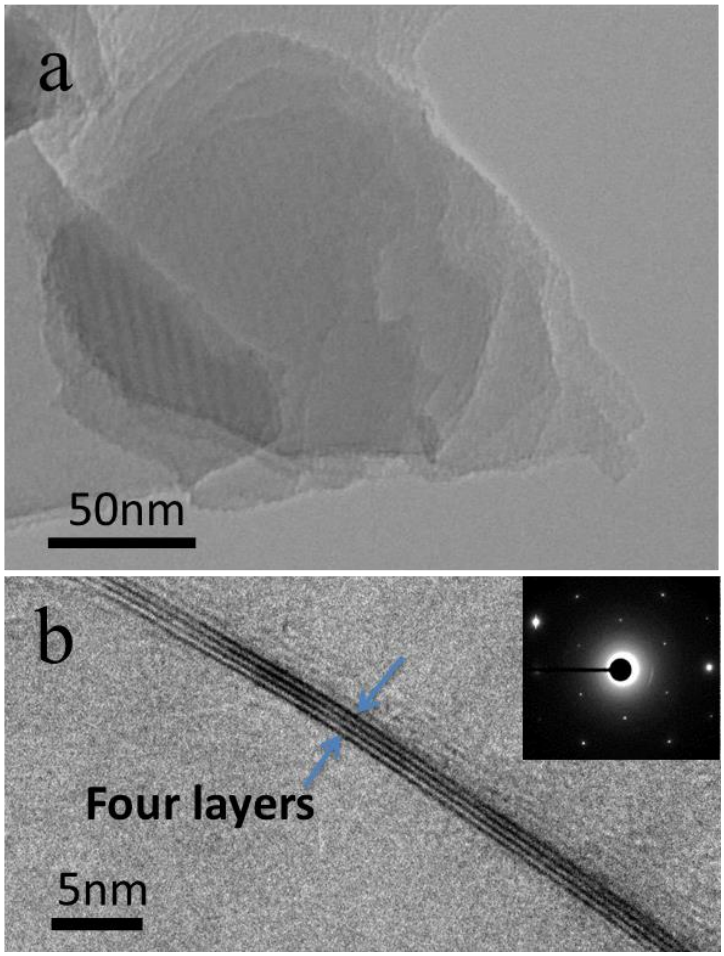

Figure 4.4. a) TEM image of a Moiré pattern due to the stacking of few-layered OH-BNNS; b) TEM image of four-layered OH-BNNS (inset showing the corresponding electron diffraction pattern).

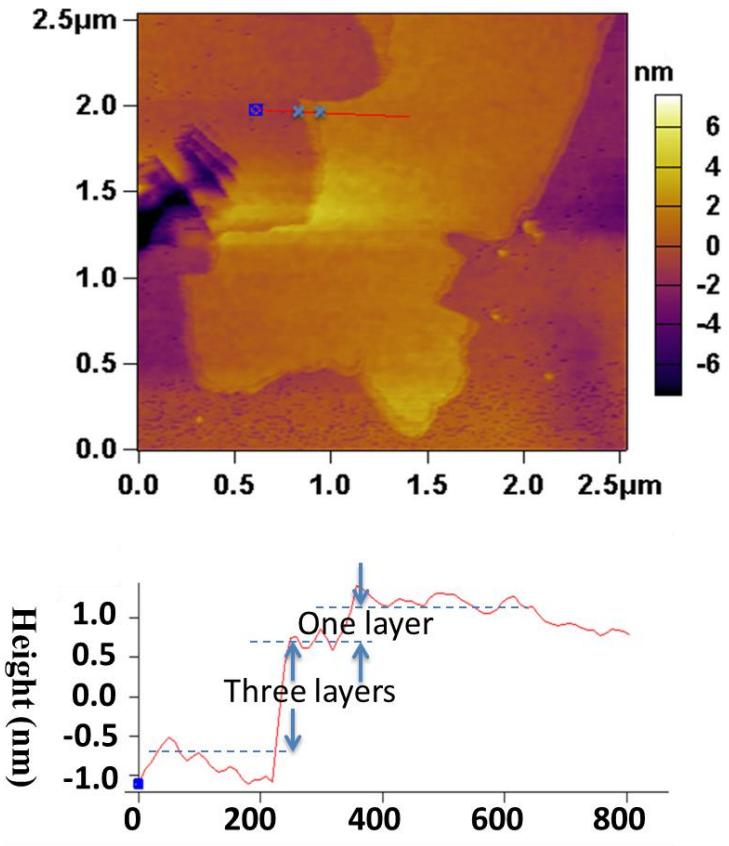

Figure 4.5. AFM topographic image and the corresponding height profile of OH-BNNS showing a terraced morphology with a mono-layered OH-BNNS joined to a tri-layered OH-BNNS.

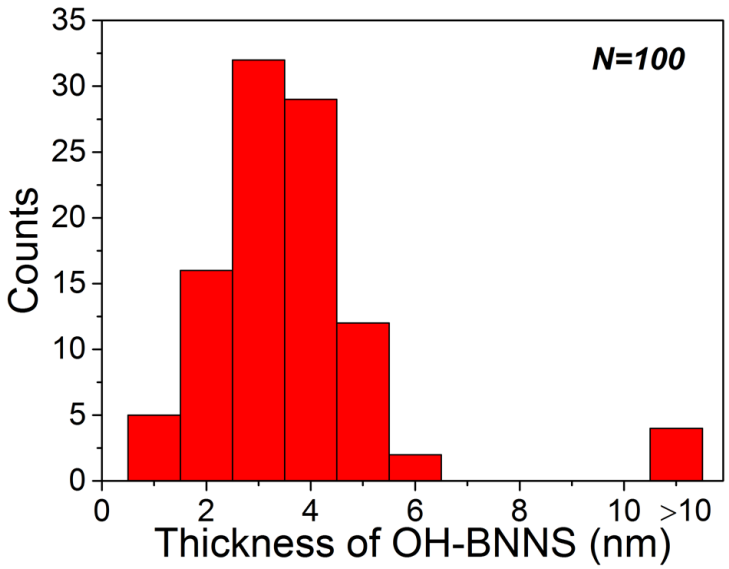

Figure 4.6. AFM derived statistical thickness of OH-BNNS obtained at 850 °C.

Similar to other nitrides, including Si_3N_4, TiN, and CrN, *h*-BN is also sensitive to moisture at elevated temperatures, due to the strong affinity of N towards O in H_2O.[20] After the heat treatment under hot steam, white ammonium pentaborate tetrahydrate ($NH_4B_5O_8{\cdot}4H_2O$) powder is deposited on the inner wall of the quartz tube downstream of the Ar outlet,[21] as confirmed by the X-ray diffraction (XRD) analysis (Figure 4.7). The initially pure deionized water in the disposal unit has a high level of ammonia, as confirmed by the Nessler's reagent test (Figure 4.8). The overall reaction can be described in Equation (4.1), which has also been observed before.[10, 22] The formation of $NH_4B_5O_8{\cdot}4H_2O$ is due to the reaction between NH_3 and H_3BO_3.

Equation (4.1)

$$BN + H_2O \rightarrow NH_3 + B(OH)_3$$

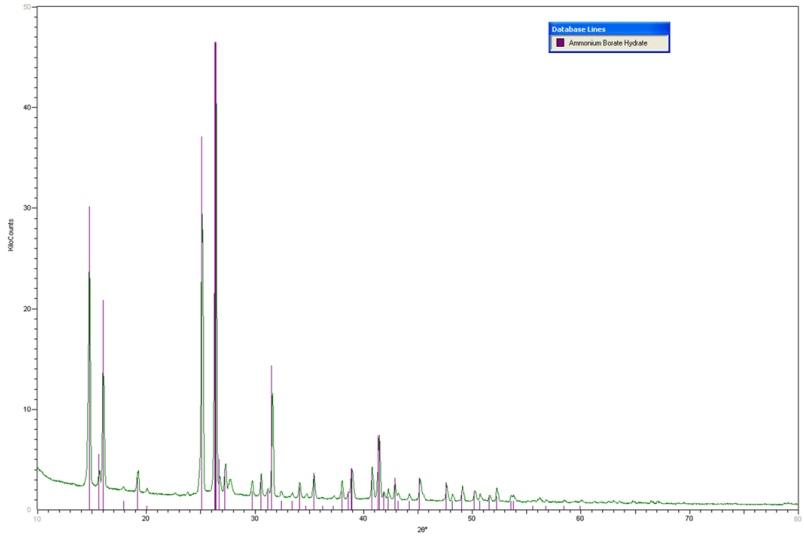

Figure 4.7. XRD pattern of the ammonium borate hydrate. (A white powder was scraped off from the tube wall downstream of the Ar outlet. The XRD pattern of the white powder has been well indexed to ammonium borate hydrate, which is formed by the reaction of boric acid with ammonium gas.)

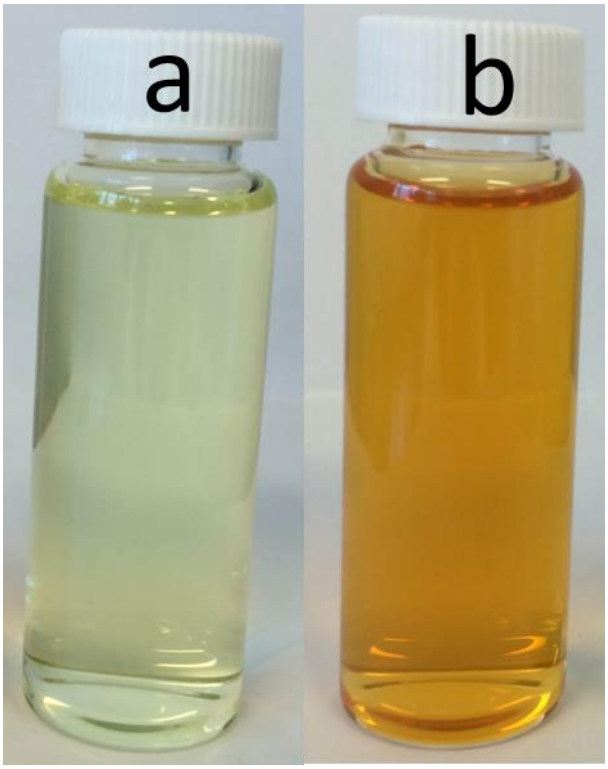

Figure 4.8. a) Nessler's reagent; b) Nessler's reagent upon adding solution from the bubbler. (The Nessler's reagent test is commonly used for ammonia detection. It turns the reagent a deeper yellow from a light yellow after several drops of solution have been added from the bubbler, indicative of the formation of NH_3 when hot water steam was blown over the BN.

The exfoliation is facilitated by the hydrolysis reaction at these high temperatures with the release of ammonia gas. The high thermal input at these temperatures would weaken the van der Waals forces between the BN layers. The hot H_2O gradually reacts with *h*-BN, forming voids (size depending on the temperature and reaction duration) on the (002) basal plane and along the edges, which would further weaken the van der Waals forces. The highly dynamic H_2O and NH_3 formed *in-situ* at such high temperatures may therefore penetrate through these voids and diffuse slowly between the BN layers, causing exfoliation, as evidenced by the SEM and TEM images (Figure 4.4a, b). AFM was used to measure the statistical thickness of the OH-BNNS[11] (Figure 4.6), which confirms that the final product has a thickness that

mainly varies from 1 to 5 nm, with ~20 % being 1-2 nm and over 60 % being 3-4 nm. This method gives a high yield of > 30 % for few-layered *h*-BNNS in the products. The yield of OH-BNNS could be controlled by optimizing the synthesis temperature and reaction duration. It's been found that the reaction rate is slow at 850 °C and the weight loss is only 5% in 2 h, suggesting that at this stage the majority of BN nanosheets remain as the solid product. Higher temperatures contribute to the formation of boric acid and consequently reduce the yields (Tables 4.1 and 4.2).

Table 4.1. (Yields of OH-BNNS at various temperatures)

Sample	Weight of bulk *h*-BN (g)	Weight (g) (after heating)	Purified weight (g)	Yields of products	Weight of OH-BNNS (g) (after separation)	Ratio of OH-BNNS among the products
BN850	1	0.95	n/a	95%	0.30	31.6%
BN950	1	0.98	0.8	80%*	0.15	18.75%
BN1050	1	1.1	0.65	65%*	0.08	12.3%

*: After removing boric acid

Table 4.2. OH contents (atomic percent) in the products obtained at various temperatures.

Sample	B	N	OH
BN850	50.44	44.41	5.15
BN950	50.27	43.50	6.23
BN1050	49.53	42.19	8.28

The functionalization occurs simultaneously with the hydrolysis, as illustrated in Figure 4.1. The driving force of the reaction is believed to be the formation of NH_3 as a leaving group. The exposed B atoms with dangling bonds then react with hydroxyl groups. The reaction in Equation (4.1) describes a situation where charge neutral H_3BO_3 is formed. In reality, tetrahedrally coordinated $N_3B(OH)$ is also formed.[16] The presence of –B(OH) can be verified using Fourier transform infrared (FTIR) spectroscopy and XRD.[10, 12, 23]

Two strong FTIR bands at ~1343 cm^{-1} and ~807 cm^{-1} are present in pristine *h*-BN, *h*-BN treated at 850 ºC (BN-850), and *h*-BN treated at 900 ºC (BN-900) (Figure 4.9a), which are correlated with the in-plane stretching and the out-of-plane bending mode of *h*-BN, respectively.[24] The red-shifts from 807 cm^{-1} for pristine *h*-BN to 787 cm^{-1} for BN-850, and 784 cm^{-1} for BN-900, are due to the disruption by hydroxyl groups, which leads to vibration at lower wavenumber.[12] A peak at 3440 cm^{-1}, assigned to the O-H stretching mode from the $N_3B(OH)$ unit, appears in the BN-850, which is consistent with previous results.[10, 12, 15, 16] Reactions at lower temperatures would not lead to an observable band at 3440 cm^{-1} (not shown here). For the BN-900, the O-H stretching mode at 3206 cm^{-1} and a new bending mode at 1200 cm^{-1} appear simultaneously, which are correlated with H_3BO_3, where boron is triangularly coordinated with oxygen.[25] This is confirmed by the XRD pattern (Figure 4.9b) of BN-900, where diffraction peaks associated with H_3BO_3 are clearly visible.[14] Based on the results obtained, it's been proposed the following explanation. H_3BO_3 has a low decomposition point (~170 ºC), but under the hot steam in the quartz tube, it can survive high temperatures. Additionally, it also has a low boiling point of 300 ºC, so it could evaporate away quickly. Based on the $NH_4B_5O_8{\cdot}4H_2O$ white powder obtained at the downstream outlet of the tube (for all the temperatures), it can be reasoned that most of the H_3BO_3 has been evaporated away. At 850 ºC, the evaporation rate is relatively faster than the formation rate of

H_3BO_3, leaving no H_3BO_3 in the final product. At 900 ºC a reverse trend occurs, and H_3BO_3 was observed in the final product, as confirmed by FTIR and XRD. The reactions were tried at higher temperatures with more H_3BO_3 observed in the final product (Table 1). Therefore, by adopting the optimum temperature, 850 ºC in this case, OH-BNNS can be obtained with an undetectable amount of impurities after a single heat treatment. Furthermore, the resultant OH-BNNS can be directly dispersed in solvents to be used as additives, avoiding tedious purification processes such as washing, centrifuging, and drying, which have been typically applied in the preparation of OH-BNNS.[12, 17, 26] The Raman spectra (Figure 4.9c) contain bands at 1362 cm^{-1} (BN-850) and 1360 cm^{-1} (BN-900), close to 1366 cm^{-1} for the commercial *h*-BN, all of which can be attributed to the E_{2g} mode vibration of *h*-BN. The slight red-shifts of 4 cm^{-1} (BN-850) and 6 cm^{-1} (BN-900) in relation to that of the pristine *h*-BN are another piece of evidence that the bulk *h*-BN has been exfoliated to produce predominantly few-layered nanosheets, which feature reduced interlayer interactions and shortening of the B-N bond.[12]

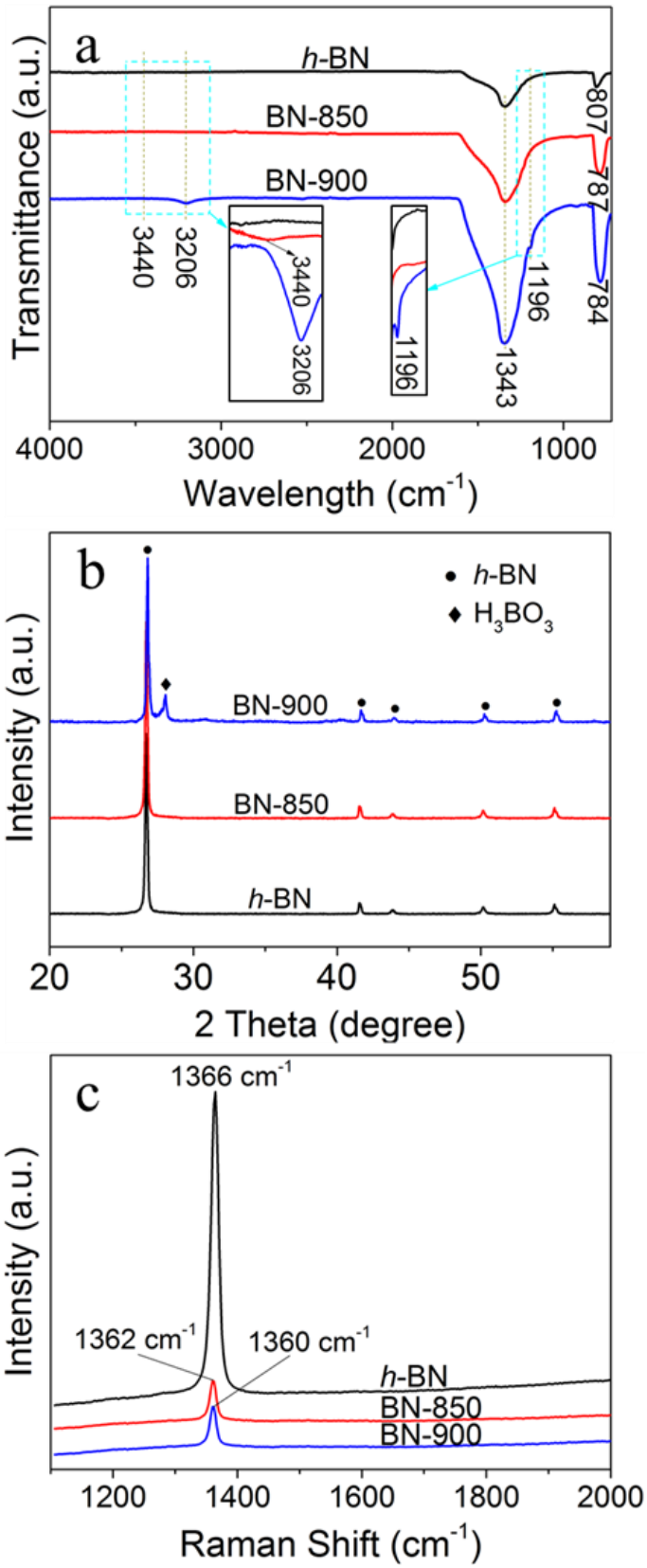

Figure 4.9. Pristine *h*-BN and *h*-BN treated at 850 ºC (denoted as BN-850) and 900 ºC (BN-900). a) FTIR spectra showing the presence of only -NB(OH)$_x$ in BN-850, as opposed to the

large amount of H_3BO_3 in BN-900; b) XRD patterns revealing the presence of H_3BO_3 in BN-900, which is negligible in BN-850. c) The red-shifts in the Raman spectra of the E_{2g} peak indicate the formation of few-layered BN at elevated temperatures.

FTIR and X-ray photoelectron spectroscopy (XPS) have been often used to validate the formation of OH-BNNS, but the location of OH groups on the plane has been vaguely described.[12, 15, 23] Aberration-corrected TEM is one of the most powerful tools to characterize matter at the sub-nanometer level. It is typically coupled with energy dispersive X-ray spectroscopy (EDS) to unequivocally identify elements present in the structure. EDS, however, is not reliable for light elements (O and lighter) due to many experimental factors. This limitation is overcome by the use of electron energy loss spectroscopy (EELS), where the light elements can be detected with the same resolution as the microscope. Here, EELS has been employed to probe the location of the OH groups in the BN sheets (Figure 4.10). Note that in these TEM images, the edges have the same intensity as the interior of the sheet, indicating that it is not a folding but a flat edge. Obviously, the O-K peak at ~532 eV in areas 2 and 3, which are along the edges of the OH-BNNS, and the disappearance of the O-K peak in areas 4, 5, and 6, which are away from the edges (Figures 4.10 and 4.11), suggesting that the *h*-BNNS have been functionalized predominately on the edges rather than on the basal plane. In addition, the presence of 1s-π^* and 1s-σ^* peaks of the N-K edge confirms that the intrinsic hexagonal structure of *h*-BN still remains.

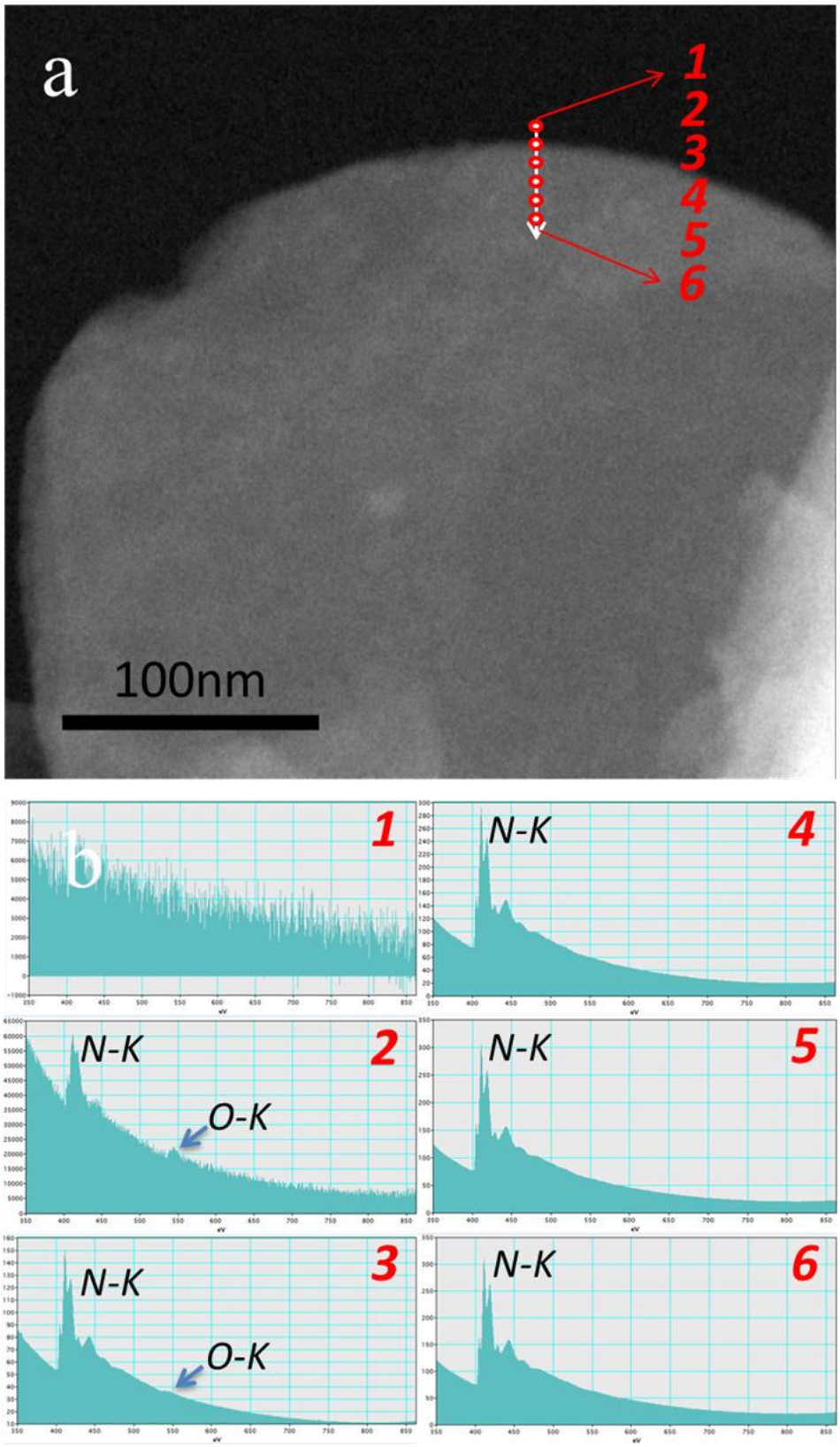

Figure 4.10. EELS mapping shows that the hydroxyl groups are predominately located along the edges of the nanosheets. Area 1 is off the OH-BNNS so no O-K or N-K peaks are observed; on moving to the edge of the OH-BNNS (area 2), the O-K peak appears and then

becomes weaker on moving away from the edge (area 3). The O-K peak is not observed when moving further into the basal plane (areas 4, 5, and 6). The presence of 1s-π* and 1s-σ* peaks of the N-K edge confirm that the intrinsic hexagonal structure of *h*-BN still remains.

Herein, it's been demonstrated the use of OH-BNNS as an effective additive to enhance the thermal response of poly(*N*-isopropylacrylamide) (PNIPAM) hydrogel. PNIPAM is one of the most widely studied temperature sensitive hydrogels, with applications ranging from drug delivery to various types of smart systems.[27] The efficacy of these applications is highly dependent on the critical response of the hydrogel to changes in temperature, which in most cases needs to be extremely fast. To take full advantage of the high thermal conductivity of *h*-BN as an additive, it is critical to well disperse the *h*-BN in the hydrogel network, which is not easy due to its hydrophobicity. In this work, the Raman mapping indicates that OH-BNNS is uniformly embedded in the hydrogel matrix rather than forming scattered aggregates (Figure 4.11c and d), The excellent dispersion can be ascribed to the extensive hydrogen bond network between the hydroxyl groups on the *h*-BNNS and –HN of *N*-isopropylacrylamide (Figure 4.11a). Such a uniform distribution would effectively favor the exploitation of the high intrinsic thermal conductivity of the *h*-BNNS, which consequently enhances heat transfer throughout the hydrogel network.

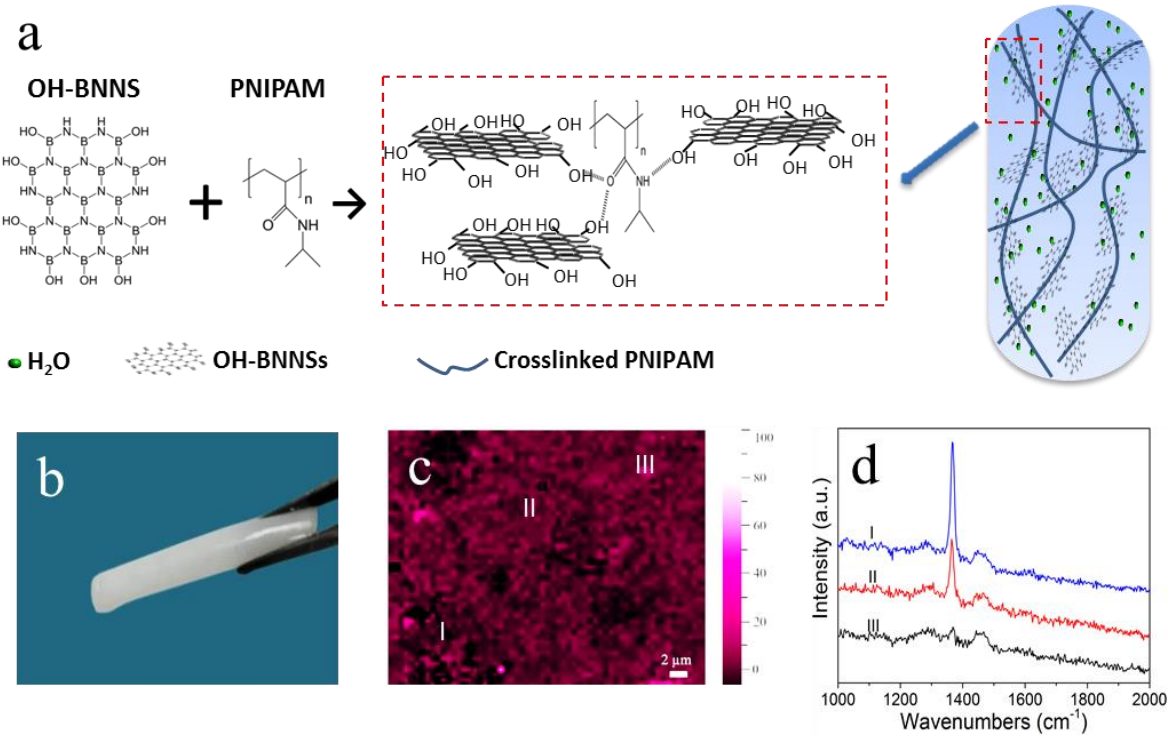

Figure 4.11. a) Schematic illustration of the formation of PNIPAM/OH-BNNS hydrogel, where the cross-linked PNIPAM and OH-BNNS are integrated through hydrogen bonding, b) photographic image of PNIPAM/OH-BNNS hydrogel, c) Raman mapping collected at 1362 cm^{-1}, showing the uniform distribution of the OH-BNNS in the hydrogel network, and d) Raman spectra of three points with maximum (III), mean (II), and minimum (I) intensity, judged by human eyes. The featured peaks of PNIPAM (at ~1450 cm^{-1}) and OH-BNNS (~1360 cm^{-1}) have an independent existence.

As a well-known temperature sensitive hydrogel, PNIPAM becomes opaque and shrinks at the same time when heated above ~32 ºC, and it returns back to its initial state when the temperature is reduced below the transition temperature. A faster change in opacity and size indicates a better temperature response, which is critical for practical applications. Such an improvement was observed in the response of the PNIPAM/OH-BNNS hydrogels to temperature changes. The addition of only 0.07 wt% (based on polymer precursor) OH-

BNNS to the hydrogel improved the thermal conductivity by 41% (Figure 4.12a). When the PNIPAM/OH-BNNS hydrogel composite and pure PNIPAM were taken out of warm water at 50 ºC, the former showed a much faster change in transparency than the latter, with a maximum 40% margin (Figure 4.12b), indicative of the pivotal role of OH-BNNS in the thermal enhancement.

As the dimensions of the hydrogel have an inverse temperature dependence, another test was carried out to compare the rate of the length change of cylindrical samples when the temperature was increased from room temperature to 50 ºC. Both hydrogels were made under the exact same conditions with the same dimensions. The PNIPAM/OH-BNNS hydrogel composite shows faster length change (inset in Figure 4.12c). Specifically, the greatest difference in length appears at 30 seconds, when the hydrogel composite has shrunk to 3.8 cm from 4.2 cm, a 5-fold greater shrinking rate than that of its neat counterpart, which has shrunk from 4.2 cm to 4.15 cm. Finally, after 6 minutes, the lengths of both hydrogels are nearly the same. The faster response rate is attributed to the highly improved thermal conductivity across the composite due to the presence of OH-BNNS sheets. This faster change in dimension would make the PNIPAM/OH-BNNS hydrogel composite a better candidate for actuator applications (e.g. valves) that work by thermal stimulation.

Dye release from the hydrogels was also tested, which provides a simple simulation of the releasing process for drug solutions. Since PNIPAM hydrogels undergo large volume deformation upon heating, the drug molecules can be "squeezed" out of the hydrogel composite. Blue dye (blue food coloring) was loaded on both neat and composite hydrogels in the same petri dish, until both reached equilibrium with an identical dark blue color, as perceived by human eyes. They were then put into warm water (T = 40 ºC) for dye release.

After 0.5 minutes, the PNIPAM/OH-BNNS hydrogel began releasing the dye, while the neat hydrogel showed no detectable change in color (Figure 4.12d). At 3 minutes, the color of the PNIPAM/OH-BNNS hydrogel became a lighter blue, indicating that more dye had been released during the same period than for the neat hydrogel. The faster dye release upon temperature change again indicates that the well-dispersed OH-BNNS improves heat conductivity. PNIPAM/OH-BNNS hydrogels therefore could show a prompt response to their environmental temperature to deliver drug solutions more effectively than the corresponding neat ones.

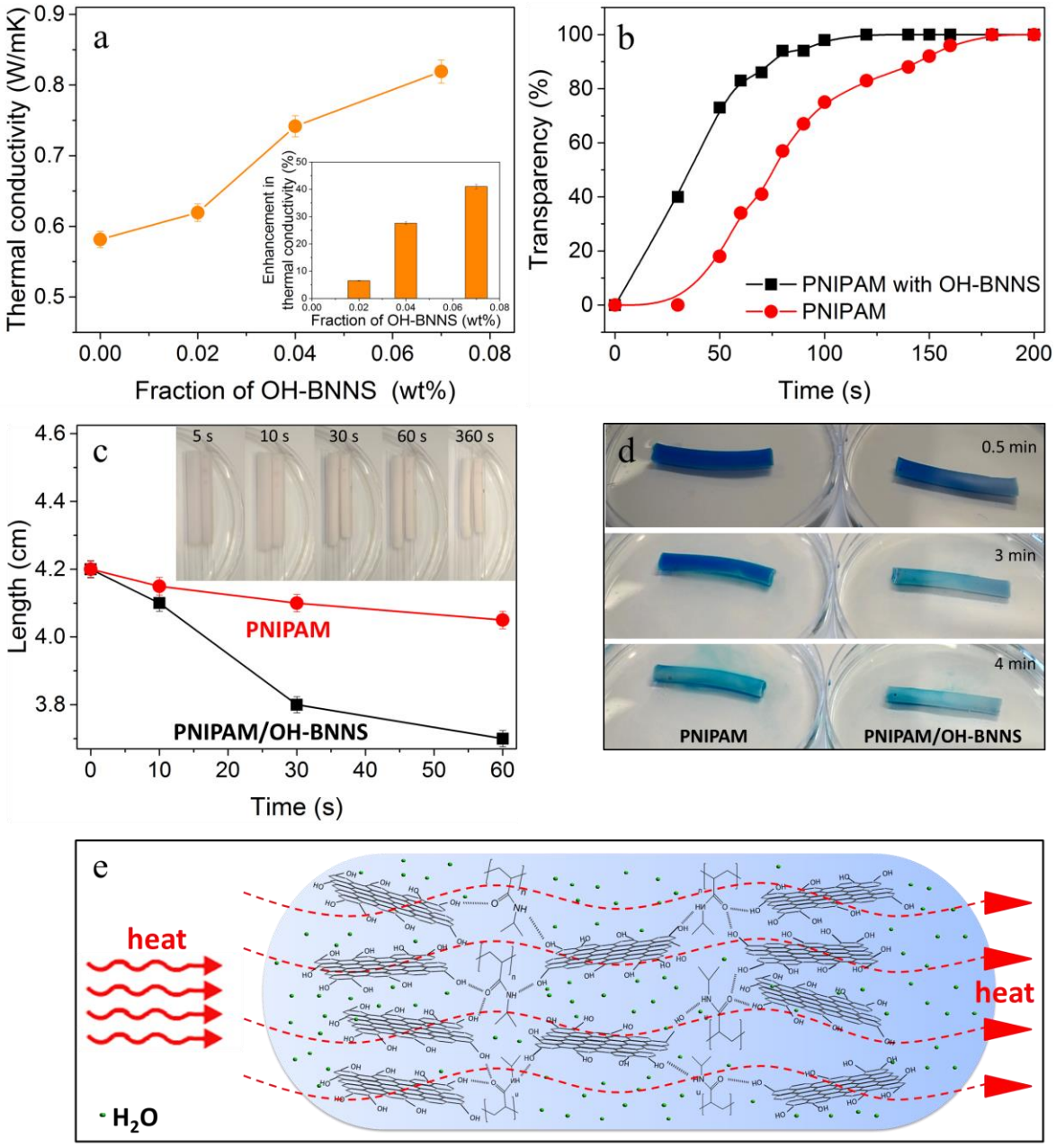

Figure 4.12. a) Thermal conductivity improvement with the ratio of OH-BNNS (inset: the improvement by percentage), b) change in transparency, c) change in length of cylindrical samples (inset: photographs of hydrogels at different times, with PNIPAM on the left and PNIPAM/OH-BNNS on the right), d) dye release upon heating, and e) schematic illustration of the enhanced heat transfer in PNIPAM/OH-BNNS hydrogel, which has resulted from the excellent integration between the OH-BNNS, H_2O, and the cross-linked PNIPAM through hydrogen bonding.

As discussed above, the treatment of bulk *h*-BN powder at high temperatures under steam leads to simultaneous exfoliation and functionalization of the *h*-BN. The resultant OH-BNNS is edge-modified and hydrophilic enough to form good suspensions in water and alcohol. Moreover, when mixed with polymers soluble in water or alcohol, the OH groups on the nanosheet edges appear to be conducive to a collective interaction between the *h*-BNNS and the polymer, most likely through hydrogen bonding, and thus, no phase segregation takes place. This is evidenced by the Raman mapping collected at 1362 cm^{-1} (Figure 4.11c-d), which reveals a uniform distribution of *h*-BNNS across the hydrogel network. It is important to note that there is no obstacle to using other hydrophilic monomers and polymers to prepare hydrogel composites, so long as the precursors are soluble in water or ethanol. Indeed, uniform poly(ethylene glycol)/OH-BNNS and poly(hydroxyethylmethacrylate)/OH-BNNS composites have been successfully fabricated.

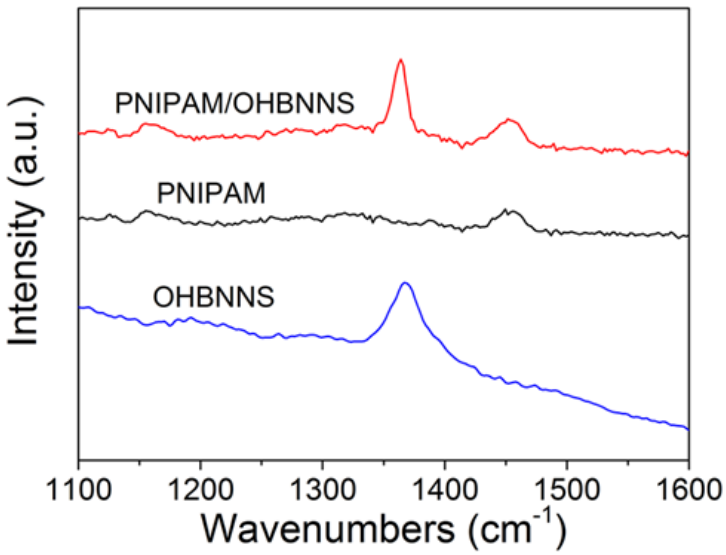

Figure 4.13. Raman spectra of OH-BNNS, PNIPAM, and PNIPAM/OH-BNNS. For the Raman spectrum of PNIPAM/OH-BNNS, the featured peaks of PNIPAM (at ~1450 cm^{-1}) and OH-BNNS (~1360 cm^{-1}) are of independent existence.

It is well known that water-PNIPAM interaction and water-water interaction in the hydrogel is highly sensitive to changes in temperature. Below the lower critical solution temperature (LCST), hydrophilic amide (-NH) and carbonyl (-CO) groups form hydrogen bonds with water molecules, with the interaction dominated by an enthalpic term. Once above the LCST, the entropic gain overcomes the enthalpic term, and water molecules are released.[27] How to effectively transfer the heat to "all" the molecules so to speed up their response is critical for any thermal-stimulus applications. These intermolecular hydrogen bond interactions between water and OH-BNNS, as well as PNIPAM and OH-BNNS, allow the OH-BNNS to act as a thermal carrier to continuously and effectively diffuse the heat throughout the hydrogel composite matrix (Figure 4.12e), which consequently enhances the thermally stimulated performance of PNIPAM/OH-BNNS hydrogel according to the tests above. The absence of -OH groups on the basal plane is also advantageous, since otherwise, deformation of the *h*-BNNS plane would occur, especially in the case of hydrogen bonding. It's been also found that OH-BNNS can effectively improve the thermal conductivity of the NIPAM/water mixture and even pure water (Table 4.3), which is critical, since the hydrogel contains a large amount of water (> 80 % by weight). The improvement is likely due to the high phonon transport along the OH-BNNS basal planes [6, 28]. The interfacial thermal contact resistance is minimized due to the large contact area between the OH-BNNS and the polymer, as well as the water. In addition, the close interaction through hydrogen bonding will effectively facilitate the transport of phonons between the BN sheets. It's been believed that the presence of OH groups has not appreciably perturbed the crosslinking efficiency of the hydrogel, which significantly affects the response time when the temperature is changed. The swelling (change in mass) ratio of the hydrogel remained unchanged, ~ 9.2 +/- 0.1, when OH-BNNS was added (at the concentration range studied here). No change was observed in the LCST of the polymer (all around 32 °C) upon adding OH-BNNS. In addition, the shrinkage ratios of

the hydrogels with and without OH-BNNS are the same, although the rates of dimensional change are different (Figure 4.12d). Therefore, the thermal enhancement is predominantly caused by the incorporated OH-BNNS. A simple simulation (Figure 4.14) indicates that the experimental data are close to the those predicted using a parallel conduction model.[29] It should be noted that, in the parallel model, the conductive filler is arranged in parallel with the direction of thermal flux, which is the most ideal case. It should be noted that the thermal contacts between any interfaces are normally poor. It's been confirmed the good dispersion of OH-BNNS in the hydrogel composite with excellent contact between the OH-BNNS and PNIPAM hydrogel through hydrogen bonding. The λ_f used here is 360 W/mK, which is the experimental value for 11-layered *h*-BN with trace of poly(methyl methacrylate)(PMMA), and it was suggested that the ineffective removal of the PMMA residue would degrade the thermal performance.[30] It should also be noted that thermal conductivity of single-layered *h*-BN can be over 1000 W/mK.[31] In this case, there is a proportion of few-layered, including monolayer, OH-BNNS, which could contribute more thermal enhancement than relatively thick OH-BNNS. It's thus likely that the experimental value of the 0.04 wt% loading is close to the simulated value.

Table 4.3. Thermal conductivities of DI water, DI water/NIPAM, DI water/OH-BNNS and DI water/NIPAM/OH-BNNS.

Sample	DI water	DI water/NIPAM	DI water /OH-BNNS	DI water /NIPAM/OH-BNNS
Thermal conductivity (W/mK)	0.61	0.56	0.66	0.64

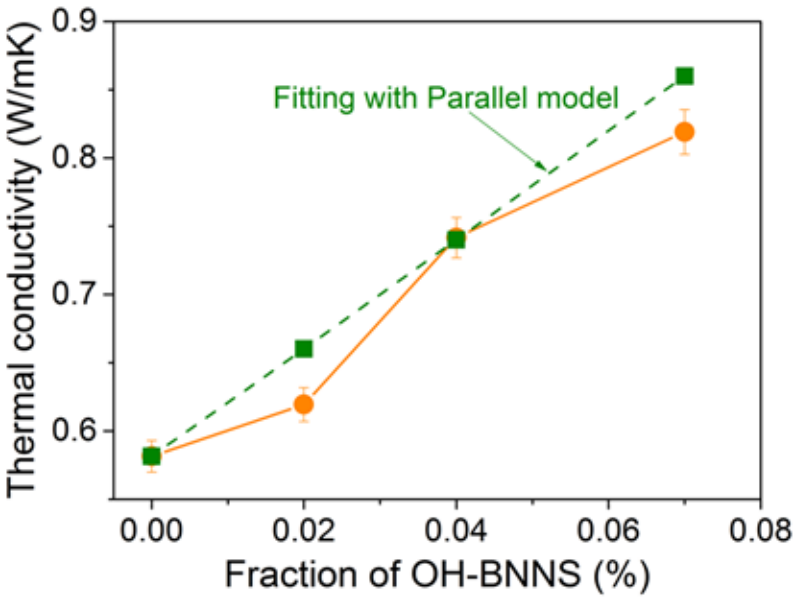

Figure 4.14. Thermal conductivity of the hydrogel composite as a function of OH-BNNS content. Solid line: experimental values; Dashed line: simulated results using a parallel model.

The thermal conductivity of the PNIPAM/OH-BNNS hydrogel composite as a function of the filler content was simulated using a parallel conduction model.[33]

$$\lambda = V \cdot \lambda_f + (1 - V) \cdot \lambda_p$$

where λ = thermal conductivity of the composite, λ_p = thermal conductivity of the neat hydrogel, λ_f = thermal conductivity of the filler, and V = volume content of the filler. As the loading of OH-BNNS is very low, the density of the hydrogel is assumed as same as OH-BNNS. The thermal conductivity of *h*-BN is taken as 360 W/mK, an experimental value for 11 layers of *h*-BN.[34]

The hydrogels need to maintain suitable mechanical properties for practical applications. All polymerization solutions made with OH-BNNS dispersions remained stable for several days

until they were polymerized, after which, the nanosheets were fully locked into the network. Over 5 tests, no significant improvement in the Young's modulus was observed when OH-BNNS was incorporated into the hydrogel formulation. Some improvements were obtained from compression testing of the hydrogel composites, where PNIPAM/OH-BNNS hydrogels exhibited a higher compression strength and final strain (Figure 4.15).

Notably, *h*-BNNS is known to be non-cytotoxic and has been studied for therapeutic or diagnostic applications.[16, 32] The PNIPAM/OH-BNNS hydrogel composite is not expected to be cytotoxic either. Therefore, the dramatic improvement in the response to external heat stimulation could be very beneficial for a wide range of bionic and soft robotic applications.

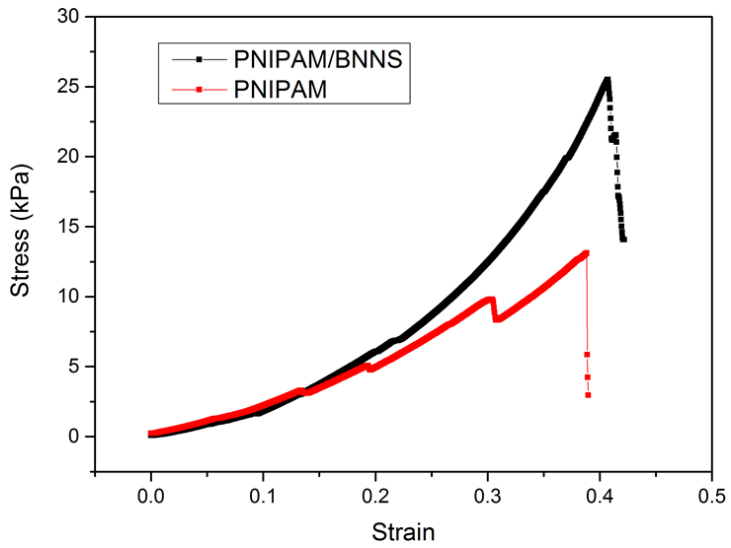

Figure 4.15. Compression test of PNIPAM/OH-BNNS and PNIPAM.

4.4 Conclusion

In summary, a facile and scalable method has been developed to directly exfoliate and functionalize intrinsically hydrophobic bulk *h*-BN into hydrophilic OH-BNNS. The hydroxyl groups are predominantly located along the edges of the nanosheets rather than on the basal plane. The excellent dispersibility of OH-BNNS in water and alcohol makes it an effective

additive to hydrogels. The intrinsic thermal properties have been perfectly inherited, since the resultant OH-BNNS exhibited large and few-layered morphology rather than the small fragments produced by the sonication-based exfoliation. The PNIPAM/OH-BNNS hydrogel composite shows a much faster thermal response compared to the bare hydrogel, with a 41% improvement in thermal conductivity achieved by adding only 0.07 wt% OH-BNNS. The hydrogel composite also shows faster dimensional change upon heating, with the discrepancy proving that OH-BNNS has passed on its excellent thermal properties to the PNIPAM hydrogel. Most interestingly, the dye-release test demonstrates its improved drug delivery capability. According to the merits above, this PNIPAM/OH-BNNS with its superior thermal response is envisaged to be a promising candidate in the field of bionic and soft robotic applications.

4.5 Reference

[1] A. Pakdel, Y. Bando, D. Golberg, Chemical Society Reviews 2014, 43, 934; X.-F. Jiang, Q. Weng, X.-B. Wang, X. Li, J. Zhang, D. Golberg, Y. Bando, Journal of Materials Science & Technology 2015, 31, 589.

[2] M. Wang, S. K. Jang, W.-J. Jang, M. Kim, S.-Y. Park, S.-W. Kim, S.-J. Kahng, J.-Y. Choi, R. S. Ruoff, Y. J. Song, S. Lee, Adv. Mater. 2013, 25, 2746; W. Yang, G. Chen, Z. Shi, C.-C. Liu, L. Zhang, G. Xie, M. Cheng, D. Wang, R. Yang, D. Shi, K. Watanabe, T. Taniguchi, Y. Yao, Y. Zhang, G. Zhang, Nat Mater 2013, 12, 792.

[3] L. H. Li, J. Cervenka, K. Watanabe, T. Taniguchi, Y. Chen, ACS Nano 2014, 8, 1457.

[4] M. Yi, Z. Shen, X. Zhao, S. Liang, L. Liu, Applied Physics Letters 2014, 104.

[5] D.-H. Cho, J.-S. Kim, S.-H. Kwon, C. Lee, Y.-Z. Lee, Wear 2013, 302, 981.

[6] J. Taha-Tijerina, T. N. Narayanan, G. Gao, M. Rohde, D. A. Tsentalovich, M. Pasquali, P. M. Ajayan, ACS Nano 2012, 6, 1214.

[7] W.-L. Song, P. Wang, L. Cao, A. Anderson, M. J. Meziani, A. J. Farr, Y.-P. Sun, Angewandte Chemie 2012, 124, 6604.

[8] C. Zhi, Y. Bando, C. Tang, H. Kuwahara, D. Golberg, Adv. Mater. 2009, 21, 2889; X.-B. Wang, Q. Weng, X. Wang, X. Li, J. Zhang, F. Liu, X.-F. Jiang, H. Guo, N. Xu, D. Golberg, Y. Bando, ACS Nano 2014, 8, 9081; X. Wang, C. Zhi, L. Li, H. Zeng, C. Li, M. Mitome, D. Golberg, Y. Bando, Adv. Mater. 2011, 23, 4072; H. Zhu, Y. Li, Z. Fang, J. Xu, F. Cao, J. Wan, C. Preston, B. Yang, L. Hu, ACS Nano 2014, 8, 3606; C. Zhi, Y. Xu, Y. Bando, D. Golberg, ACS Nano 2011, 5, 6571; X. Wang, A. Pakdel, J. Zhang, Q. Weng, T. Zhai, C. Zhi, D. Golberg, Y. Bando, Nanoscale Res Lett 2012, 7, 662.

[9] J. N. Coleman, M. Lotya, A. O'Neill, S. D. Bergin, P. J. King, U. Khan, K. Young, A. Gaucher, S. De, R. J. Smith, I. V. Shvets, S. K. Arora, G. Stanton, H.-Y. Kim, K. Lee, G. T. Kim, G. S. Duesberg, T. Hallam, J. J. Boland, J. J. Wang, J. F. Donegan, J. C. Grunlan, G.

Moriarty, A. Shmeliov, R. J. Nicholls, J. M. Perkins, E. M. Grieveson, K. Theuwissen, D. W. McComb, P. D. Nellist, V. Nicolosi, Science 2011, 331, 568.

[10] Y. Lin, T. V. Williams, T.-B. Xu, W. Cao, H. E. Elsayed-Ali, J. W. Connell, The Journal of Physical Chemistry C 2011, 115, 2679.

[11] K. R. Paton, E. Varrla, C. Backes, R. J. Smith, U. Khan, A. O'Neill, C. Boland, M. Lotya, O. M. Istrate, P. King, T. Higgins, S. Barwich, P. May, P. Puczkarski, I. Ahmed, M. Moebius, H. Pettersson, E. Long, J. Coelho, S. E. O'Brien, E. K. McGuire, B. M. Sanchez, G. S. Duesberg, N. McEvoy, T. J. Pennycook, C. Downing, A. Crossley, V. Nicolosi, J. N. Coleman, Nat Mater 2014, 13, 624.

[12] T. Sainsbury, A. Satti, P. May, Z. Wang, I. McGovern, Y. K. Gun'ko, J. Coleman, Journal of the American Chemical Society 2012, 134, 18758.

[13] Q. Tang, Z. Zhou, P. Shen, Z. Chen, ChemPhysChem 2013, 14, 1787; Q. Tang, J. Bao, Y. Li, Z. Zhou, Z. Chen, Nanoscale 2014, 6, 8624.

[14] Z. Cui, A. J. Oyer, A. J. Glover, H. C. Schniepp, D. H. Adamson, Small 2014, 10, 2352.

[15] G. R. Bhimanapati, D. Kozuch, J. A. Robinson, Nanoscale 2014, 6, 11671.

[16] Q. Weng, B. Wang, X. Wang, N. Hanagata, X. Li, D. Liu, X. Wang, X. Jiang, Y. Bando, D. Golberg, ACS Nano 2014, 8, 6123.

[17] X. Li, X. Hao, M. Zhao, Y. Wu, J. Yang, Y. Tian, G. Qian, Adv. Mater. 2013, 25, 2200.

[18] Y. Hernandez, V. Nicolosi, M. Lotya, F. M. Blighe, Z. Sun, S. De, I. T. McGovern, B. Holland, M. Byrne, Y. K. Gun'Ko, J. J. Boland, P. Niraj, G. Duesberg, S. Krishnamurthy, R. Goodhue, J. Hutchison, V. Scardaci, A. C. Ferrari, J. N. Coleman, Nat Nano 2008, 3, 563.

[19] Y. Lin, J. W. Connell, Nanoscale 2012, 4, 6908; S. Park, R. S. Ruoff, Nat Nano 2009, 4, 217.

[20] S. Motojima, Y. Tamura, K. Sugiyama, Thin Solid Films 1982, 88, 269; C. G. Cofer, J. Economy, Carbon 1995, 33, 389.

[21] T. Matsuda, J Mater Sci 1989, 24, 2353.

[22] T. Saito, F. Honda, Wear 2000, 237, 253.

[23] A. S. Nazarov, V. N. Demin, E. D. Grayfer, A. I. Bulavchenko, A. T. Arymbaeva, H.-J. Shin, J.-Y. Choi, V. E. Fedorov, Chemistry – An Asian Journal 2012, 7, 554; Y. Lin, T. V. Williams, W. Cao, H. E. Elsayed-Ali, J. W. Connell, The Journal of Physical Chemistry C 2010, 114, 17434.

[24] R. Geick, C. H. Perry, G. Rupprecht, Physical Review 1966, 146, 543.

[25] S. Anderson, R. L. Bohon, D. D. Kimpton, Journal of the American Ceramic Society 1955, 38, 370.

[26] M. Du, X. Li, A. Wang, Y. Wu, X. Hao, M. Zhao, Angewandte Chemie International Edition 2014, 53, 3645.

[27] Y. Qiu, K. Park, Advanced Drug Delivery Reviews 2012, 64, Supplement, 49; X. Zhang, C. L. Pint, M. H. Lee, B. E. Schubert, A. Jamshidi, K. Takei, H. Ko, A. Gillies, R. Bardhan, J. J. Urban, M. Wu, R. Fearing, A. Javey, Nano Letters 2011, 11, 3239; C. Yu, Z. Duan, P. Yuan, Y. Li, Y. Su, X. Zhang, Y. Pan, L. L. Dai, R. G. Nuzzo, Y. Huang, H. Jiang, J. A. Rogers, Adv. Mater. 2013, 25, 1541.

[28] C. Zhi, Y. Bando, T. Terao, C. Tang, H. Kuwahara, D. Golberg, Advanced Functional Materials 2009, 19, 1857.

[29] Y. Agari, T. Uno, Journal of Applied Polymer Science 1986, 32, 5705.

[30] I. Jo, M. T. Pettes, J. Kim, K. Watanabe, T. Taniguchi, Z. Yao, L. Shi, Nano Letters 2013, 13, 550.

[31] L. Lindsay, D. A. Broido, Physical Review B 2011, 84, 155421.

[32] X. Chen, P. Wu, M. Rousseas, D. Okawa, Z. Gartner, A. Zettl, C. R. Bertozzi, Journal of the American Chemical Society 2009, 131, 890; L. Horváth, A. Magrez, D. Golberg, C. Zhi, Y. Bando, R. Smajda, E. Horváth, L. Forró, B. Schwaller, ACS Nano 2011, 5, 3800.

[33] Y. Agari, T. Uno, Journal of Applied Polymer Science 1986, 32, 5705.

[34] I. Jo, M. T. Pettes, J. Kim, K. Watanabe, T. Taniguchi, Z. Yao, L. Shi, Nano Letters 2013, 13, 550.

Chapter 5 Few-layered and hierarchically porous boron nitride nanosheets

5.1 Introduction

Hexagonal boron nitride nanosheets (*h*-BNNS) are an inorganic analogue of graphene and one of the most studied two-dimensional (2D) materials. *h*-BNNS possesses fascinating properties such as superb mechanical strength and high thermal conductivity.[1-3] *h*-BNNS have thus been explored as reinforcing nanofillers to enhance the mechanical and thermal performances of composites.[4-6] Moreover, *h*-BNNS show unique properties that are absent in their carbon counterparts, such as high electrical resistance, excellent oxidation resistance, and chemical inertness in harsh environments.[7-9] These properties have provided the driving force behind the booming interest in *h*-BNNS for a diversity of applications, such as drug delivery, pollution remediation, anticorrosion coatings, and insulating substrates.[10-14] As a result, intensive efforts have been devoted to the synthesis of high-quality, few-layered *h*-BNNS in quantities suitable for large-scale applications. One of the most common ways to produce *h*-BNNS is through sonication-assisted exfoliation of bulk hexagonal boron nitride (*h*-BN) in selected polar solvents, such as isopropyl alcohol, *N,N'*-dimethylformamide, and water.[4,15-17] These methods have led to *h*-BNNS with a large distribution of layer numbers (from few to hundreds), and the resultant sheets tend to have a small lateral size (less than 1 mm). In addition, the sonication-assisted method normally requires many hours, and the yield is not satisfactory.[16,17] Thus, a scalable synthesis of *h*-BNNS with controllable layer thickness is keenly sought after.

Template-based methods have been used to make highly ordered porous BN structures.[18–20] These methods have several disadvantages, however, such as difficulties in efficient filling of the nanopores and complete removal of the template. Furthermore, for large-scale production, the cost of the template could be very high. Template-free and dynamic-template

strategies have been introduced more recently to synthesize porous BN in forms such as sponges, belts, and ribbons.[13,21,22] It remains a critical challenge to control the morphology of porous BN as a 2D sheet structure.

Herein, a controllable bottom-up synthesis of few-layered porous *h*-BNNS has been reported. This strategy employs the unique crystal structure of MgB_2, where Mg atoms are sandwiched by boron sheets (Figure 5.1a). During the reaction, *h*-BNNS formation is constrained by the formation and decomposition of Mg-based by-products, and as a result, only few-layered nanosheets with controlled pore size are obtained. The resultant porous *h*-BNNS show good CO_2/N_2 selectivity and adsorption capability.

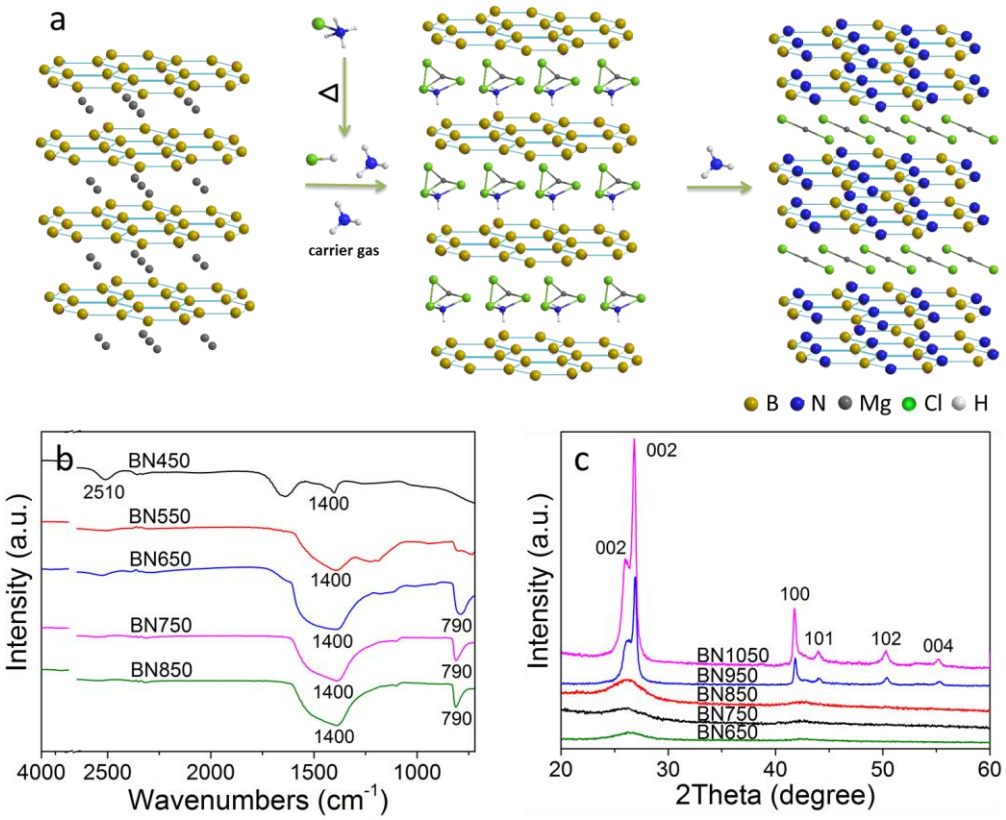

Figure 5.1. (a) Schematic diagrams of synthesis of *h*-BNNS. (b) Fourier transform IR (FTIR) spectra, and (c) XRD patterns of the samples obtained at different temperatures. The product

obtained at 450 °C is denoted as BN450, and the same notation has been applied to all the samples.

5.2 Experimental section

Synthesis

Magnesium diboride (MgB_2, Alfa Aesar) and ammonium chloride (NH_4Cl, Sigma Aldrich) were used as received. In a typical experiment, MgB_2 (0.1840 g) and NH_4Cl (1.2840 g) were ground together into a homogeneous mixture in a glove box and then transferred into a boron nitride crucible. The reaction was carried out in a tube furnace with a fused quartz tube (50 mm inside and 55 mm outside diameter). The quartz tube was evacuated 3 times and filled with Ar in between. Subsequently, the mixture was treated under ammonia at varied temperatures from 450-1050 °C for 2h. A high flow rate of 200 sccm was used to prevent the formation of solid products that may cause blockage. After the reaction, the furnace was naturally cooled down to room temperature. The product was washed with 1 M hydrochloride acid and deionized (DI) water, dried at 80 °C overnight, and then collected for further characterizations.

Characterization

X-ray powder diffraction (XRD) patterns were obtained on a GBC MMA (Cu Kα, λ = 0.15406 nm). Fourier transform infrared (FTIR) spectra were collected using a Shimadzu FTIR Prestige-21. Raman spectra were obtained at room temperature using a Horiba JobinYvon/LabRAM HR8000 with a laser source at 632.8 nm. X-ray photoelectron spectroscopy analysis (XPS, PHOIBOS 100 hemispherical analyser SPECSGmbH) was

carried out at the energy of 486.6 eV. High resolution transmission electron microscope images were acquired in JEOL 2011 and JEOL ARM200F at an 80 kV accelerating voltage. Gas adsorption studies were carried out using a Quantachrome Autosorb MP instrument, with high purity nitrogen (99.999 %) and carbon dioxide (99.995 %) gasses at the Wollongong Isotope and Geochemistry Laboratory, UOW. Surface areas were determined using Brunauer-Emmett-Teller (BET) calculations.

5.3 Results and discussion

The dynamic template afforded by the layered structure of MgB_2 is the key to producing few-layered porous *h*-BNNS (Figure 5.1a). During the synthesis, NH_4Cl is introduced as an etchant and NH_3 as the nitrogen source to form *h*-BNNS. The final products were washed with dilute hydrochloric acid and deionized water prior to characterization. At temperatures lower than 450 °C, the final solid product appears brownish, indicating the formation of elemental boron. At 450 °C, the B-N stretching mode at 1400 cm^{-1} becomes visible in the infrared (IR) spectra (Figure 5.1b). With increasing temperature, *h*-BN starts to dominate the products, as confirmed by the growth in intensity of the IR bands at 1400 cm^{-1} and 790 cm^{-1} that are associated with the stretching and bending modes of B-N vibrations, respectively (Figure 5.1b). The X-ray diffraction (XRD) results (Figure 5.1c) agree well with the IR results, in that temperatures of 550 °C and above facilitate the formation of BN. When the synthesis temperatures were elevated to 950 °C and 1050 °C, the products evolved into a mixture of *h*-BN and turbostratic boron nitride (*t*-BN), with an extra set of (002), (100), (101), (102), and (004) peaks appearing (Figure 5.1c). *t*-BN consists of partially disordered BN layers with interspacing larger than that of *h*-BN.[23,24]

To further elucidate the reaction mechanism, the reaction was carried out at the lower temperature of 350 °C. The resultant product was identified from its XRD pattern as ammonium magnesium chloride (NH_4MgCl_3), with the hydrate formed because NH_4MgCl_3 is hygroscopic (Figure 5.2). The likely process involves the decomposition of NH_4Cl (decomposes around 338 °C) into NH_3 and HCl, which then reacts with MgB_2, forming NH_4MgCl_3 and elemental boron. At higher temperatures, the elemental boron formed in situ reacts with NH_3 to form BN (Figure 5.1a), and the NH_4MgCl_3 decomposes to NH_3, HCl, and amorphous $MgCl_2$.[25] $MgCl_2$ would be present throughout the thermal process (m.p. 714 °C; b.p. 1412 °C), playing a vital role in preventing the BN layers from aggregating.

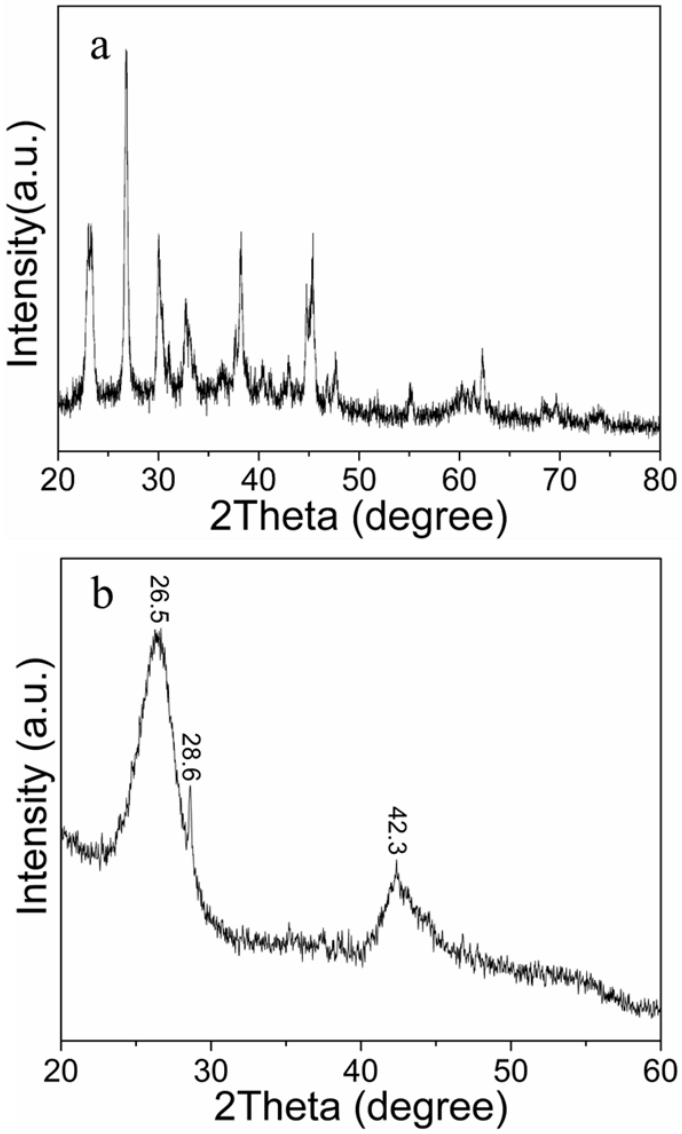

Figure 5.2. XRD patterns of the solid product obtained at a) 350 °C and b) 650 °C without any treatment. At 350 °C, NH_4Cl decomposes into NH_3 and HCl, which react with MgB_2, forming ammonium magnesium chloride (hydrated when exposed to air). At 650 °C, Mg-based byproducts exist in the whole process and finally form into MgO.

X-ray photoelectron spectroscopy (XPS) was used to determine the chemical compositions of the products. The full survey spectrum reveals the presence of B, N, and C (Figure 5.3a), indicating that Mg and Cl have been largely removed. The C element can be assigned to the carbon tape used as the substrate for the specimen. Two dominant peaks in the spectra (Figure 5.3b and c) are located at 190.7 eV (B 1s) and 398.0 eV (N 1s), in close agreement with the reported values for *h*-BN.[3] Energy dispersive spectroscopy (EDS) under transmission electron microscopy (TEM) (Figure 5.4) also reveals the presence of B, N, C, and O, and negligible amounts of Mg. The formation of *h*-BNNS is also confirmed by the Raman spectra, where the E_{2g} mode centred around 1364 cm^{-1} is observed (Figure 5.5) for BN1050, and redshifts are observed for both BN850 and BN650, indicating reduced thickness of the *h*-BNNS with lower synthesis temperatures.

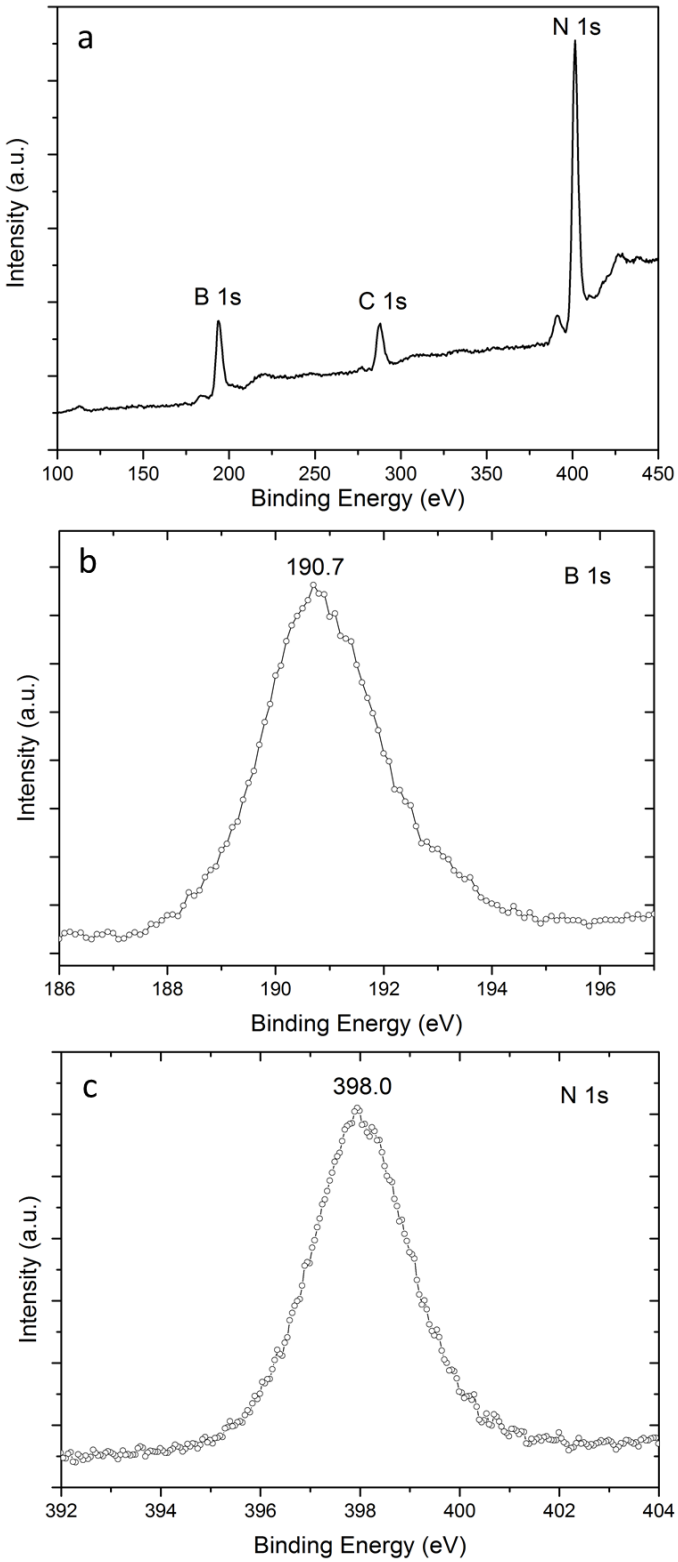

Figure 5.3. a) Full XPS survey spectrum of typical resultant *h*-BNNS for all samples, but only spectrum of BN650 is shown here; b) and c) XPS spectra for B and N elements, respectively.

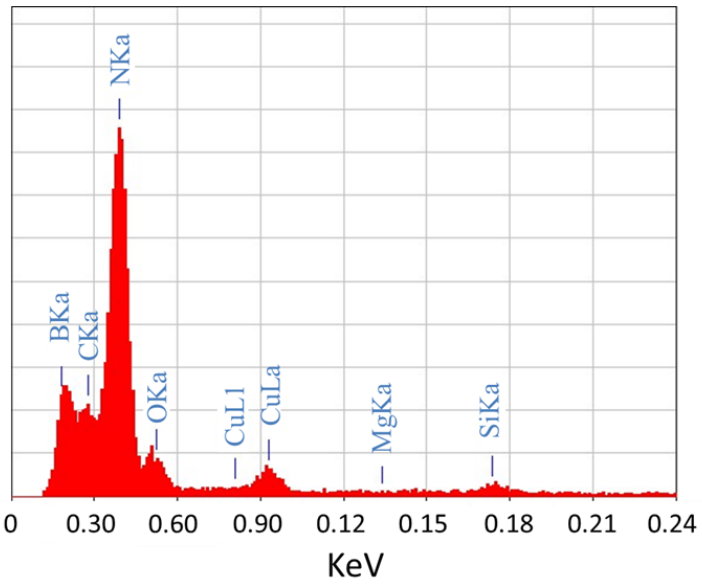

Figure 5.4. EDX spectrum collected under TEM for sample BN750, indicating that the product contains predominantly B and N with negligible amounts of Mg and Cl. (Silicon signal is likely to have arisen from the quartz tube.)

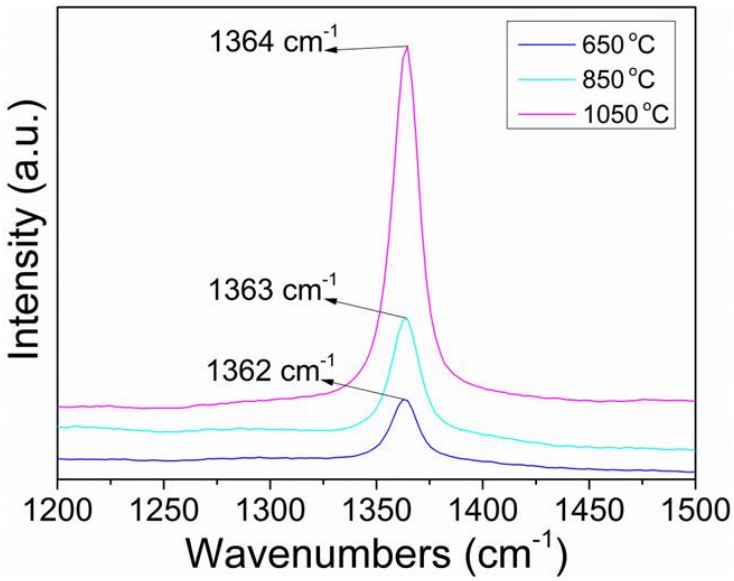

Figure 5.5. Raman spectra of BN650, BN850, and BN1050.

The morphologies of the *h*-BNNS have been carefully characterized through TEM (Figure 5.6). *h*-BNNS prepared at 650 °C (BN650) has a sheet-structured morphology with a lateral

size of up to 1.5 mm and wrinkles all over the sheet due to its thin graphene-like nature. The majority of the resultant *h*-BNNS is bi-layer at 650 °C (Figure 5.6d), and monolayer *h*-BNNS was also observed (Figure 5.7). As the synthesis temperature is increased, the *h*-BNNS becomes thicker, and it is up to 10 layers in BN850 and 20 layers in BN1050 (Figure 5.6b and c). This is because higher temperatures accelerate the evaporation and decomposition of the Mg-based by-products, favouring better crystallisation and growth. Note that during the synthesis, those nanosheets are prone to joining together to form bigger sheets, especially at higher temperatures.

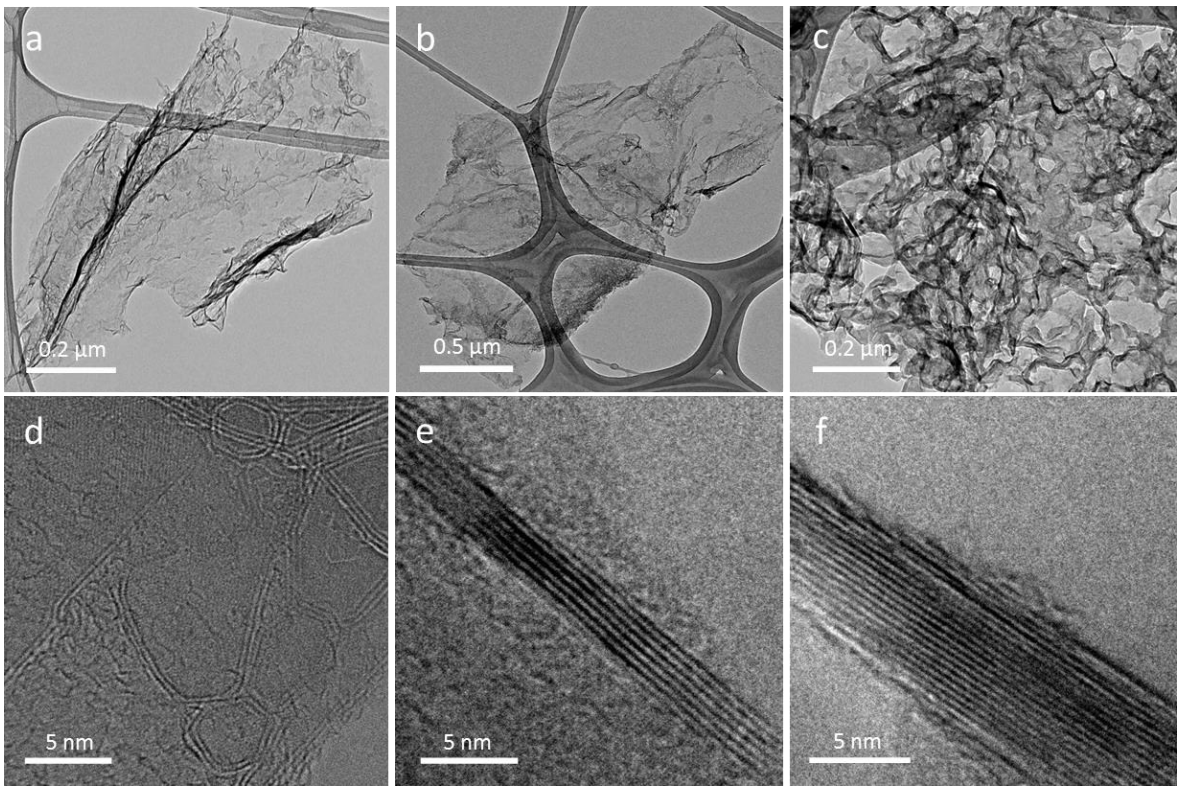

Figure 5.6. TEM images of BN650, BN850, and BN1050: (a–c) low magnification; (d–f) high magnification with clear lattice fringes.

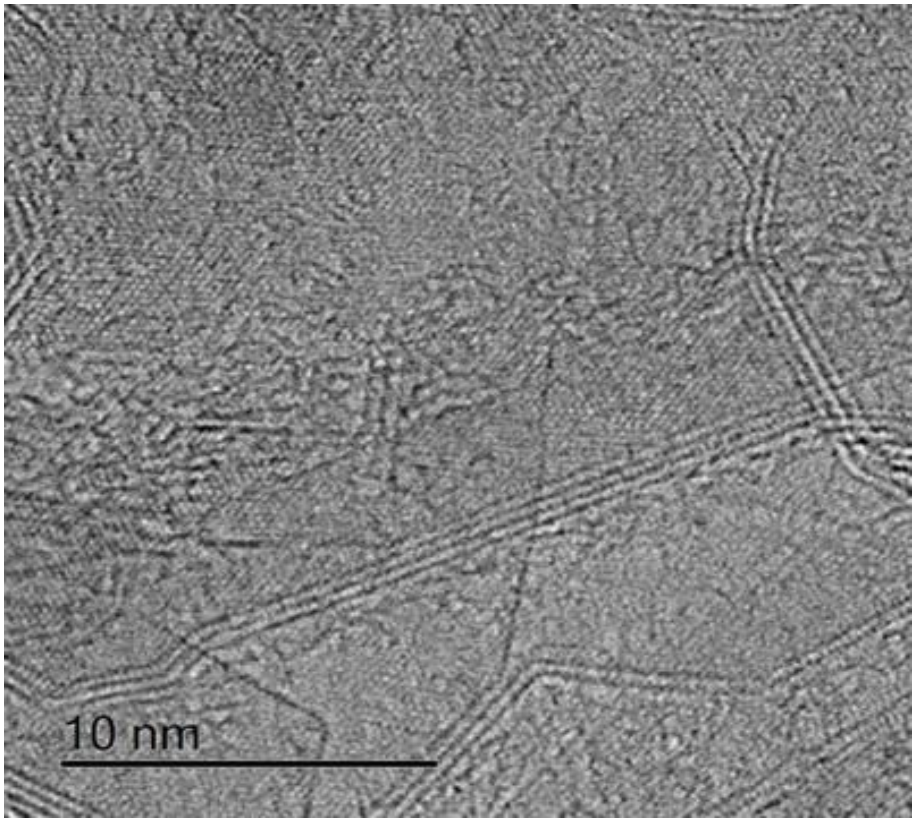

Figure 5.7. TEM image of BN650 with monolayer *h*-BNNS.

Nitrogen adsorption-desorption isotherms (Figure 5.8a) of the samples collected at 77 K show type-IV curves and H_1-type hysteresis loops. The pore size distributions derived from the adsorption branches using density functional theory (DFT) are correlated with the synthesis temperature (Figure 5.8b). A sharp peak corresponding to a pore size of 1 nm in diameter is observed for BN650 and BN750 (Figure 5.8b), suggesting a large proportion of micropores in these two products. This is also evident from the cumulative pore volume as a function of pore diameter (Figure 5.9). The micropore volumes of BN650 and BN750 are more than 3-fold higher than for the samples obtained at higher temperatures. All the samples contain mesopores around 4 nm in diameter.

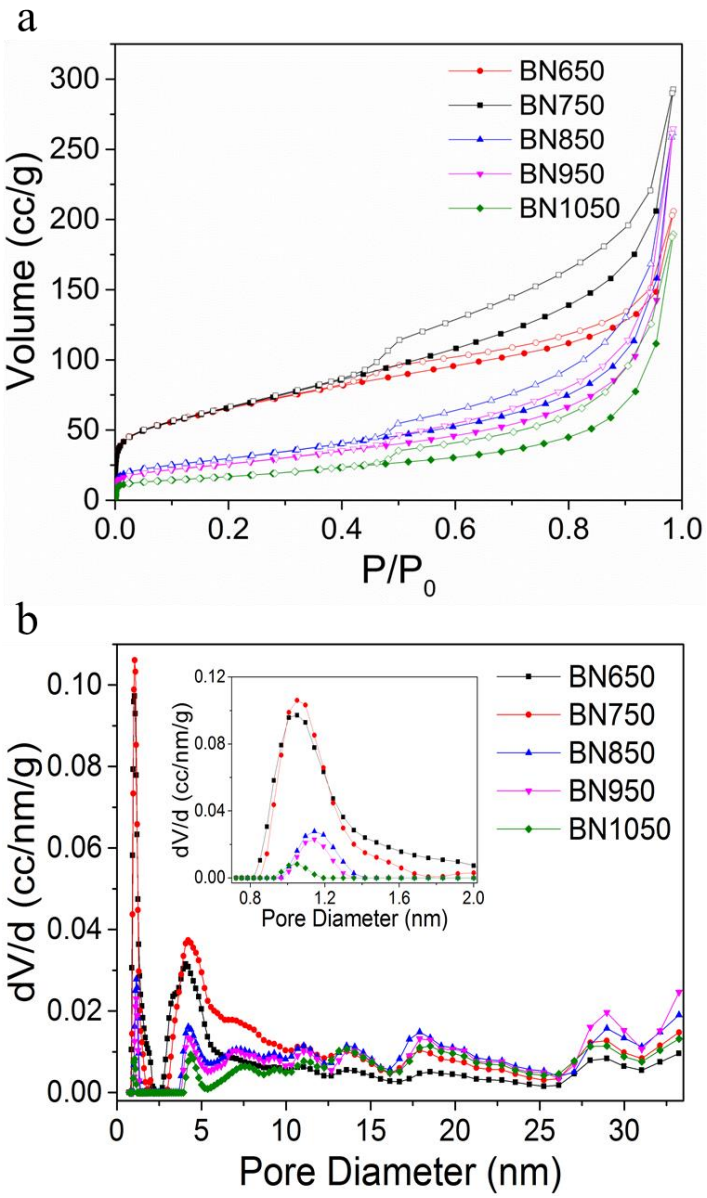

Figure 5.8. (a) Nitrogen adsorption–desorption isotherms. Closed symbols represent adsorption, and open symbols represent desorption. (b) Pore size distributions of the samples synthesized at varied temperatures. The inset is an enlargement of the small pore diameter range.

A previous report has proposed that micropores in porous *h*-BNNS arise mainly from enlarged interlayer distances and nonparallel BN layers.[21] Temperatures over 850 °C

facilitate crystallization of the *h*-BNNS, as evidenced by the XRD patterns (Figure 5.1c), and consequently, reduce the amount of non-parallel BN layers and thereby micropores. The evaporation of Mg-based by-products is temperature-dependent. Lower synthesis temperatures lead to slow evaporation and decomposition of the by-products, which slows down the crystallization of BN and contributes to the formation of larger amounts of micropores. It is also possible that the migration of the volatiles out of the materials may damage the BN layers and thereby generate pores. The Brunauer-Emmett-Teller (BET) surface area and cumulative pore volume data for the samples are summarised in Table 5.1. The surface areas range from 61-236 $m^2 g^{-1}$, much higher than that of the commercial BN powder (~25 $m^2 g^{-1}$). Based on the high specific surface areas and hierarchical pore-size distributions, this form of porous *h*-BNNS is expected to be a promising adsorbent.

Table 5.1. List of the specific surface areas and cumulative pore volumes for samples synthesized at varied temperatures.

Sample	Specific surface area/$m^2 g^{-1}$	Cumulative pore volume/cc g^{-1}
BN650	235	0.256
BN750	236	0.364
BN850	108	0.303
BN950	94	0.293
BN1050	61	0.220

Recently, porous *h*-BNNS have attracted attention for gas adsorption and pollutant removal due to their high porosity and high specific surface area, as well as their low density and high chemical stability.[21,26,27] The capture of CO_2 has attracted considerable attention in recent

years, since anthropogenic CO_2 emission is believed to be the main contributor to global warming. Each BN sample was therefore examined for CO_2 sorption up to 760 Torr at 298, 288, and 273 K (Figure 5.10a). Although BN750 has the highest specific surface area and largest cumulative pore volume (Figure 5.9), BN650 exhibited the highest CO_2 adsorption capacity. This could be ascribed to its micropore volume, which was highest in BN650 (Figure 5.8b and Figure 5.9). It is known that the micropores, not the surface area, play a dominant role in CO_2 adsorption at low pressure.[28] This is corroborated by the low CO_2 adsorption by samples BN850, BN950, and BN1050, all of which have low micropore volumes (Figure 5.8b and Figure 5.9). Note that mesopores may become predominant once micropores are already saturated and BN650 has the highest volume when micropores and mesopores are combined. In addition, BN650 demonstrated excellent selectivity of CO_2 over N_2. The selectivity was calculated from single component isotherms at 298 K, using values representing the composition of flue gas emitted from coalfired power plants (15% CO_2; 75% N_2; 10% other gases). The CO_2/N_2 selectivity as calculated through eqn 5.1 is 26.3, indicating that this form of *h*-BNNS exhibits high selectivity towards CO_2 adsorption. This selectivity is also ascribed to the large micropore volume which is known to be an essential factor for the selective adsorption of CO_2 over N_2.[29,30]

Equation of CO_2 selectivity

$$S = [q_1/q_2]/[p_1/p_2] \qquad (5.1)$$

S = selectivity

q_1=quantity of CO_2 @ p_1

q_2=quantity of N_2 @ p_2

p_1 = 0.15 bar (0.15 atm) for CO_2

p_2 = 0.75 bar (0.75 atm) for N_2

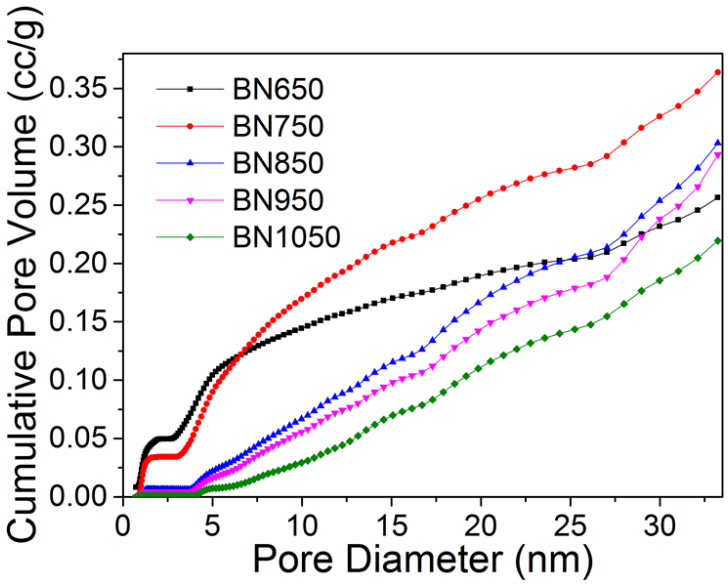

Figure 5.9. Cumulative pore volumes as a function of pore diameter.

Heat of adsorption (HoA) calculations were conducted for all the samples, and the results are shown in Figure 5.10c. BN650 is the best performing material, with good maintenance of the strength of the interaction out to coverage of over 7 cm^3 g^{-1}. BN750 behaves similarly but with a lower heat of adsorption. The data for BN850 and BN950 indicate a strong attraction for CO_2 at very low coverage, with values over 50 kJ mol^{-1}, although this rapidly drops away to below 20 kJ mol^{-1} at a coverage of around 2 cm^3 g^{-1}. This indicates that BN650 has more active sites that feature strong interaction with the CO_2 molecules than the other samples do. Note that at low pressure, HoA would affect the selectivity, and at high pressures, several other factors come in. In this paper, the selectivity test was carried out at ambient pressure of N_2 and CO_2, where CO_2 binds strongly with the active sites.

Another possible reason for the strong interaction between CO_2 and *h*-BNNS comes from recent simulations suggesting that lattice vacancies in BN give rise to strong interactions with CO_2 molecules,[31–34] with N vacancies leading to interactions between Lewis acidic B atoms and lone pairs on the O atoms in CO_2. The XPS results (Table 5.2) indicate that the as-obtained *h*-BNNS contain more B at lower synthesis temperatures, suggestive of potentially more B active sites. As the synthesis temperature increases, the B/N ratio comes closer to unity, resulting in less B active sites. The amount of B active sites could be correlated with the measured heat of adsorption (HoA, Figure 5.10c). The rapid drop in HoA for BN1050 compared with the steady HoA over adsorption for BN650, indicates that more active sites are available for CO_2 adsorption in BN650. It is difficult, however, to experimentally prove this reasoning at this stage.

Table 5.2. B and N atomic ratios (based upon XPS analysis) for samples prepared at varied temperatures.

Sample	N 1s (at%)	B 1s (at%)
BN650	44.50	55.50
BN750	45.85	54.15
BN850	46.12	53.88
BN950	46.76	53.24
BN1050	47.30	52.70

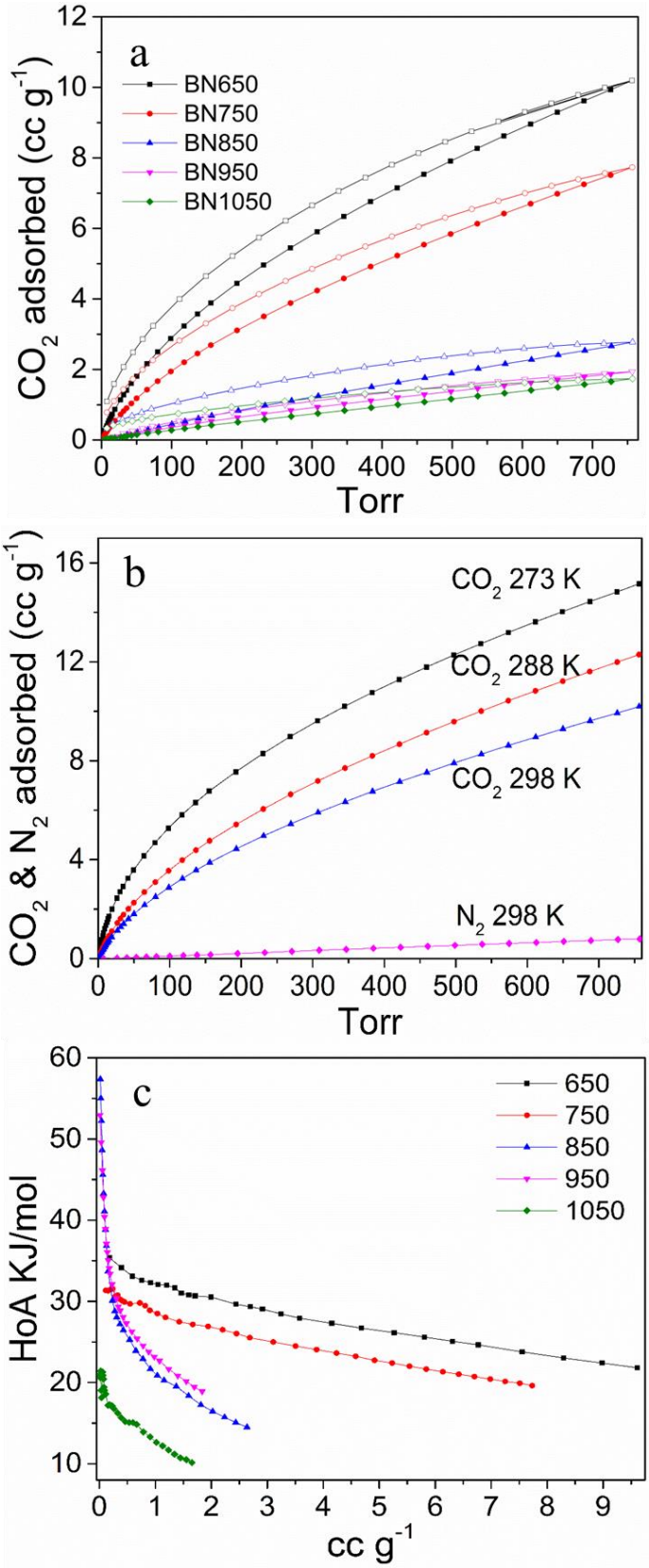

Figure 5.10. a) CO_2 adsorption-desorption isotherms at 298 K for each sample; b) CO_2 adsorption isotherms at 298, 288, and 273 K, and N_2 adsorption at 298 K for BN650; c) Heat

of adsorption plots for each sample. Closed symbols represent adsorption, and open symbols represent desorption.

5.4 Conclusion

In summary, a controllable synthesis method for few-layered porous *h*-BNNS was developed using MgB_2 as a dynamic template. At the optimum temperature, a large proportion of bi-layered *h*-BNNS is obtained, and to the best of my knowledge, this has not been achieved previously in a bottom-up synthesis. Additionally, the *h*-BNNS are hierarchically porous, with 1 nm micropores and 4 nm mesopores. The material is favourable for CO_2 adsorption, providing a CO_2/N_2 selectivity of 26.3. This facile and efficient synthetic method is very promising for the large-scale, low-cost preparation of porous *h*-BNNS for adsorption applications.

5.5 Reference

1. A. Pakdel, Y. Bando and D. Golberg, Chemical Society Reviews, 2014, 43, 934-959.

2. Y. Lin and J. W. Connell, Nanoscale, 2012, 4, 6908-6939.

3. D. Golberg, Y. Bando, Y. Huang, T. Terao, M. Mitome, C. Tang and C. Zhi, ACS Nano, 2010, 4, 2979-2993.

4. C. Zhi, Y. Bando, C. Tang, H. Kuwahara and D. Golberg, Advanced Materials, 2009, 21, 2889-2893.

5. J. Taha-Tijerina, T. N. Narayanan, G. Gao, M. Rohde, D. A. Tsentalovich, M. Pasquali and P. M. Ajayan, ACS Nano, 2012, 6, 1214-1220.

6. H. Zhu, Y. Li, Z. Fang, J. Xu, F. Cao, J. Wan, C. Preston, B. Yang and L. Hu, ACS Nano, 2014, 8, 3606-3613.

7. L. H. Li, J. Cervenka, K. Watanabe, T. Taniguchi and Y. Chen, ACS Nano, 2014, 8, 1457-1462.

8. Z. Liu, Y. Gong, W. Zhou, L. Ma, J. Yu, J. C. Idrobo, J. Jung, A. H. MacDonald, R. Vajtai, J. Lou and P. M. Ajayan, Nature Communications, 2013, 4, 1-8.

9. M. Yi, Z. Shen, X. Zhao, S. Liang and L. Liu, Applied Physics Letters, 2014, 104, 143101-143105.

10. Y. Li, P. S. Dorozhkin, Y. Bando and D. Golberg, Advanced Materials, 2005, 17, 545-549.

11. L. H. Li, E. J. G. Santos, T. Xing, E. Cappelluti, R. Roldán, Y. Chen, K. Watanabe and T. Taniguchi, Nano Letters, 2015, 15, 218-223.

12. H. Zeng, C. Zhi, Z. Zhang, X. Wei, X. Wang, W. Guo, Y. Bando and D. Golberg, Nano Letters, 2010, 10, 5049-5055.

13. Q. Weng, X. Wang, C. Zhi, Y. Bando and D. Golberg, ACS Nano, 2013, 7, 1558-1565.

14. X. Zhang, G. Lian, S. Zhang, D. Cui and Q. Wang, CrystEngComm, 2012, 14, 4670-4676.

15. J. N. Coleman, M. Lotya, A. O'Neill, S. D. Bergin, P. J. King, U. Khan, K. Young, A. Gaucher, S. De, R. J. Smith, I. V. Shvets, S. K. Arora, G. Stanton, H.-Y. Kim, K. Lee, G. T. Kim, G. S. Duesberg, T. Hallam, J. J. Boland, J. J. Wang, J. F. Donegan, J. C. Grunlan, G. Moriarty, A. Shmeliov, R. J. Nicholls, J. M. Perkins, E. M. Grieveson, K. Theuwissen, D. W. McComb, P. D. Nellist and V. Nicolosi, Science, 2011, 331, 568-571.

16. Y. Lin, T. V. Williams, T.-B. Xu, W. Cao, H. E. Elsayed-Ali and J. W. Connell, The Journal of Physical Chemistry C, 2011, 115, 2679-2685.

17. T. Sainsbury, A. Satti, P. May, Z. Wang, I. McGovern, Y. K. Gun'ko and J. Coleman, Journal of the American Chemical Society, 2012, 134, 18758-18771.

18. J. Li, J. Lin, X. Xu, X. Zhang, Y. Xue, J. Mi, Z. Mo, Y. Fan, L. Hu, X. Yang, J. Zhang, F. Meng, S. Yuan and C. Tang, Nanotechnology, 2013, 24, 155603.

19. A. Vinu, M. Terrones, D. Golberg, S. Hishita, K. Ariga and T. Mori, Chemistry of Materials, 2005, 17, 5887-5890.

20. P. Dibandjo, L. Bois, F. Chassagneux, D. Cornu, J. M. Letoffe, B. Toury, F. Babonneau and P. Miele, Advanced Materials, 2005, 17, 571-574.

21. Q. Weng, B. Wang, X. Wang, N. Hanagata, X. Li, D. Liu, X. Wang, X. Jiang, Y. Bando and D. Golberg, ACS Nano, 2014, 8, 6123-6130.

22. J. Li, X. Xiao, X. Xu, J. Lin, Y. Huang, Y. Xue, P. Jin, J. Zou and C. Tang, Scientific Reports, 2013, 3, 3208.

23. J. Thomas, N. E. Weston and T. E. O'Connor, Journal of the American Chemical Society, 1962, 84, 4619-4622.

24. E. J. M. Hamilton, S. E. Dolan, C. M. Mann, H. O. Colijn, C. A. McDonald and S. G. Shore, Science, 1993, 260, 659-661

25. H.-C. Eom, H. Park and H.-S. Yoon, Advanced Powder Technology, 2010, 21, 125-130.

26. W. Lei, D. Portehault, D. Liu, S. Qin and Y. Chen, Nature Communications, 2013, 4, 1777.

27. Q. Weng, X. Wang, Y. Bando and D. Golberg, Advanced Energy Materials, 2014, 4, 1301525.

28. A. Lu, S Dai, Green Chemistry and Sustainable Technology, 2014.

29. E. N. C. Paura, W. F. da Cunha, L. Rocaratti, J. B. L. Martins, G. M. e Silva and R. Gargano, RSC Advances, 2015, 5, 27412-27420.

30. S. H. Lee, N. Kim, D. G. Ha and S. K. Kim, Journal of the American Chemical Society, 2008, 130, 16241-16244.

31. Y. Jiao, A. Du, Z. Zhu, V. Rudolph, G. Q. Lu and S. C. Smith, Catalysis Today, 2011, 175, 271-275.

32. H. Choi, Y. C. Park, Y.-H. Kim and Y. S. Lee, Journal of the American Chemical Society, 2011, 133, 2084-2087.

33. Q. Sun, Z. Li, D. J. Searles, Y. Chen, G. Lu and A. Du, Journal of the American Chemical Society, 2013, 135, 8246-8253.

Chapter 6 Conclusions and Outlook

6.1 Conclusions

During my PhD study, two types of *h*-BNNS, OH-BNNS and porous *h*-BNNS, have been synthesized and investigated. Based on their structural and chemical features, they have been appropriately utilized for different applications with satisfying results. For example, the OH-BNNS/PNIPAM hydrogel composite exhibits significantly improved thermal performance compared to the neat PNIPAM hydrogel; porous *h*-BNNS has a high surface area andabundant micropores, which result in high adsorption capacity towards CO_2.

OH-BNNS was produced through exfoliation and functionalization of bulk *h*-BN by water steam at high temperature. This synthesis process is a facile one-pot and low-cost method without the need for any harsh chemicals. More importantly, it is easily scaled up, so that it is fully qualified to meet industrial quantity requirements. Additionally, the mechanism of the exfoliation and functionalization process has been clearly clarified. It has been found that *h*-BN is easily affected by moisture at high temperature, which provides a new facile method to exfoliate and functionalize *h*-BN. Furthermore, it has been demonstrated that the hydroxyl groups are only located along the edges of OH-BNNS, which has been confirmed by EELS mapping and Raman mapping. The resultant OH-BNNS can be well dispersed in aqueous and organic solutions, with dispersions of 0.3 mg mL^{-1} in water and 0.06 mg mL^{-1} in ethanol, respectively. This excellent dispersion of OH-BNNS enables it to be an effective additive to PNIPAM hydrogel, achieving a remarkable enhancement (41%) of the thermal performance by adding only 0.07 wt% OH-BNNS without compromising its mechanical properties. In addition, the distribution of hydroxyl group along the edges of OH-BNNS strongly improves the thermal response of OH-BNNS/PNIPAM, since hydroxyl groups on the basal plane

would be detrimental to the heat transfer. In the application testing, the OH-BNNS/PNIPAM hydrogel composite exhibited improved dimensional change. More interestingly, the dye-release test suggested that it has elevated drug delivery capability.

The synthesis of porous *h*-BNNS was designed by using MgB_2 as a dynamic template and NH_4Cl as an etchant, with NH_3 as a carrier gas and nitrogen source. This method has avoided many of the shortcomings previously reported in the literature, such as difficulties in efficient filling of the nanopores and complete removal of the template, limited production, high cost of templates, and additional procedures for the removal of templates. More importantly, it is able to control the morphology of the porous BN to produce a 2D sheet structure with a majority of bi-layered sheets. MgB_2 supplies the dynamic template associated with its layered structure, where Mg atoms are sandwiched by boron sheets. In the reaction, NH_4Cl decomposes to HCl, acting as an etchant to react with the Mg layers, while NH_3 acts as a nitrogen source to form the *h*-BNNS. The brownish powder obtained below 450 °C suggested the formation of elemental boron. With elevated temperature, the B-N stretching mode and bending modes started appearing sequentially in IR spectra, indicating the formation of *h*-BNNS. In addition, the morphologies of *h*-BNNS were investigated. The majority of the resultant *h*-BNNS is bi-layered at 650 °C and the *h*-BNNS becomes thicker with elevated temperature. This is ascribed to the acceleration of evaporation and the decomposition of Mg-based by-products at higher temperatures, promoting better crystallisation and growth of *h*-BNNS. It has also been proposed that the porous structure is due to the evaporation of Mg-based by-products and the migration of volatiles out of the material. The resultant porous *h*-BNNS has shown much higher surface area than that of the bulk *h*-BN (~25 $m^2 g^{-1}$), ranging from 61-236 $m^2 g^{-1}$. Moreover, the products synthesized at 650 °C and 750 °C had a large

proportion of micropores, which enabled them to exhibit great CO_2 adsorption capacity and CO_2/N_2 selectivity.

6.2 Outlook

All the work above can be modified to some extent to improve their performance. For the first sub-project, to enlarge the lateral size of OH-BNNS and to reduce the layer thickness would make the thermal conduction more continuous and smooth, and more (002) planes would be exposed, which would be beneficial for thermal transfer. For the second sub-project, there is considerable room to enhance the surface area to increase the adsorption capacity.

h-BNNS is endowed with many excellent properties, especially its chemical and thermal stability and its nontoxicity, which enable it to trump other materials in some sophisticated fields, such as electronic, military, and biological applications. Although there is a long way to go for the more practical applications to be realized, I think that *h*-BNNS will be a shining star in this scientific field.